IEKP-KA/93-9

Longitudinal Shower Development in the DELPHI Electromagnetic Calorimeter HPC

Christof Kreuter

Institut für Experimentelle Kernphysik
Fakultät für Physik, Universität Karlsruhe (TH)

21 June, 1993

Longitudinal Shower Development in the DELPHI Electromagnetic Calorimeter HPC

Diplomarbeit

an der

Universität Karlsruhe (TH)

von

Christof Kreuter
aus Bremm

21. Juni 1993

Hauptreferent: *Prof. Dr. W. de Boer*
Korrereferent: *Prof. Dr. D. C. Fries*

Versicherung

Ich versichere, daß ich diese Arbeit selbständig und nur unter Verwendung der angegebenen Hilfsmittel angefertigt habe, und daß ich alle Stellen, die dem Wortlaut oder dem Sinne nach anderen Werken entnommen sind, durch Angabe der Quellen als Entlehnung kenntlich gemacht habe.

Karlsruhe, den 21.06. 1993 Christof Kreuter

Abstract

In present and future experimental high energy physics, calorimeters are and will play a major role in complex detector systems. Therefore the construction and study of new technologies such as the High Density Projection Chamber (HPC) contribute to the development in detector physics. In this report several studies concerning the HPC are described.

The first study concerned the calibration of 1992 data. For the calibration of the HPC normally Bhabha scattering and the response from a Krypton signal, originating from the radioactive decay of a Krypton source, are considerd. Detailed studies on the calibration and on the improvement of energy and spatial resolution will be presented.

Due to a natural α–radioactivity in the lead converter, the response of the HPC to a given signal decreases with time (*ageing*). In order to reduce the ageing speed of the HPC read-out chambers, new chambers were developed, the so-called graphite chambers. Results from a Krypton Monte Carlo, studying the properties and resolutions of the graphite chambers and the normal brass chambers, will be presented.

The main contents of this report will focus on a longitudinal shower fit, performed on the nine layers of the HPC, as a major tool for electron identification in DELPHI. Using the model of a Γ-distribution describing the longitudinal shape of a shower, a working algorithm was developed which provided a significant separation between electromagnetic and hadronic showers. In order to improve efficiencies, the shower fit was extended to work also in θ-cracks (regions between modules which are not sensitive to charge). The recovery of θ-crack showers will be shown to be excellent. The electron identification is now comparable with the one from other detectors at LEP.

Contents

List of Figures

List of Tables

Chapter 1

Introduction

The long history of human beings shows that there is a natural interest in exploring the surrounding nature. For hundreds of years people developed theories about the origin and the structure of the universe. The primary motivation was not only to derive applications (e.g. astronomy provided the tool for navigation), but to obtain more information on the origin of human beings in the surrounding world. Scientific curiosity is still the motivation for research in our days even if it is sometimes hidden by economical, ecological or military interests. The tools for modern research have changed drastically. In the Greek philosophy, theories were only developed from the daily experience of nature and the human spirit. In the present era of science, theories are based on large experiments. In high energy physics, experiments involving hundreds of physicists are performed to obtain details on the structure of matter.

The present knowledge of our understanding of nature consists mainly of three theories:

(1) The general theory of relativity, published by A. Einstein in 1915, describes the effects of gravity. By using a pseudo Riemanian geometry for the 4–dimensional space–time, introduced by special relativity, gravitational effects are explained by the curvature of this space–time. The curvature is induced by massive objects. Test particles in such a curved space–time are expected to move on geodaesics. Efforts to transform the general theory of relativity in a quantum theory have not been successful yet.

(2) The theory of strong interactions which is called Quantum ChromoDynamics (QCD) describes the effects of quark interactions. Experimental evidence for QCD has been obtained from deep inelastic electron–proton scatterings as well as by the measurement of the ratio of the hadronic and leptonic cross section in electron–positron annihilations. The gauge boson of the strong interaction, the gluon, has been discovered in three jet events at the electron positron ring PETRA[1]at DESY[2]. Since the gluon carries color charge, this leads to the observed quark gluon confinement at lower energies. Because of this effect the theory (QCD) has to be a non–Abelian theory.

(3) The Standard Model of the electroweak interactions has been developed by Glashow, Salam and Weinberg [1]. It is often called GSW theory. It unifies the first modern gauge theory, the Quantum ElectroDynamics (QED) which was constructed by Feynman, with the

[1] PETRA : Positron Electron Tandem Ring Accelerator

[2] DESY : Deutsches Electronen Synchrotron

weak interaction which is responsible for radioactive decays. This electroweak theory predicted the existence of three new gauge bosons, the $W^{\pm}$ and the Z^0. They were discovered in the predicted mass range in 1983 and 1984 in proton-antiproton experiments at CERN[3] [2].

In order to investigate the properties of the electroweak gauge bosons Z^0 and $W^{\pm}$ the LEP[4] collider at CERN has been built. The collider produces Z^0's from the annihilation of electrons and positrons in resonance at a center of mass energy of $m_Z = 91.2\ GeV$. Four detectors (ALEPH, DELPHI, L3, OPAL) collect the data from the decay products of the Z^0's.

In a second stage of LEP the collider will be upgraded to an energy of twice the $W^{\pm}$ mass, in order to produce $W^{\pm}$ pairs. This stage is called LEP200. This upgrade is foreseen for the years 1994–95. In this way the charged electroweak bosons can be investigated.

In this thesis, detector studies of the DELPHI barrel electromagnetic calorimeter, the High Density Projection Chamber (HPC), will be presented. After a description of the DELPHI experiment some major theoretical background for the understanding of a calorimeter like the HPC will be given.

For the calibration of the HPC normally Bhabha scattering and the response from a Krypton signal, originating from the radioactive decay of a Krypton source, are considered. Detailed studies on the calibration and on the improvement of energy and spatial resolution will be presented (see chapters 4 and 5).

Due to a natural α–radioactivity in the lead converter, the response of the HPC to a given signal decreases with time. This effect is called *ageing*. In order to reduce the ageing speed of the HPC read-out chambers, new chambers were developed, the so-called graphite chambers. Results from a Krypton Monte Carlo, studying the properties of the graphite chambers and of the normal brass chambers, will be explained in chapter 5.

The main topic of this thesis will be the electron identification in DELPHI by using a longitudinal shower fit in the HPC (see chapter 6). Since electrons form an electromagnetic shower in a calorimeter, the typical shape of such an electron shower can be used for the separation of electron showers from pion showers. In order to increase efficiencies a special treatment for θ-cracks (regions between modules which are not sensitive to charge) in the HPC was developed. Furthermore, a method to obtain shower fluctuations will be presented.

[3] CERN: Conseil Européen pour la Researche Nucléaire

[4] LEP : Large Electron Positron collider

Chapter 2

The Experiment

In this chapter, the experimental setup of the **L**arge **E**lectron **P**ositron collider (LEP) at CERN will be described. After a description of the LEP machine, the DELPHI detector, one of the four LEP experiments, will be explained in more detail. This will be followed by a description of the DELPHI barrel calorimeter, the **H**igh Density **P**rojection **C**hamber (HPC).

2.1 The LEP Collider

The LEP storage ring with a circumference of about 27 km is installed in the LEP tunnel which has a diameter of 3.80 m and lies 50 to 150 meters below the surface across the frontiers between France (Pays de Gex) and Switzerland (Canton Genève) [3]. The LEP ring basically consists of a beam pipe and a set of magnets and acceleration sections and their power supplies. The magnets either bend or focus the electron beam while the acceleration sections consisting of several radio frequency cavities provide the energy for the acceleration of the electrons and positrons. In total, there are 3392 dipole magnets, 876 quadrupole and 520 sextupole magnets. Since the electrons and positrons have opposite charge and equal mass, they can circulate in one single beam pipe with the same arrangement of focusing and bending magnets. Therefore, LEP has only one beam pipe.

The energy of the electrons and positrons in the LEP100 phase is around 45 GeV. This is achieved in a several step procedure (see Figure 2.1). In the first step of positron generation, electrons are accelerated at the LEP Injector Linacs (LIL) to an energy of about $200MeV$. Collisions with a target of high atomic number Z lead to the production of positrons with an average energy of $10MeV$. A small fraction (1/1000) of the positrons is accelerated by the second stage LIL to $600MeV$. The electrons for the electron beam are produced by a $10MeV$ electron gun and are injected directly into the second stage LIL. In the next step the electrons and positrons are accumulated in the Electron Positron Accumulator (EPA) to increase the current of each beam. The Proton Synchrotron (PS) then accelerates the beams to 3.5 GeV followed by the Super Proton Synchrotron (SPS) which provides an energy of 20 GeV. Finally the beams are injected into LEP where the particles are accelerated to about 45 GeV. The

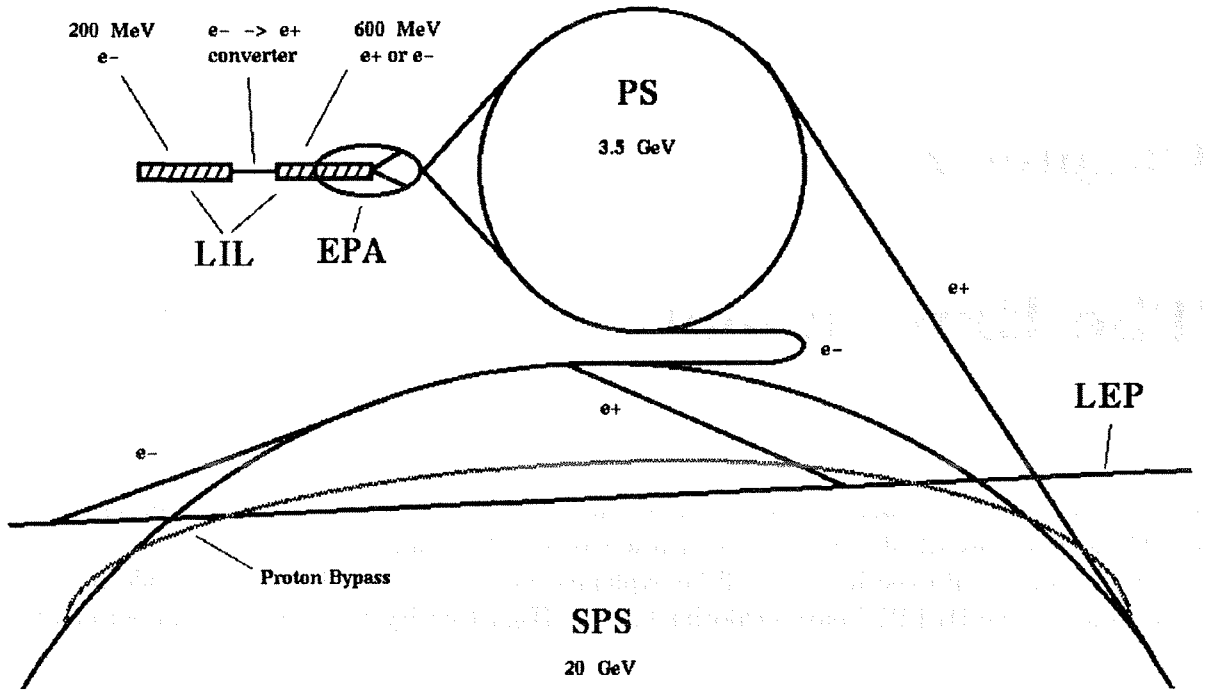

Figure 2.1: *Schematic view of the LEP injection system, which shows the two stage LEP Injector Linacs (LIL), the Electron Positron Accumulator (EPA), the Proton Synchrotron (PS), the Super Proton Synchrotron (SPS) and the LEP ring itself. The 10 MeV electron gun close to the $e^- \rightarrow e^+$ converter is not shown.*

energy loss ΔU due to synchrotron radiation is given by:

$$\Delta U = 8.85 \cdot 10^{-5} \frac{E^4}{r} \cdot \frac{m}{GeV^3} \quad , \tag{2.1}$$

where E is the beam energy and r the bending radius of the ring. The synchrotron radiation loss in LEP is not negligible and consumes about $1.2MW$ of power. It is the major constraint on the maximum beam energy for LEP100 with the present accelerator sections.

Each beam is concentrated in short time bunches which consists typically of about $4 \cdot 10^{11}$ electrons or positrons. LEP has been running with a bunch length of $4.5cm$ ($7cm$) in 1992 (1991). The transverse dimensions are in the order of a few millimeters and the beam profile is strongly elliptic. Until mid 1992 four bunches for electrons and positrons were used. For the 1993 running period it is scheduled to run in eight bunch mode. Both bunch systems are synchronized so that they cross each other at the four interaction points which are surrounded by the Detectors ALEPH, DELPHI, OPAL and L3. The production of Z^0 events at the interaction points is increased, because the size of the bunches is squeezed by strong superconducting quadrupole magnets close to the detectors.

From the physics point of view, two important machine parameters are the center of mass energy $\sqrt{s}$ and the luminosity $\mathcal{L}$. The center of mass energy $\sqrt{s}$ of an e^+e^- storage ring of two beams with exactly the same energy is twice the beam energy. This is the most economical way of achieving the highest possible center of mass energy. In order to get a stable beam several effects such as betatron oscillations[1], or beam-beam effects[2], have to be considered. Another more spectacular effect which influences the beam energy on the per mill level is the phase of the moon. Since the moon stretches the surface of the earth and influences the total orbit length the beam energy is changed. A clear correlation of the LEP energy with the phase of the moon has been measured ([4], [5]).
The luminosity $\mathcal{L}$ is defined by [6]:

$$n = \sigma \cdot \mathcal{L} \ , \tag{2.2}$$

where n is the number of events per second of a given type and σ is the corresponding cross section. The luminosity depends on some specific machine parameter and can be expressed in the following way:

$$\mathcal{L} = \frac{N^+ \cdot N^- \cdot k \cdot f}{4\pi \cdot \sigma_x \cdot \sigma_y} \ , \tag{2.3}$$

where $N^{\pm}$ denotes the number of electrons or positrons in a bunch, k is the number of bunches, f is the revolution frequency and σ_x and σ_y are the horizontal and vertical widths of the beams at the collision point. The beam current is defined as:

$$I^{\pm} = N^{\pm} \cdot k \cdot f \cdot e^{\pm} \ , \tag{2.4}$$

where $e^{\pm}$ is the elementary charge of the electrons and positrons. Typical beam currents for LEP during the 1992 running period were $1.2mA$. An integrated luminosity of roughly $32pb^{-1}$ has been collected in the years 1990-92. As an example we consider the decay of the Z^0 into hadrons. The cross section for the Z^0 production times its branching ratio into hadrons at the Z^0 peak is roughly $13nb$. This leads with the integrated luminosity of $32pb^{-1}$ to roughly 415 000 hadronic Z^0 events.

At LEP200 the center of mass energy will go up to roughly 180 GeV in order to produce $W^+ W^-$ pairs. Due to the drastic drop in cross section and the expected rise in luminosity one expects about 1000 $W^{\pm}$ pairs per year. A serious problem for LEP200 is the energy consumption of the ring. Due to synchrotron radiation an energy loss of about $38MW$ is expected for the case of eight bunches. This corresponds to roughly 10% of the production of a modern power station. In order to optimize the acceleration section of LEP the conventional radio-frequency (RF) cavities will be exchanged with superconducting RF cavities.

[1] Oscillations of the beam around the ideal orbit of the machine are called betatron oscillations.

[2] Electromagnetic interactions between the beams lead to an increased betatron frequency.

2.2 The DELPHI Detector

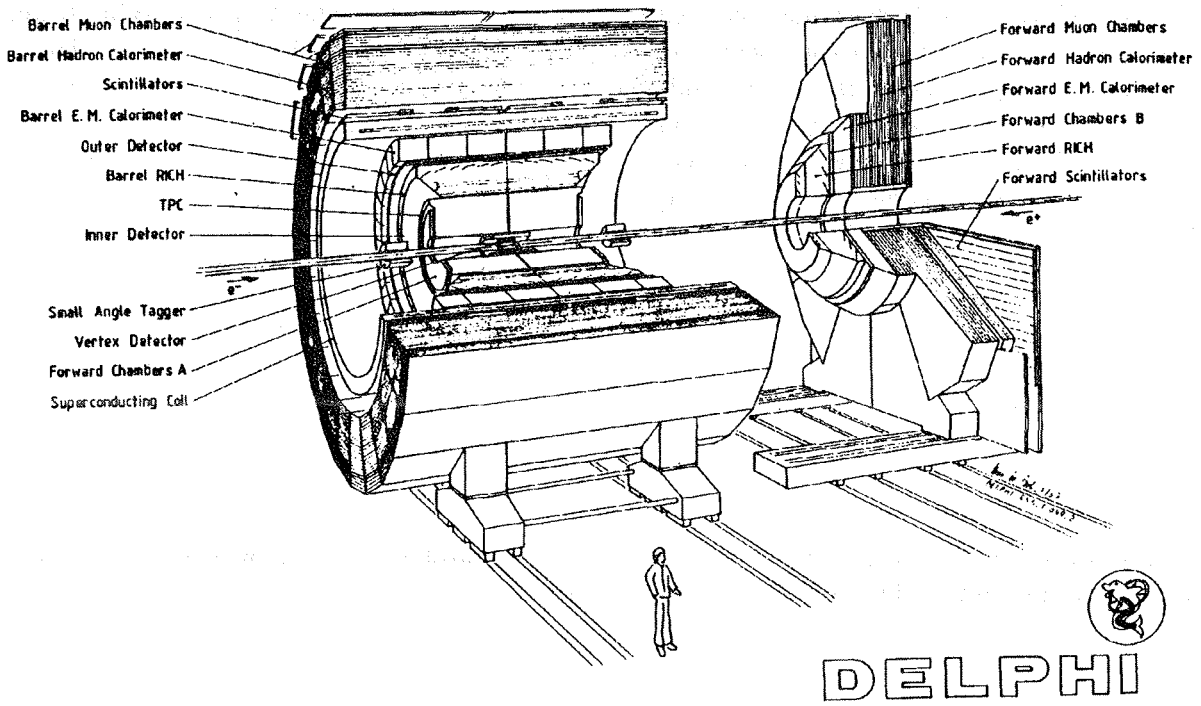

Figure 2.2: *Schematic view of the DELPHI detector: micro vertex detector (μV), inner detector (ID), time projection chamber (TPC), ring imaging Cherenkov counter (RICH), outer detector (OD), high density projection chamber (HPC), superconducting solenoid, time of flight scintillators (TOF), hadron calorimeter (HAC), muon chambers (MUB and MUF), forward drift chambers (FCA and FCB), small angle tagger (SAT), forward electromagnetic calorimeter (FEMC).*

One of the four large LEP experiments is the DELPHI detector ([7], [8]), constructed and run by a collaboration of 540 physicists coming from 41 different universities and national laboratories. The construction time of DELPHI was roughly 7 years. The costs for the construction of DELPHI not including the manpower provided by the institutes were in the order of 150 MSFr. Since the operational beginning of LEP in November 1989, DELPHI has collected over 500 000 Z^0 events by early summer 1992.

DELPHI stands for **DE**tector for **L**epton, **P**hoton and **H**adron **I**dentification. A schematic view of the detector is given by the Figures 2.2, 2.3 and 2.4. The detector architecture has, besides some conventional components of an e^+ e^- detector, some features to identify particles. Hadronic particle identification is done by using the Ring Imaging Cherenkov (RICH) technique for the separation of protons, pions and kaons in a certain momentum range. The Barrel RICH (BRICH) was operational for 70% of the time in 1992, while the installation of the Forward RICH (FRICH) was finished at the end of 1992. Another important sub-detector

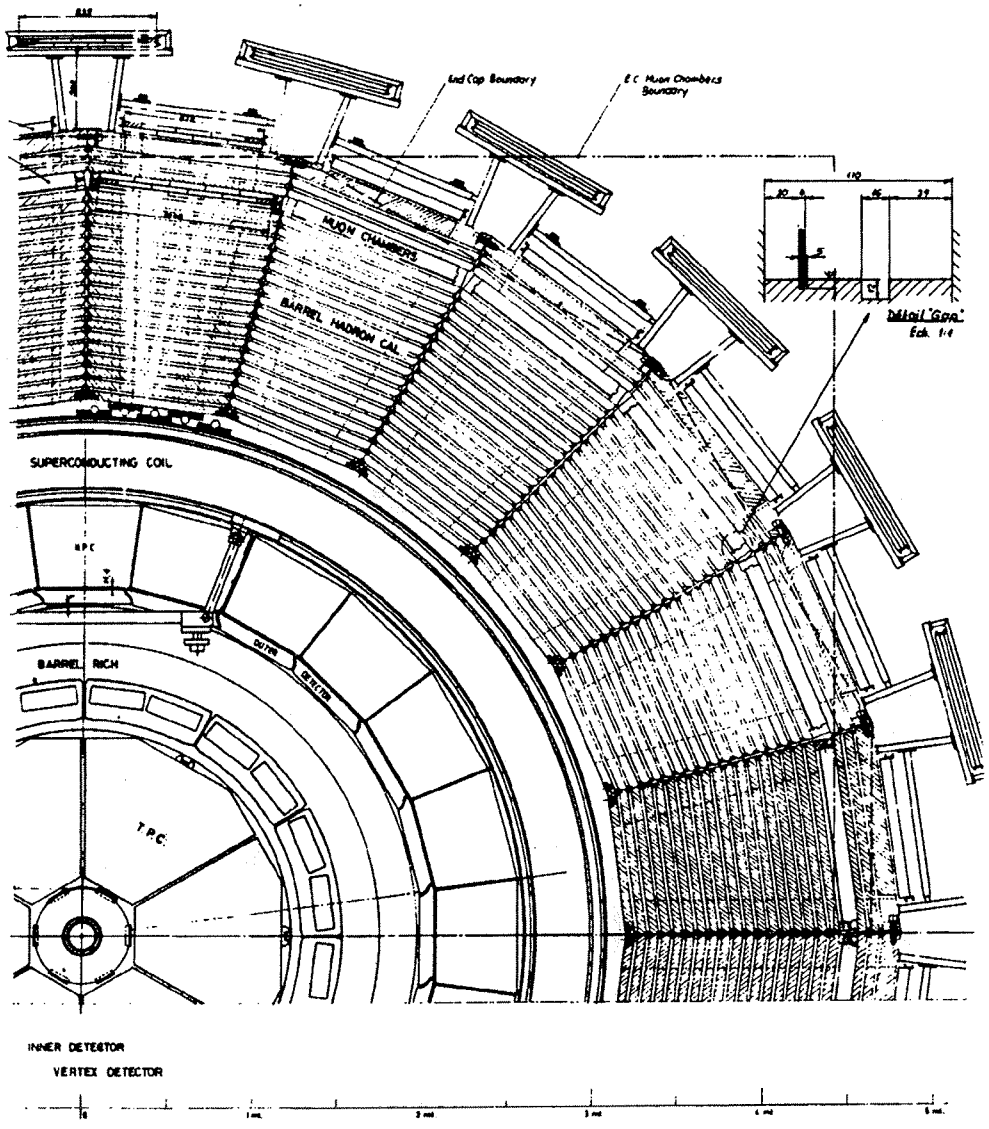

Figure 2.3: *Schematic view of the DELPHI detector along the beam pipe*

is the Time Projection Chamber (TPC) which provides a three dimensional track information of charged particles in the barrel region including a good Z resolution. In addition the tracking in the barrel region is supplemented by a Micro Vertex (μV) detector for precise reconstruction of secondary vertices ($\sigma_{R\phi} = 7\mu m$), the Inner Detector (ID) for fast triggering and vertex reconstruction and finally the Outer Detector (OD) for fast triggering and momentum reconstruction. The tracking in the forward region is done using the TPC, the forward chambers FCA and FCB and the FRICH. A homogeneous magnetic field of 1.2 Tesla allows the determination of the momenta of charged particles. It is provided by a superconducting magnet with a diameter of 5.2 m and a length of 7.2 m. The momentum resolution in the

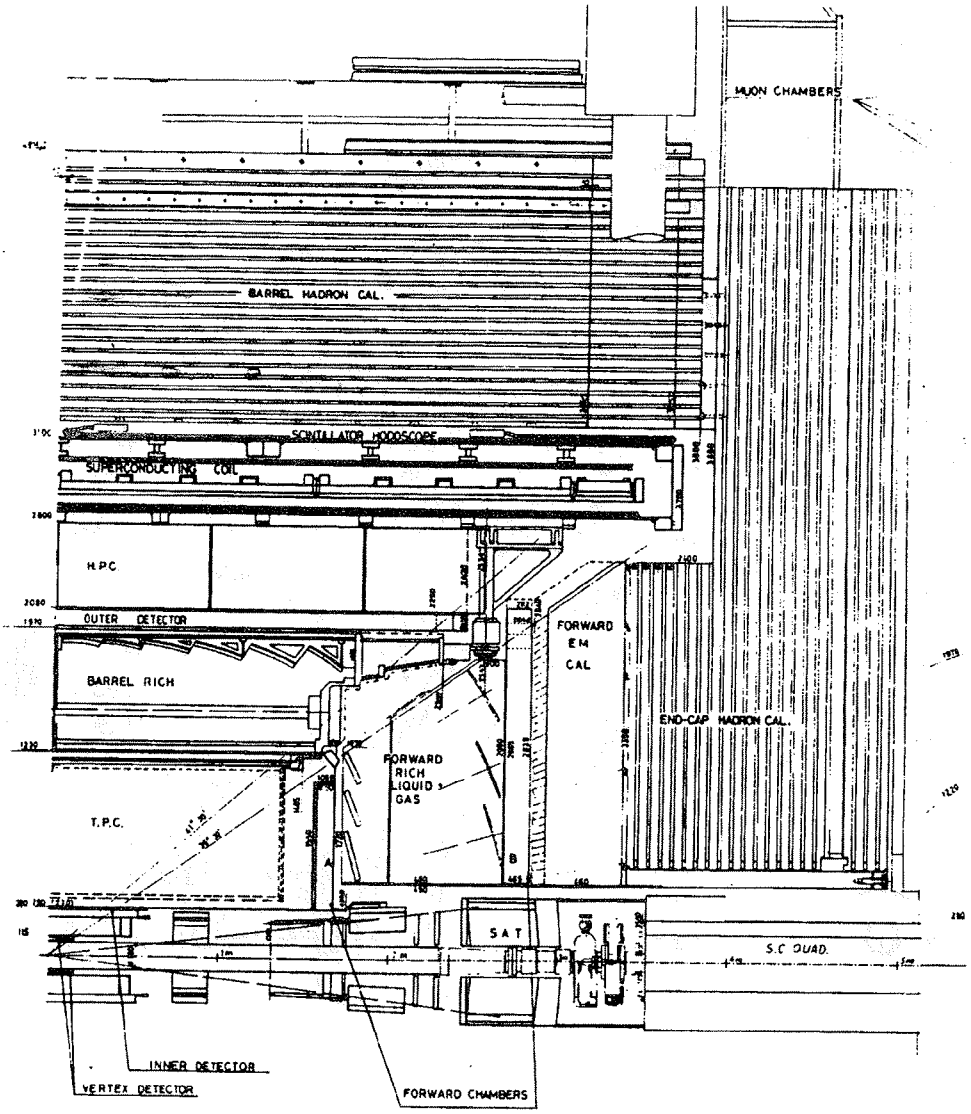

Figure 2.4: *Schematic view of the DELPHI detector perpendicular to the beam pipe*

barrel (measured with muons) is:

$$\frac{\sigma_p}{p} = 0.0010 \cdot \frac{p}{1\ \mathrm{GeV}} \quad , \tag{2.5}$$

if one combines the ID, TPC and OD track elements. The momentum resolution in the forward region with $20° \leq \theta \leq 35°$ is:

$$\frac{\sigma_p}{p} = 0.0037 \cdot \frac{p}{1\ \mathrm{GeV}} \quad , \tag{2.6}$$

using the ID, TPC and FCB information. The azimuthal track resolution measured with the

ID, TPC and OD but without μV detector is

$$\sigma_{R\phi} = 90\mu m \quad . \tag{2.7}$$

Electrons and photons are identified and their energy is measured using the High Density Projection Chamber (HPC) in the barrel region and the Forward ElectroMagnetic Calorimeter (FEMC) in the region below 40°, which consists of lead glass blocks and is read out by photomultipliers. The HPC will be described in more detail in section 2.3. The calorimeter components are completed by the Hadron Calorimeter (HCAL) in the barrel and the forward region. In order to identify muons the Barrel and Forward Muon Chambers (MUB and MUF) are grouped outside the hadron calorimeters. In the very forward region, the Small Angle Tagger (SAT) and the Very Small Angle Tagger (VSAT) are tracking and calorimeter devices which also allow a determination of the luminosity of LEP. The coordinate system to describe the detector has its Z-direction parallel to the beam pipe with positive Z-direction given by the electron direction. The radius R and the azimuth ϕ are perpendicular to the beam and the polar angle $\theta = 0°$ is along the Z axis.

Data measured by DELPHI are processed using the DELANA[3] software package where the raw data information of an event is transformed into physics information e.g. momenta and energies of particles. According to different hardware configurations of DELPHI and different calibrations and alignments one has to distinguish between different processings. DELANA_F denotes the most recent processing for 1991 data. For 1992 data the last processing is called DANA92_C.

As an example Figure 2.5 shows a three-jet event recorded by the DELPHI detector visualized by the 3-D interactive colour display program DELGRA. The individual charged tracks are marked as lines and the hits in the calorimeter as boxes. DELGRA is a useful tool for the investigation of the detector performance and for checks of the results of analysis programs (e. g. track fits and shower reconstructions).

2.3 The High Density Projection Chamber

In this section a brief description of the High Density Projection Chamber will be given followed by a description of HPC offline software. In chapter 3 some detailed physical effects will be discussed which are important for the understanding of a calorimeter like the HPC.

2.3.1 The Construction of the HPC

The High Density Projection Chamber (HPC) is the barrel electromagnetic calorimeter in DELPHI [7]. It is the first large time projection gas calorimeter which provides a full three-dimensional reconstruction of an electromagnetic shower. It covers the angular region $41°30' < \theta < 138°30'$. The HPC consists of 144 modules arranged in 6 rings inside the cryostat of the magnet. Each ring consists of 24 modules concentric arranged around the Z-axis with an inner radius of $208cm$ and an outer radius of $260cm$. The inner and the middle ring

[3]DELANA : the **DEL**phi **ANA**lysis program

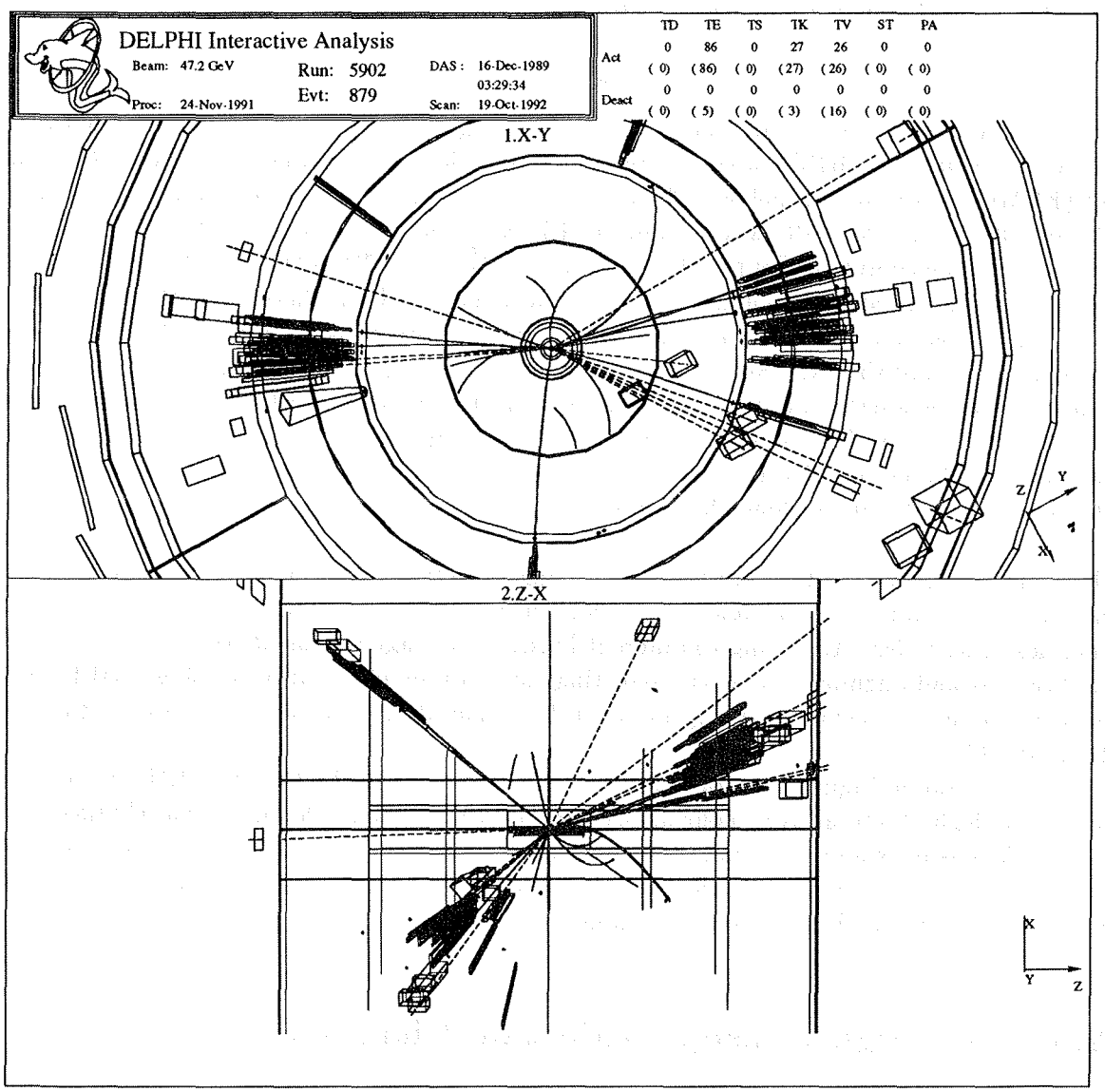

Figure 2.5: *A three-jet event recorded with the DELPHI detector and visualized with the DELGRA event display program. The individual charged tracks are drawn as lines and hits in the calorimeters as boxes. The upper and lower plot show the views in direction and perpendicular to the direction of the beam pipe.*

modules have a length of $85cm$, the outer ring modules are shorter with a length of $65cm$. It has to be mentioned that only part of the whole volume is sensitive for charge detection, because of *cracks* between the modules. That means that in ϕ-direction each 15° we find a crack. Also for $\theta = 49°, 67°, 90°, 113°$ and for $\theta = 131°$, volumes of a few cm thickness are not sensitive to charge.
In principle each HPC module is a TPC with layers of a high density material in the gas

volume where electromagnetic showers are initiated. The converter thickness varies between 18 and 22 *radiation length* depending on the angle θ. Each HPC module consists of 40 planes of lead with a thickness of about $3mm$. The 39 gas gaps are $8mm$ thick and are filled with an argon/methane (80/20%) gas mixture. An entering electron converts its energy in the lead planes by the multiple effects of *bremsstrahlung* and *pair production* in a sample of electrons, positrons and photons. These particles deposit part of their energy in the drift gap by ionization processes. The resulting charge cloud drifts in a nearly homogeneous electric field ($E = 106V/cm$) which is parallel to the $\vec{B}$ field to the read-out proportional chambers. The electric drift field is produced by 500 (382) lead wires in the case of long (short) modules. Altogether they form a structure similar to an accordion, where the potential difference between two wires is $\Delta U = 18V$. It is interesting to realize that the lead wires act as the converter of the calorimeter and as the source of the drift field. Figure 2.6 shows some details of the construction of a HPC module.

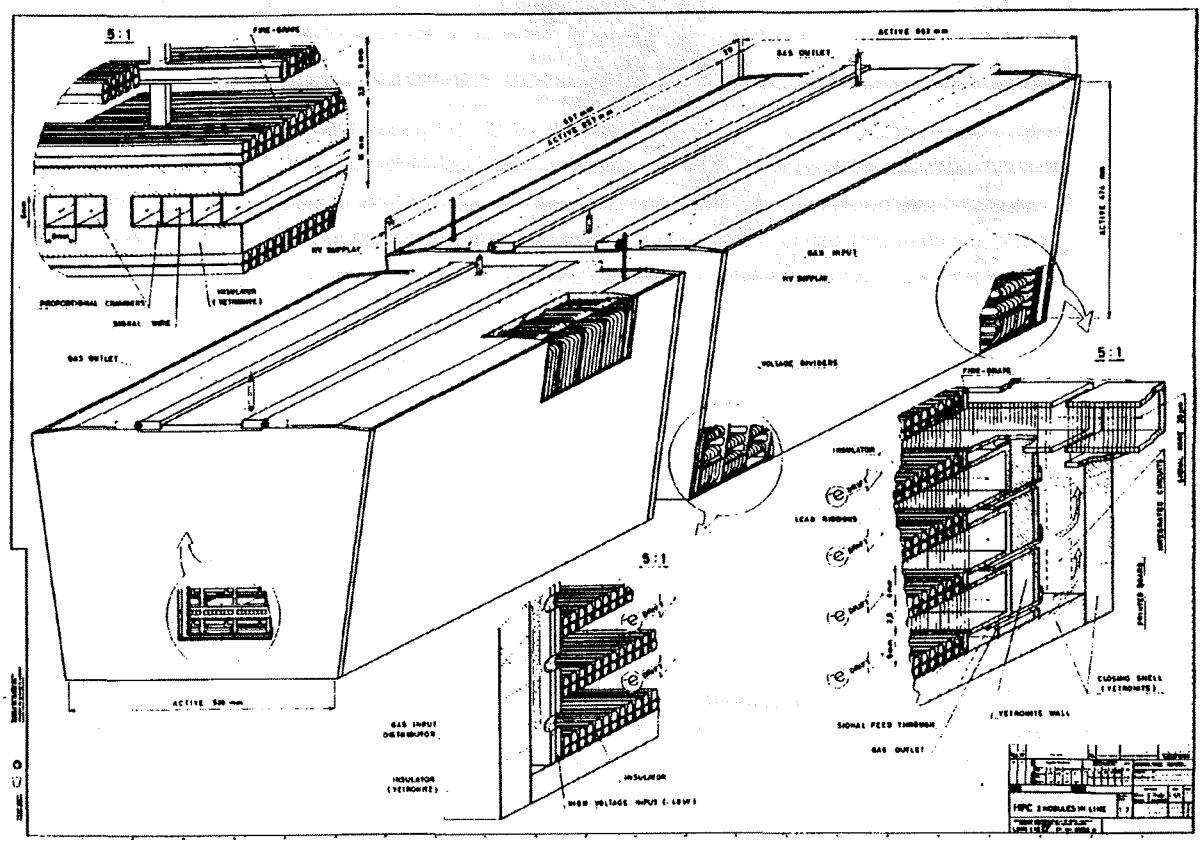

Figure 2.6: *Schematic view of the High Density Projection Chamber (HPC)*

The read-out of a single module is done by a planar MWPC[4] which consists of 39 sense wires and is segmented in 128 pads. Each pad is read out as an individual electronic channel. This corresponds to 18432 channels for the whole HPC. For each module these pads are grouped into 9 parallel rows. In order to get better spatial resolution different pad sizes were chosen for different layers. In the first three rows there are small pads each containing 3 drift gaps. The next three rows consist of medium pads with 4 drift gaps. The large pads in the rows 7, 8 and 9 contain 6 drift gaps. The Figures 2.7 and 2.8 show the layer structure of a HPC module and the different pad sizes of the read-out chamber.

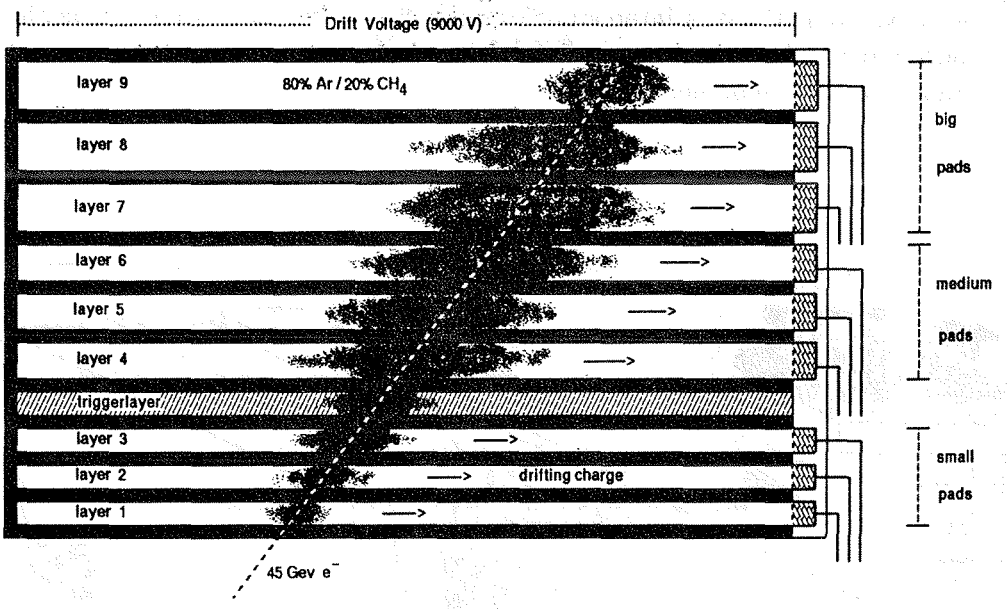

Figure 2.7: *Schematic view of the layer structure of a single HPC module.*

The information about the Z-coordinate is given by the drift time. The granularity depends on the sampling time of the flash ADC's which is about $68ns$; this corresponds with a drift velocity of $5.5cm/\mu s$ to about $3.7mm$. Since 256 flash intervals of $68ns$ are read out a total time of $17.4\mu s$ is needed. This is less than the time between two BCO's ($22\mu s$).[5] Using all this information, we are left with nearly five million pulse heights which are potentially present per event in the HPC.

Since it takes $17.4\mu s$ to read the signal from the HPC it can not be used as a trigger for the detector. Therefore plastic scintillators were installed in each module. They deliver a prompt signal ($< 1\mu s$) if an e^+, e^- or a photon showers in the HPC. The scintillators are installed after 4.5 radiation length (the location of the maximum of a 3 GeV shower). They are read out by photomultipliers via optical fibres [9].

[4] MWPC: multi-wire proportional chamber

[5] BCO: beam crossing over

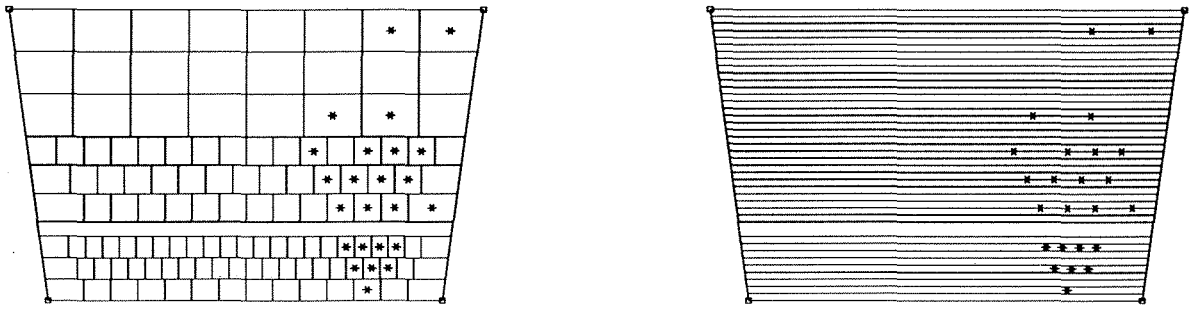

Figure 2.8: *Pad geometry and lead distribution of a single HPC module visualized with HPCGRAPH.*

2.3.2 The HPC Offline Software

Each sub-detector of DELPHI provides its own software for the offline DELANA processings. The HPC analysis program is called HPCANA [10]. It converts the raw data information into physics information (e.g. momenta and energies of partricles) and provides the necessary energy calibration and alignment. The philosophy applied in the HPC pattern recognition is hierarchical in structure. After a first stage pattern recognition is performed, a second stage phase will follow where the information from other sub-detectors is used in addition.

In the first stage pattern recognition phase only HPC information is used. Starting from the charge strings as they are recorded from the data aquisition a first threshold is applied and a *cluster* is defined by the consecutive time buckets above that threshold. If the width of the cluster is large, a higher threshold is applied, and one or more new clusters can be found. The values for the threshold, together with the width cuts, have been determined by studying Monte Carlo and data in order to be sensitive to the full HPC dynamic range (e.g from minimal ionizing particles to highly energetic showers).

For the shower reconstruction neighbouring clusters are associated to each other. In addition, a loose vertex constraint is applied. Therefore, the energy of the clusters is projected in θ and ϕ in 1° bins onto an unitary sphere. After a search for the local maximum is performed, the energy of neighbouring bins, consistent with the transverse dimensions of an electromagnetic shower, is added to the shower energy.

During a second stage pattern recognition, the information from the other sub-detectors, especially from the tracking detectors, is used to search for showers. Therefore the track information of ID, TPC and OD is extrapolated to the HPC giving a hint for the expected shower starting point and direction. Such additional guidance is necessary in order to find also low energetic showers (e.g. from pions) which consist typically only of a few clusters.

Chapter 3

Electromagnetic Showers in Sampling Calorimeters

3.1 Sampling Calorimeter

High energetic particles ($E \gg mc^2$) in matter predominantly lose their energy due to the production of secondary particles in inelastic interactions. If the secondary particles are able to produce new particles again in inelastic collisions, this leads to the development of a particle *shower*. When the energy of the particles has decreased to a certain amount, other mechanisms of energy loss become increasingly important. The low energetic particles do not contribute to the development of the shower anymore, but they lose their energy in inelastic atomic collisions (*ionization / excitation*). Electrons produced by ionization or photons from the excited atoms can be collected and converted into an electronic signal.

In high energy physics a calorimeter denotes a detector in which the particle energy is absorbed and transformed into an electronic signal ([12], [13], [14]). The measured signal is preferably proportional to the energy of the incident particle, which can only be achieved if the energy of the particle is absorbed completely in the calorimeter. This can only be realized with dense materials, either transparent crystals of a dense material like NaI[1] or BGO[2] or just solid materials like lead or iron.

A calorimeter can be built in a way that particle multiplication and signal development take place in the same material. With these *homogeneous* calorimeters a very high energy resolution can be obtained but the materials used (NaI, BGO, lead glass) are expensive and hard to treat. Spatial resolution and particle separation of these homogeneous calorimeters are determined by the segmentation of the used crystals and the corresponding read-out. Water can also be used in a calorimeter, but huge dimensions are needed to absorb high energetic showers.

In order to reduce the dimensions of the calorimeter and to minimize the costs, it is sometimes better to build a calorimeter as a *sandwich*. Here passive layers of high mass and charge density (e.g. lead) are interleaved by active layers of low density. The passive layers are re-

[1] sodium iodide

[2] bismuth germanate

sponsible for particle multiplication, the active layers are responsible for the measured signal. The signal from the active layers is, therefore, only a sample of the total deposited energy. Such a calorimeter is called *sampling* calorimeter.

As will be shown in the next sections the main effects for electromagnetic particle multiplication are the processes of bremsstrahlung and pair production. In order to get high cross sections for these processes, materials with high atomic number Z are chosen for the passive layers. The passive layers should be thin to obtain, for a constant ratio of absorber to active material, a maximum number of active layers. In this way the statistical fluctuations (sampling fluctuations) of the measured energy can be minimized. The sampling fluctuations are directly correlated to the energy resolution of the electromagnetic calorimeter.

In calorimeters which are built to measure hadronic showers[3], the influence of the sampling fluctuations on the energy resolution is very small. The dominating contribution to the energy resolution comes from intrinsic fluctuations of the hadronic shower development. The choice of the absorption and the active material and their density range is different from the case of an electromagnetic calorimeter. The scale which describes the spatial development of a hadronic shower is the interaction length λ. Compared to the small radiation length[4], which describes the development of an electromagnetic shower, the interaction length is much larger. Therefore, hadron calorimeters have to be more massive than electromagnetic calorimeters. That means that the price of the used absorber material plays an important role. Frequently used materials for hadron calorimeters are uranium ($\lambda = 12.0cm$), iron ($\lambda = 17.1cm$) and lead ($\lambda = 18.5cm$).

By using a fine segmentation of the active read-out layers, not only the energy of the incident particle can be measured, but also the extension and direction of the shower can be obtained. This spatial information can be used for particle separation and for particle identification.

The following sections will describe some physical effects of particle detection. The complete and correct treatment of this effects has to be done by calculations of quantum electrodynamics (QED). The purpose of these sections is to point out the main effects for the understanding of a calorimeter like the HPC.

3.2 Interaction of Heavy Charged Particles with Matter

In general, two principal effects characterize the passage of charged particles through matter: (a) the loss of energy by the particle (b) the deflection of the particle from the incident direction. These effects are the consequences of the two processes:

1) inelastic collisions with the electrons of the atom
2) elastic scattering from nuclei

These reactions occur very often per unit path length in matter. So the sum of all these

[3] In a hadronic shower particle multiplication arises due to inelastic hadronic reactions of the incident hadron with the nuclei of the absorber.

[4] The definition of the radiation length will be given in section 3.3.3.

reactions leads to the two observed effects of energy loss and angular deflection[5]. These, however, are not the only reactions which can occur. Other possible processes are:

3) emission of Cherenkov radiation
4) nuclear reactions
5) bremsstrahlung.

In comparison to the atomic collision process, they are extremely rare. Therefore, these processes are only mentioned here. For reasons which become clearer in the following sections, it is necessary to separate the descriptions of heavy charged particles from the description of electrons and positrons. The group of the heavy charged particles includes for example the following particles: pion, proton, α-particle and other light nuclei. Heavy ions are excluded from this discussion because they are irrelevant in e^+e^- detectors.

Inelastic collisions are the main source of energy loss of heavy charged particles. In these collisions, energy is transferred from the particle to the atom of the matter by ionization or by excitation. Normally, the amount of energy which is transferred to the atom is very small compared to the kinetic energy of the particle. Since the number of collisions per unit path length for normal material is huge, the particle can lose a substantial part of its energy by passing only a few centimeters of matter. These atomic collisions are divided into two groups: *soft* collisions which are only causing excitation and *hard* collisions which are causing ionization. For highly energetic particles the hard collisions are responsible for the main energy loss in matter. In some of the hard collisions enough energy is transferred such that the liberated electron itself causes secondary ionization. The highly energetic recoil electrons are sometimes called *δ-rays* or *knock-on* electrons.

The second process, the elastic scattering on nuclei does not occur as often as the first process. In general very little energy is transferred because the mass of the nucleus is much higher than the mass of the incoming particle. In special cases (e.g. α-particles in hydrogen) the particles can lose some energy through this mechanism but the major part of energy is still lost due to the first process.

Niels Bohr first calculated the energy loss per path length (dE/dx) using classical arguments. Later Bethe and Bloch derived a more consistent formula using the tools of quantum mechanics. The quantity dE/dx is known as the *stopping power*.

3.2.1 Bethe-Bloch-Formula

The derivation of the Bethe-Bloch-formula requires the framework of QED and is outside of the scope of this paper. Nevertheless it is very instructive to follow a classical argument. Using such an argument the energy loss per path length is caused by the electromagnetic processes of excitation and ionization which occur in the field of the entering charged particles. A simplified version of this argument can be found in [16]. In this section the result of the complete QED calculations is given. Formula 3.1 is known as the *Bethe-Bloch-formula* and is the basic expression for energy loss calculations [15]:

$$-\frac{dE}{dx} = 2\pi N_A r_e^2 m_e c^2 \rho \frac{Z}{A}\frac{z^2}{\beta^2}\left[\ln\left(\frac{2m_e v^2 W_{max}}{I^2(1-\beta^2)}\right) - 2\beta^2\right] \tag{3.1}$$

[5] More quantitative calculations can be found in Ref. [15].

with:

r_e :	classical electron radius	A :	atomic weight of absorber
m_e :	electron mass	ρ :	density of absorbing material
c :	speed of light	z :	charge of incident particle [e]
N_A :	Avogadro's number	v :	velocity of incident particle
I :	mean excitation potential	β :	v/c of incident particle
Z :	atomic number of absorber	W_{max} :	max. E transfer in a single collision

The maximum energy transfer W_{max} for a single collision can be derived by a kinematical argument. Using $\varepsilon = m_e/M$ and $\eta = \beta/\sqrt{1-\beta^2}$ for an incident particle with mass M the following formula can be derived:

$$W_{max} = \frac{2m_e c^2 \eta^2}{1 + 2\varepsilon\sqrt{1+\eta^2} + \varepsilon^2} \tag{3.2}$$

At non-relativistic energies, dE/dx in the Bethe-Bloch-formula is dominated by the overall $1/\beta^2$ factor. By increasing the velocity to $v \simeq 0.96c$ a minimum is reached. Particles at this point and beyond this minimum are called *minimal ionizing particles (mip's)*. The minimum value of dE/dx is almost the same for particles of the same charge. By increasing the velocity beyond this minimum the overall $1/\beta^2$ factor becomes almost constant and a small rise is caused by the logarithmic term in equation 3.1. This small rise is known as the *relativistic rise* in the Bethe-Bloch-formula. Figure 3.1 shows the curve of the stopping power dE/dx as a function of energy for different particles.

In the non-relativistic region, a separation of particles with different masses is easily possible. In the relativistic region, this becomes impossible because of the nearly vanishing mass dependence of the Bethe-Bloch-formula.

In order to get better agreement with experimental results, in practice two corrections are normally added to the Bethe-Bloch-formula: the *density effect* correction δ and the *shell* correction C [15]:

$$-\frac{dE}{dx} = 2\pi N_A r_e^2 m_e c^2 \rho \frac{Z}{A}\frac{z^2}{\beta^2}\left[\ln\left(\frac{2m_e v^2 W_{max}}{I^2(1-\beta^2)}\right) - 2\beta^2 - \delta - 2\frac{C}{Z}\right] \tag{3.3}$$

The quantities δ and C are corrections to the Bethe-Bloch-formula, which are important only for high and low energies. The density effect comes from the fact that the electric field of the particle polarizes the surrounding atoms along its path. Electrons which are far away from the path will be shielded from the full electric field, so that collisions with these electrons contribute less to the energy loss than it was predicted in the Bethe-Bloch-formula. This effect and the polarization are depending on the density of the matter. The shell corrections describe the effect which occurs when the velocity of the incident particle is smaller than or equal to the orbital velocity of the bound electron. Then the assumption that the electron is stationary relative to the incident particle is no longer valid. The quantities δ and C can be parametrized as a function of particle energy and some characteristic values of the absorbing material[6].

[6] For more details see Ref. [15].

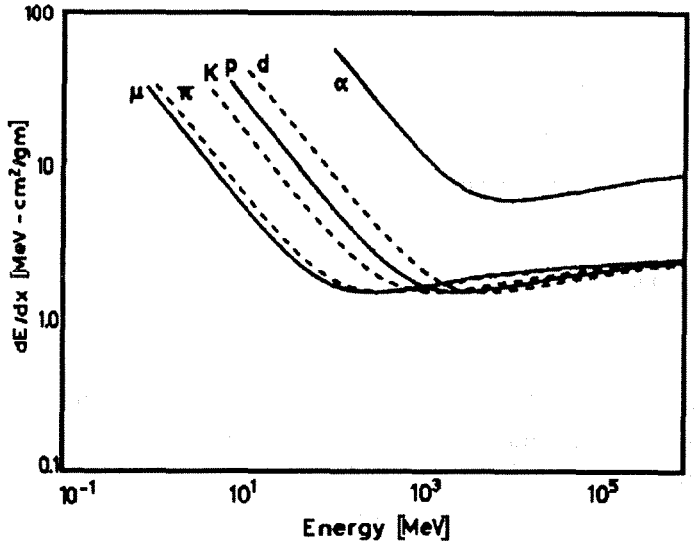

Figure 3.1: *The stopping power dE/dx as a function of energy for different particles [15].*

3.2.2 Limitations of the Bethe-Bloch-Formula

For elementary particles and nuclei up to the mass of the α-particle the formula gives predictions within a few percent of accuracy. The velocities can range from $v \simeq 0.1c$ up to the relativistic region. For velocities $v \leq 0.05c$ the Bethe-Bloch-formula breaks down, because the velocity of the incident particle is similar to the velocity of the orbital electrons. At this point some complicated effects come into play. The most important process is that the particle tries to pick up electrons from the surrounding matter for some time[7].
In materials with a symmetric atomic structure, i.e. crystals, the Bethe-Bloch-formula can only be applied with care. If the particle enters a crystal with a very small angle relative to the symmetry axis, the particle can suffer a series of correlated small-angle scatterings which guide the particle through the crystal. Because of this effect, particles do not cause as many ionizations inside the crystal as predicted in the Bethe-Bloch-formula. So the particles can travel a much longer distance inside a crystal than inside an amorphous material. This effect is known as *channeling effect*[8].

3.3 Interaction of Electrons and Positrons with Matter

In addition to the energy loss of heavy charged particles, as discribed in the previous sections, for electrons and positrons another effect becomes very important: the emission of electromagnetic radiation from the scattering in the field of a nucleus (*bremsstrahlung*). At energies of a few MeV or less this effect is very small. At higher energies the probability for bremsstrahlung rises very strongly and for energies of a few GeV this effect dominates

[7] Some empirical formulae for this energy region can be found in Ref. [15].

[8] For more details see Ref. [13], [15].

completely.

Therefore, the total energy loss for electrons and positrons is composed of two parts:

$$\left(\frac{dE}{dx}\right)_{total} = \left(\frac{dE}{dx}\right)_{coll} + \left(\frac{dE}{dx}\right)_{brems} \tag{3.4}$$

3.3.1 Collision Loss

The processes of inelastic collisions are very similar to the processes of heavy charged particles. The Bethe-Bloch-formula from the previous section has to be modified slightly because of two reasons. The first is the very small mass of the electron. This is causing a deflection of the incident electrons during the collision process. In the derivation of the Bethe-Bloch-formula for heavy charged particles this deflection is neglected. The second reason is that with electrons the collision happens between identical particles and one can not distinguish between them. The maximal energy transfer per collision W_{max} is now exactly the half of the incident kinetic energy. These changes in the assumptions lead to the following Bethe-Bloch-formula [15]:

$$-\left(\frac{dE}{dx}\right)_{coll} = 2\pi N_A r_e^2 m_e c^2 \rho \frac{Z}{A}\frac{1}{\beta^2}\left[\ln\left(\frac{\tau^2(\tau+2)}{2(I/m_e c^2)^2}\right) + F(\tau) - \delta - 2\frac{C}{Z}\right] \tag{3.5}$$

where τ is the kinetic energy in units of $m_e c^2$. $F(\tau)$ is given by the following expression

$$F(\tau) = 1 - \beta^2 + \frac{\tau^2/8 - (2\tau+1)\ln 2}{(\tau+1)^2} \tag{3.6}$$

for electrons, and

$$F(\tau) = 2\ln 2 - \frac{\beta^2}{12}\left(23 + \frac{14}{\tau+2} + \frac{10}{(\tau+2)^2} + \frac{4}{(\tau+2)^3}\right) \tag{3.7}$$

for positrons.

As it can be seen from equation 3.5, the energy loss due to inelastic collisions varies nearly logarithmically in energy (for $\beta \simeq 1$) and nearly linear in Z.

3.3.2 Bremsstrahlung

If a charged particle crosses the electric field of a nucleus it is accelerated. Because of this acceleration the particle emits electromagnetic radiation. This radiation is called *bremsstrahlung*. Figure 3.2 shows the nature of this process.

At LEP energies electrons and positrons are the only particles which lose a substantial part of their energy via bremsstrahlung. This can be seen from the cross section of bremsstrahlung which is presented below ($\sigma \propto r_e^2 = (e^2/mc^2)^2$). Because of their very small mass the cross section for electron bremsstrahlung is a factor of 40000 higher than for the next lightest particle, the muon (m=106 MeV).

Bremsstrahlung is dependent on the strength of the electric field of the nucleus. Therefore the screening of the electrons of the atom plays an important role. Thus the cross section for

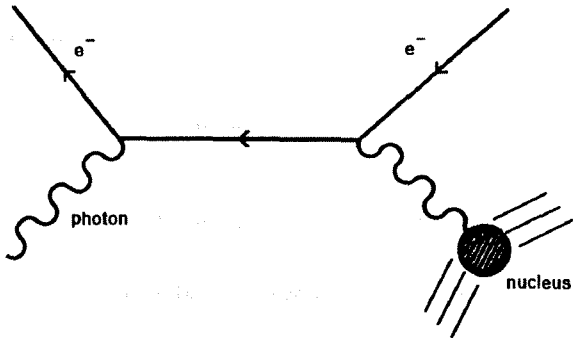

Figure 3.2: *The process of Bremsstrahlung. An electron gets accelerated in the field of a nucleus and radiates a photon.*

bremsstrahlung depends on the energy of the particle, the charge of the nucleus Z and the screening by the electrons. For the case $\eta = 100 m_e c^2 h\nu / E_0 E Z^{1/3} \simeq 0$, the cross section in Born approximation can be written in the following form [15]:

$$d\sigma = 4Z^2 r_e^2 \alpha \frac{d\nu}{\nu} \left[\left(1 + \varepsilon^2 - \frac{2\varepsilon}{3} \right) \ln(183 Z^{-1/3}) + \frac{\varepsilon}{9} \right] \tag{3.8}$$

where $h\nu$ is the energy of the emitted photon, E_0 (E) is the energy of the incident particle before (after) the radiation and ε corresponds to $\varepsilon = E/E_0$.
The energy loss from radiation can now be calculated by integrating the cross section times the photon energy over the allowable energy range [15]:

$$-\left(\frac{dE}{dx}\right)_{brems} = n \int_0^{\nu_0} h\nu \frac{d\sigma}{d\nu}(E_0, \nu) d\nu \tag{3.9}$$

where n: number of atoms/cm^3 and $\nu_0 = E_0/h$.
This leads to the following result ($E_0 \gg 137 m_e c^2 Z^{1/3}$, $\eta \simeq 0$):

$$-\left(\frac{dE}{dx}\right)_{brems} = 4nE_0 Z^2 r_e^2 \alpha \left[\ln(183 Z^{-1/3}) + \frac{1}{18} \right] \tag{3.10}$$

In this case the energy loss by bremsstrahlung varies nearly linear in energy, which leads to complete dominance of this effect at very high energies. The dependence on Z is nearly quadratic. These results are only valid for bremsstrahlung which is emitted in the field of a nucleus. A second possible process is the emission of *electron-electron* bremsstrahlung. It can be shown that this can be included by replacing Z^2 by $Z(Z+1)$.

The energy loss due to radiation has large fluctuations. It can happen that all the radiated energy is emitted in one or two photons. In contrast, the energy loss due to inelastic collisions is a very continuous process. Just because of this effect, the development of electromagnetic showers is possible, as will be described later.

3.3.3 Radiation Length

A *radiation length* is defined as the distance over which the electron energy is reduced to $1/e$ of its original energy. For this definition, only radiation losses are considered. Indeed, if one

rewrites formula 3.10 ignoring in the high energy limit the collision losses one arrives at the following result [15]:

$$-\frac{dE}{E} = \frac{1}{X_0}dx \tag{3.11}$$

$$\frac{1}{X_0} \simeq 4nZ(Z+1)r_e^2\alpha\left[\ln(183Z^{-1/3})\right] \tag{3.12}$$

where X_0 is called *radiation length.* Integration of formula 3.11 leads to the familiar exponential law:

$$E = E_0 \exp\left(\frac{-x}{X_0}\right) \tag{3.13}$$

Table 3.1 lists the radiation length for some materials. The usefulness of the concept of radiation length becomes clear if one measures the thickness of materials in these units. Formula 3.11 then becomes $-(dE/dt) \simeq E_0$, where t is the distance in radiation length. From these considerations, one can easily see, that the energy loss in terms of radiation lengths is roughly independent of the material type.

3.3.4 Critical Energy

The energy loss dE/dx by bremsstrahlung depends on the absorbing material and the energy of the incident particle. For a certain energy, the losses by bremsstrahlung are exactly equal to the losses from inelastic collisions. This energy is called the *critical* energy E_c.

$$\left(\frac{dE}{dx}\right)_{coll} = \left(\frac{dE}{dx}\right)_{brems} \quad for \quad E = E_c \tag{3.14}$$

It is a characteristic energy for different absorbing materials. Table 3.1 gives a list of the critical energies for some commonly used materials. The critical energy can be approximated by the following formula due to *Bethe* and *Heitler* [17]:

$$E_c \simeq \frac{1600 \cdot m_e c^2}{Z} \tag{3.15}$$

Material	Critical Energy [MeV]	Radiation Length [cm]
Pb	9.51	0.56
Al	51.0	8.9
Fe	27.4	1.76
Cu	24.8	1.43
Air	102	30050
NaI	17.4	2.59
H_2O	92	36.1
Polystyrene	109	42.9

Table 3.1: *Critical energies and radiation lengths for some materials [15].*

Figure 3.3 shows the fractional energy loss for the different interaction processes of electrons and positrons with matter. For low energies, the process of ionization is the most important reaction. For higher energies, the effect of bremsstrahlung dominates completely. The effects of Møller, Bhabha scattering or positron annihilation play only a role in the low energetic end of the spectrum.

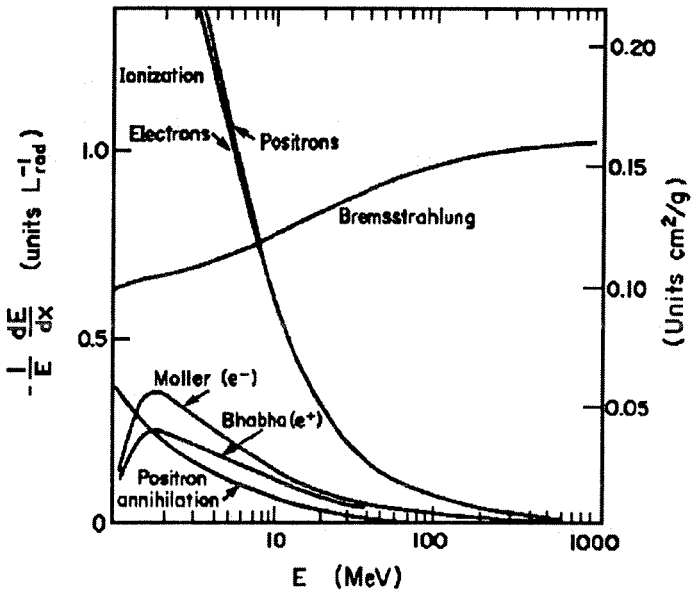

Figure 3.3: *Fractional energy loss for electrons and positrons in lead [18].*

3.4 Multiple Coulomb Scattering

In addition to inelastic collisions with atomic electrons, charged particles can suffer elastic Coulomb scatterings from nuclei. Ignoring spin effects and screening these collisions are individually described by the well-known Rutherford formula [19]:

$$\frac{d\sigma}{d\Omega} = z^2 Z^2 r_e^2 \frac{mc/\beta p}{4\sin^4(\theta/2)} \tag{3.16}$$

If we assume that the nucleus is much more massive than the incident particle, we can neglect the energy transfer. Because of the $1/\sin^4(\theta/2)$, dependence the major effect of this process is a small angular deflection of the particle. Depending on thickness and density of the material one can distinguish between three cases: *Single Scattering*, *Plural Scattering* and *Multiple Scattering*. The multiple scattering with more than 20 scatterings can be treated statistically. In this case the particle follows a random zigzag path.

The effect of multiple scattering is important for the lateral development of a shower. For its description the typical scale unit of one *Molière* radius R_M is used. The Molière radius

R_M results from the theory of multiple scattering, if one describes the lateral development of an electron beam with the energy E_c passing through an absorber with the thickness of $1X_0$:

$$1R_M = \frac{E_{MS}}{E_c} X_0 \tag{3.17}$$

$$E_{MS} = m_e c^2 \sqrt{\frac{4\pi}{\alpha}} \approx 21.2\ MeV \tag{3.18}$$

The Molière radius is used for the material independent description of the transverse shower development (similar to the unit of one radiation length for the longitudinal development). It can approximately be calculated from the atomic mass (A) and the atomic number (Z) of the material [20]:

$$1R_M \simeq 7\frac{A}{Z} X_0 \quad \left(\frac{\Delta R_M}{R_M} < \pm 10\% \ for\ 13 \leq Z \leq 92\right) \tag{3.19}$$

Lead e.g. has a critical energy of 9.51 MeV. Using equation 3.17 leads to the unit of one Molière radius:

$$1R_M = 2.23X_0 = 1.25cm \quad for\ lead \tag{3.20}$$

3.5 Interaction of Photons with Matter

The interaction of photons with matter is completely different from the behaviour of charged particles. Photons are not able to have as many inelastic collisions with atomic electrons, because of their lack of charge. The main effects of their interaction with matter are:

1) Photoelectric Effect
2) Compton Scattering
3) Pair Production

3.5.1 Photoelectric Effect

The photoelectric effect describes the effect of photon absorption by an atomic electron of the material. The kinetic energy of the ejected electron is equal to the photon energy reduced by the binding energy B of the atom:

$$E_{kin} = h\nu - B \tag{3.21}$$

This effect cannot occur with free electrons, because of the conservation of energy and momentum. The nucleus of an atom is needed to absorb the recoil momentum. Theoretically, the cross section for the photoelectric effect is difficult to compute, because of the complicated Dirac wavefunctions of the atomic system. The typical shell structure of an atom can be observed if one plots the cross section versus the photon energy. For energies above the K-shell the K-electrons are almost always involved in the photoelectric reaction. If we assume this,

the cross section for energies in the MeV region ($h\nu \ll m_e c^2$) can be calculated by using a Born approximation [15]:

$$\sigma_{ph} = \frac{8\pi}{3} r_e^2 4\sqrt{2} Z^5 \alpha^4 \left(\frac{m_e c^2}{h\nu}\right)^{7/2} \tag{3.22}$$

Note especially, that the dependence of the cross section on the atomic number (Z) goes as the 5th power. The dependence on the energy is proportional to $(h\nu)^{-7/2}$.

3.5.2 Compton Scattering

Compton scattering describes the scattering of photons on free electrons. In matter the atomic electrons are bound. If the energy of the photon is high compared to the binding energy of the electrons, one can neglect the binding energy and consider the electrons as essentially free. Figure 3.4 describes the process of Compton scattering. From easy calculations of energy and

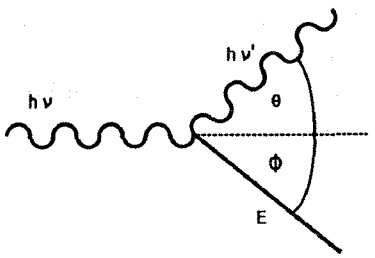

Figure 3.4: *Kinematics of Compton scattering.*

momentum conservation one can derive the following relations [15]:

$$h\nu' = \frac{h\nu}{1 + \varepsilon(1 - \cos\theta)} \tag{3.23}$$

$$E_{kin} = h\nu - h\nu' = h\nu \frac{\varepsilon(1 - \cos\theta)}{1 + \varepsilon(1 - \cos\theta)} \tag{3.24}$$

$$\cot\phi = (1 + \varepsilon)\tan\frac{\theta}{2} \tag{3.25}$$

where $h\nu$, $h\nu'$ and E_{kin} are the energies of the scattering particles, and ε is defined as $\varepsilon = h\nu/m_e c^2$. The energy loss of the photon is a function of the scattering angle θ. It will be maximal in the case of back-scattering ($\theta = \pi$):

$$E_{max} = h\nu \frac{2\varepsilon}{1 + 2\varepsilon} \tag{3.26}$$

and is known as the *Compton edge.*
The cross section for Compton scattering was one of the first results of quantum electrodynamics. It is known as the *Klein-Nishina formula*:

$$\frac{d\sigma}{d\Omega} = \frac{r_e^2}{2} \frac{1}{[1 + \varepsilon(1 - \cos\theta)]^2} \left(1 + \cos^2\theta + \frac{\varepsilon^2(1 - \cos\theta)^2}{1 + \varepsilon(1 - \cos\theta)}\right) \tag{3.27}$$

The total probability per electron for Compton scattering can be obtained by integration of this formula over $d\Omega$:

$$\sigma_c = 2\pi r_e^2 \left[\frac{1+\varepsilon}{\varepsilon^2} \left(\frac{2(1+\varepsilon)}{1+2\varepsilon} - \frac{\ln(1+2\varepsilon)}{\varepsilon} \right) + \frac{\ln(1+2\varepsilon)}{2\varepsilon} - \frac{1+3\varepsilon}{(1+2\varepsilon)^2} \right] \tag{3.28}$$

Figure 3.5 shows the total cross section for Compton scattering as a function of photon energy. One notices that Compton scattering is only dominant in the region of low energies ($\approx 1\ MeV$), because of the $1/(h\nu)^2$ energy dependence. The dependence on Z is linear, because of the Z electrons per atom.

3.5.3 Pair Production

Pair production describes the conversion of an initial photon into an electron-positron pair. This process is not possible in the vacuum, because of conservation of energy and momentum. Usually the process occurs near a nucleus or an atomic electron which is carrying away the missing energy and momentum. Moreover, to create an e^+e^-pair, the photon has to have at least an energy of $E = 2m_ec^2 = 1.022\ MeV$.

Theoretically, the pair production process is very similar to bremsstrahlung because of the very similar Feynman diagrams (in Figure 3.2, change the time axis). In the case of high energies ($h\nu \gg 137 m_e c^2 Z^{-1/3}$, $\eta \simeq 0$), the following stopping power can be obtained:

$$-\left(\frac{dE}{dx}\right)_{pair} = 4nE_0Z(Z+1)r_e^2\alpha \left[\frac{7}{9}\ln(183Z^{-1/3}) - \frac{1}{54}\right] \tag{3.29}$$

From this, it is interesting to compute the mean free path, X_{pair}, for photons due to pair production. Comparison of equations 3.11 and 3.12 neglecting the small constant term delivers the following results:

$$\frac{1}{X_{pair}} \simeq \frac{7}{9} 4nZ(Z+1)r_e^2\alpha \left[\ln(183Z^{-1/3})\right] \tag{3.30}$$

$$X_{pair} \simeq \frac{9}{7} X_0 \tag{3.31}$$

The cross section for pair production behaves for low energies logarithmically and reaches for high energies a stable limit. This implies that for typical LEP energies of a few GeV the effect of pair production dominates completely. The dependence on Z is proportional to $Z(Z+1)$.

3.6 Simple Shower Models

One of the most interesting and useful results of the combined effects of bremsstrahlung and pair production of highly energetic electrons and photons is the formation of electromagnetic showers. As the HPC is designed based on these effects, a discussion of shower models is important. An energetic photon in matter converts into an electron-positron pair. Each of these leptons emits then an energetic bremsstrahlung photon. These photons convert again into e^+e^-pairs and so on. The result is a cascade or a shower of photons, electrons and positrons. This cascade stops when the energy of the pair produced leptons reaches the critical energy

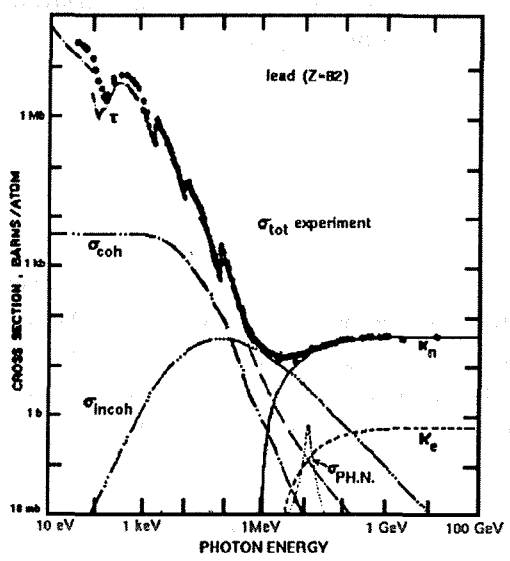

Figure 3.5: *Photon total cross sections as a function of energy in lead, showing the contributions of the different processes: τ = atomic photo-effect (electron ejection, photon absorption), σ_{COH} = Coherent scattering (Rayleigh scattering-atom neither ionized nor excited), σ_{INCOH} = Incoherent scattering (Compton scattering), κ_n = pair production in nuclear field, κ_e = pair production in electron field, $\sigma_{PH.N.}$ = Photonuclear absorption (nuclear absorption, usually followed by the emission of a neutron or another particle) [18].*

E_c. In order to describe the electromagnetic shower in a material-independent way, we work with the following simplifications:

- the cross sections for the different processes are equal for electrons and for positrons
- the cross sections for bremsstrahlung and pair production are taken in their high energy limits
- effects of multiple and Compton scattering are neglected
- the energy loss per radiation length due to ionization is continuous and constant

The development of a shower is a statistical process. With the following assumptions one can try to describe the number of particles and their mean energy as a function of radiation lengths in the converting material:

- Each $e^-(e^+)$ with $E > E_c$ radiates within one radiation length a photon

$$e \rightarrow e' + \gamma \ with \ E_\gamma = E_e/2 = E_{e'} \ . \tag{3.32}$$

- Each photon with $E > E_c$ converts within one radiation length into an e^+e^-pair

$$\gamma \rightarrow e^- + e^+ \ with \ E_{e-} = E_{e+} = E_\gamma/2 \ . \tag{3.33}$$

After t radiation lengths we find for a shower which was initiated from an electron, positron or a photon of energy E_0 a total number of particles:

$$N(t) = 2^t \ , \tag{3.34}$$

each with an average energy of

$$E(t) = \frac{E_0}{2^t} \ . \tag{3.35}$$

Figure 3.6 gives a schematic view of the electromagnetic shower development. Now let us compute the maximum penetration length of this cascade. We assume that for particles with $E > E_c$ the energy loss is only caused by the processes of bremsstrahlung and pair production. Particles with $E \leq E_c$ lose their energy abruptly due to ionization ([21], approximation A). This means that the shower can penetrate maximal to a depth t_{max} where the energy of the single particles drops down to $E(t_{max}) = E_0/2^{t_{max}} = E_c$. This leads to the maximum penetration length:

$$t_{max} = \frac{\ln(E_0/E_c)}{\ln 2} \ , \tag{3.36}$$

and to the maximum number of produced particles

$$N_{max} = 2^{t_{max}} = \frac{E_0}{E_c} \ . \tag{3.37}$$

The maximum penetration length rises logarithmically with the incident energy E_0 of the particle, so that compact calorimeters can be built even for high energies.

Responsible for the formation of the shower signal are all charged particles (2/3) in the shower. Therefore, it is necessary to compute the mean total path length $< T >$:

$$< T > [X_0] = \frac{2}{3} \int_0^{t_{max}} N(t) dt \tag{3.38}$$

$$= \frac{2}{3 \ln 2} \left(\frac{E_0}{E_c} - 1 \right) \tag{3.39}$$

$$\approx \frac{E_0}{E_c} \tag{3.40}$$

The mean path length $< T >$ is nearly proportional to the energy of the incident particle. This result is fundamental for the usage of calorimeters in high energy physics.

This simple model can only give a very rough picture of the real development of a shower. The approximation that only particles with $E \leq E_c$ lose energy due to ionization is too crude for more detailed studies. Therefore, in approximation B [21], it is allowed that also particles with $E > E_c$ lose an energy E_c per radiation length due to ionization. The calculations of the shower development are now much more complicated, because this ionization energy is no longer available for particle production. One can derive expressions for the maximum $t_{max}[X_0]$, the center of gravity $t_{cog}[X_0]$ and the variance $\sigma_t^2[X_0^2]$ for photon and electron induced shower distributions:

$$t_{max,\gamma} = 1.01 \left[\ln \left(\frac{E_0}{E_c} \right) - \frac{1}{2} \right] \tag{3.41}$$

$$t_{cog,\gamma} = t_{max} + 1.7 \tag{3.42}$$

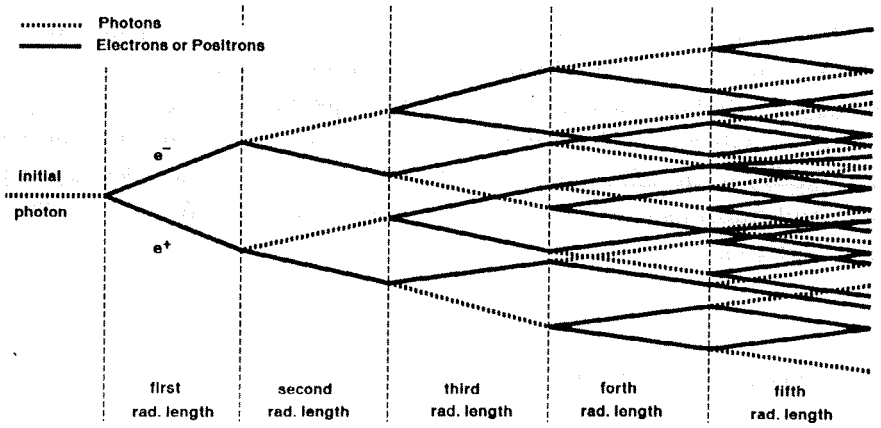

Figure 3.6: *Simple model of the electromagnetic shower development*

$$\sigma_\gamma^2 = 1.61 \ln\left(\frac{E_0}{E_c}\right) + 0.9 \tag{3.43}$$

$$t_{max,e} = 1.01\left[\ln\left(\frac{E_0}{E_c}\right) - 1\right] \tag{3.44}$$

$$t_{cog,e} = t_{max} + 1.4 \tag{3.45}$$

$$\sigma_e^2 = 1.61 \ln\left(\frac{E_0}{E_c}\right) - 0.2 \tag{3.46}$$

In order to find a better calculation of the total path length one can use a correction factor $F(z)$ which accounts for the following [20]:

- The dependence of the detectable path length on the threshold E_{thr} of the calorimeter.
- Approximation B is only valid for medium atomic numbers Z. For materials with high Z better approximations are made using the correction factor.

The mean detectable path length $< T_d >$ in a homogenous calorimeter is:

$$< T_d > [X_0] \simeq F(z)\frac{E_0}{E_c} \ , \tag{3.47}$$

with

$$F(z) \simeq e^{-z}\left[1 + z \ln\left(\frac{z}{1.53}\right)\right] \tag{3.48}$$

and

$$z = 4.58\frac{Z}{A}\frac{E_{thr}}{E_c} \ . \tag{3.49}$$

Apart from such approximations, it is, in principle, not possible to compute the whole shower development analytically. In order to find better approximations to reality one has to use the techniques of Monte Carlo simulations. In the case of the HPC the simulation of electromagnetic showers is done in HPCSIM using the program EGS (Electron Gamma Showers)

developed at SLAC[9]. EGS is generally agreed to be the most complete Monte Carlo program available for the study of electromagnetic showers. EGS considers for electrons and positrons the exact probability distributions for multiple scattering, bremsstrahlung, Møller-scattering, Bhabha-scattering and annihilation. For photons, pair production, Compton scattering and the photoelectric effect are simulated. EGS allows a detailed description of electrons, positrons and photons in matter in the energy ranges of 1.5 MeV – 100 $GeV(e^{\pm})$ and 0.1 MeV – 100 $GeV(\gamma)$.

3.7 Sampling Fluctuations

In a sampling calorimeter the detectable total path length consists almost entirely of the path elements of the charged particles in the active material. In a first approximation, we can assume that the signal is proportional to the number of crossing points N_s, of the active layers through the path of the charged particles. If we use $d[X_0]$ for the thickness of an active and a passive layer and approximation B, we get the following expression for the number of crossing points N_s:

$$N_s \simeq \frac{< T_d >}{d} \tag{3.50}$$

Use of equation 3.47 then leads to:

$$N_s \simeq F(z)\frac{E_0}{E_c d} \ . \tag{3.51}$$

We assume that the different crossing points are independent of each other and the value N_s is normally distributed. This is correct if the mean free path length of the low energetic particles is on the order of the thickness of the layers. This leads to the relative standard deviation for N_s:

$$\frac{\sigma_{N_s}}{N_s} = \frac{1}{\sqrt{N_s}} \tag{3.52}$$

A lower limit for the relative energy resolution of an electromagnetic sampling calorimeter results with equation 3.51:

$$\frac{\sigma_E}{E}(e) = 3.2\%\sqrt{\frac{E_c[MeV]}{F(z)}\frac{d[X_0]}{E_0[GeV]}} \ . \tag{3.53}$$

In the described model of approximation B [21] particle multiplication only happens one-dimensionally on the longitudinal scale of radiation lengths. In addition to that, one has to consider the effect of multiple scattering which leads to lateral expansion of the shower. The mean path of the charged particles through the active layers $< t_a > [X_0]$ is therefore increased in comparison to the thickness of the active layer $d_a[X_0]$ by a factor of $1/ < \cos\theta >$ [20]:

$$< t_a >= d_a / < \cos\theta > \tag{3.54}$$

This factor can be expressed in the following way:

$$< \cos\theta > \approx \cos\frac{E_{MS}}{\pi E_c} \ , \tag{3.55}$$

[9]SLAC : Stanford Linear Accelerator Center

where E_{MS} is used in equation 3.17 to describe the lateral shower development. With this correction the relative energy resolution is now:

$$\frac{\sigma_E}{E}(e) = 3.2\% \sqrt{\frac{E_c[MeV]}{F(z)\cos\left(\frac{E_{MS}}{\pi E_c}\right)} \frac{d[X_0]}{E_0[GeV]}} \quad . \tag{3.56}$$

This leads to the result that, because of the statistical nature of the sampling fluctuations, the relative energy resolution improves with rising energy.

$$\frac{\sigma_E}{E}(e) = \frac{const}{\sqrt{E_0[GeV]}} \tag{3.57}$$

3.8 Landau and Path-Length Fluctuations

In gaseous or very thin read-out layers, where the number of collisions, N, is small compared to the case of thick or solid absorbers, the so called *Landau* fluctuations can contribute to the sampling fluctuations. This is because of the possibility of a large energy transfer in a single collision. For heavy particles, this W_{max} is kinematically limited, while for electrons, as much as one-half of the initial energy can be transferred. In the latter case there is also the additional possibility of large energy losses due to bremsstrahlung. Although these events are rare, they add up to a long tail in the energy loss probability distribution. Thus the energy loss peak is not symmetric. The mean energy loss W_{mean} corresponds no longer to the peak of the distribution but is displaced because of the high energy tail. In contrast, the position of the peak now defines only the most probable energy loss. Theoretically, basic derivations of these distributions have been carried out by Landau, Symon and Vavilov; each of these has a different region of applicability. These regions are distinguished by the ratio:

$$\kappa = \frac{W_{mean}}{W_{max}} \quad . \tag{3.58}$$

Landau was the first to calculate the energy loss distribution for the case of very thin absorbers ($\kappa \leq 0.01$).

Path-Length fluctuations occur when the path length of an ionizing particle is much higher than the thickness of the read-out layer. In this case the $< \cos\theta >$ correction is no longer valid. The physical process behind this is the emission of a δ-electron and the curling in an external magnetic field. In this case one active layer can dominate the shower completely. Inhomogenities in the read-out structure (e.g. cracks between the sample layers) lead again to a degradation of the energy resolution. In addition, *leakage* effects (from showers which are not contained completely in the calorimeter) lead to reduced measured energies. In the construction of a calorimeter one has to keep these effects in mind to avoid inhomogenities as much as possible.

3.9 Visible Energy

The fraction of visible energy in the read-out layers compared to the total deposited energy

$$S = \frac{E_a}{E_a + E_p} \tag{3.59}$$

with

E_a : visible energy in the active layers
E_p : deposited energy in the passive layers

can be calculated using the energy loss of the so called minimal ionizing particles (mip's). A mip denotes an idealized particle which loses its energy only due to ionization. The energy loss per radiation length is independent of the energy and is equal to the minimum of the energy loss curve of a charged heavy particle (see Figure 3.1). With the help of the tabulated minimal energy loss $dE/dx|^{mip}$ for mip's, the visible energy part for layers with the thickness d can be expressed in the following way:

$$S(mip) = \frac{d_a \cdot \frac{dE}{dx}\Big|_a^{mip}}{d_a \cdot \frac{dE}{dx}\Big|_a^{mip} + d_p \cdot \frac{dE}{dx}\Big|_p^{mip}} \tag{3.60}$$

The indices a and p denote the values for the active and the passive media. Using the assumptions of approximation B that the mean path length $< t >$ of a shower corresponds nearly to the thickness of the layers

$$< t_a > \simeq d_a \ , \ < t_p > \simeq d_p \tag{3.61}$$

and that the mean energy loss of electrons due to ionization is nearly the same as for mip's

$$\left\langle \frac{dE}{dx} \right\rangle^{ion}(e) \simeq \frac{dE}{dx}\Big|^{mip} , \tag{3.62}$$

the visible energy part of an electromagnetic shower $S(e) \equiv e$ would be the same as the value for minimal ionizing particles $S(mip) \equiv mip$. The ratio e/mip would nearly be one.
However, the experimental tests on sampling calorimeters with absorption material of high atomic number show the ratio e/mip to be smaller than one. Furthermore, the ratio e/mip decreases with increasing difference ΔZ in the atomic numbers of absorption and read-out material. This experimental result can be explained due to two effects.

- The influence of the multiple scattering on the mean path length of the electrons $< t >$ has to be considered. Using previous results we find for the visible energy part of an electromagnetic shower:

$$S(e) = \frac{< t_a > \cdot \left\langle \frac{dE}{dx} \right\rangle_a^{ion}}{< t_a > \cdot \left\langle \frac{dE}{dx} \right\rangle_a^{ion} + < t_p > \cdot \left\langle \frac{dE}{dx} \right\rangle_p^{ion}} \tag{3.63}$$

with

$$< t_a >= d_a / < \cos\theta >_a \quad and \quad < t_p >= d_p / < \cos\theta >_p \ . \tag{3.64}$$

$S(e)$ is smaller than $S(mip)$ because of the relative larger mean path length $< t_p >$ in the absorption material.

- The strong charge dependence of the cross section for the atomic photoelectric effect at low energies ($h\nu < 1\ GeV$) has to be considered. By neglecting the influences of absorption edges, the cross section for photons at energies $h\nu \ll m_e c^2$ is proportional to Z^5 (see section 3.5.1). This implies that much more energy is deposited in the absorption relatively to the read-out material, which leads to a decreased value for e/mip. Furthermore, the range of photo-electrons in dense matter is less than $1mm$. Therefore, most of the photons and electrons will be absorbed in the converter material. Only photo-electrons produced at the edge of the absorption material will contribute to the signal.

Using these effects, the thickness of absorption and read-out material can be chosen in a way, so that the ratio e/mip can be manipulated inside certain ranges. Predictions about the ratio e/mip can only be done by using the techniques of Monte Carlo simulation. Therefore, the sampling structure of the calorimeter and the behaviour of low energetic shower particles need to be simulated in a detailed way.

3.10 Energy Distributions

The previous sections described some fundamental relations for the understanding of the electromagnetic shower development in a sampling calorimeter.

- The longitudinal shower development scales in radiation lengths.
- The lateral shower development scales in Molière radii.
- The shower length is proportional to the logarithm of the incident energy.
- The signal of a shower is proportional to the incident energy.
- The relative energy resolution of a sampling calorimeter is proportional to $1/\sqrt{E}$.
- The range e/mip for sampling calorimeters is lower than 1.

Due to the energy independent cross sections and the neglect of Compton scattering, the experimental data can not be quantitatively described very well in this model. Figure 3.7 shows the longitudinal shower development of 6 GeV electrons for different materials. It can be seen that the shower profiles scale only approximatively in radiation lengths. When one increases the atomic number of the calorimeter material the distributions become broader and the maxima are shifted to higher radiation lengths.

One important reason for this effect is the very different energy dependence of the total photon cross section for different materials in the MeV-region. In the transition region from pair production to Compton scattering the cross section for materials with high Z drops drastically. For example, the mean free path length in lead for a photon of a few MeV is nearly $4X_0$, whereas our model works with one radiation length.

For practical reasons, it is therefore sometimes better to use analytical formulae for the description of the shower development, which are based on measured charge distributions. This will be discussed in the following section.

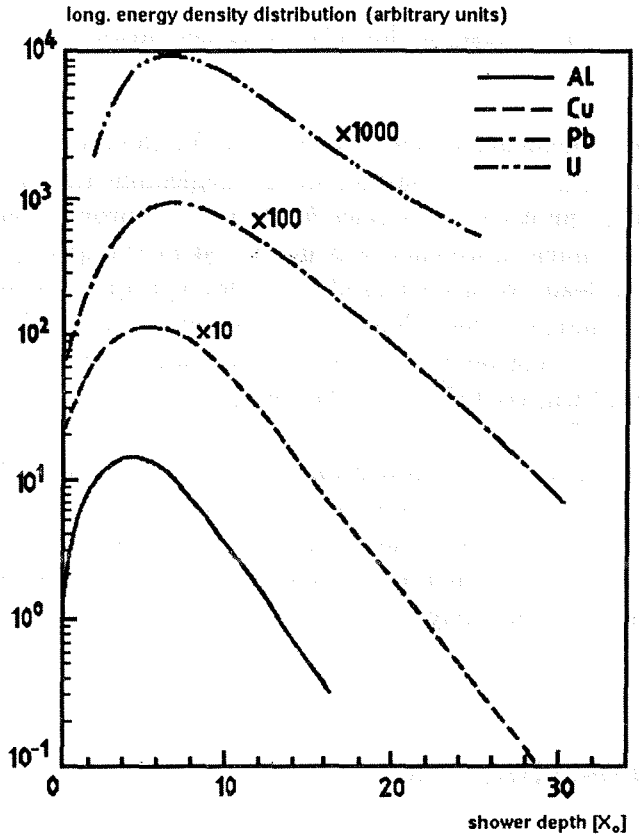

Figure 3.7: *Longitudinal shower development for 6 GeV electrons in different materials [22].*

3.11 Parametrization of Electromagnetic Showers

The total deposited energy E_{dp} of a shower yields from the integration of the deposited energy density $\rho_{dp}(\vec{r})$ over the complete volume V of the calorimeter:

$$E_{dp} = \int_V dE_{dp}(\vec{r}) \tag{3.65}$$

$$= \int_V \rho_{dp}(\vec{r})dV \tag{3.66}$$

$$= E_{inc} \quad (V \to \infty) \tag{3.67}$$

In the case of a fictitious infinite calorimeter, the total deposited energy for an electromagnetic shower is equal to the incident energy E_{inc}. The spatial distribution of the deposited energy per volume unit can be expressed by the distribution density function $f(t, r, \phi)$, which can be factorized by using the typical scales for longitudinal and lateral expansion in the t- r- and ϕ-dependent parts[10]:

$$dE_{dp}(\vec{r}) = \rho_{dp}(\vec{r})dV \tag{3.68}$$

[10]The volume element dV can be factorized in $dV = rd\phi drdt$.

$$= E_{dp} f(t, r, \phi) dt dr d\phi \quad (3.69)$$

$$= E_{dp} f_{lon}(t) dt f_{rad}(r) dr f_{azi}(\phi) d\phi \quad (3.70)$$

With this ansatz it is not necessary to have a complete and detailed description of the detector geometry. It is possible to describe the sampling structure of a calorimeter using a mean effective material distribution. In this way for example the longitudinal development of a shower can be described in calorimeter stacks with different sampling structure using only one distribution density function.

3.11.1 Longitudinal Parametrization

The mean longitudinal profile of an electromagnetic shower can be described by a Γ-distribution:

$$f_{lon}(t) = f_\Gamma(t) \equiv \frac{(\beta t)^{\alpha-1} e^{-\beta t}}{\Gamma(\alpha)} \ . \quad (3.71)$$

The parameter α describes the form of the distribution. The value t denotes the depth of the shower in units of radiation length $[X_0]$ where β is used only as a scaling factor ([23], [24], [25]).

In the calorimeter simulation, one normally does not only want to describe the mean shower profile, but to simulate the behaviour of a single shower. Fluctuating the parameters, obtained from the average profiles, does not necessarily lead to the fluctuations observed in the longitudinal shape of an individual shower. Assuming that the profiles of single showers can approximately be described by a Γ-distribution, these fluctuations can be evaluated and reproduced exactly.

The expected maximum position t_{max} of the shower development can easily be calculated by differentiating the Γ-distribution:

$$t_{max} = \frac{\alpha - 1}{\beta} \quad (3.72)$$

The expected mean value $< t >$ can be expressed as the first algebraic moment of the Γ-distribution:

$$< t > \equiv \int_0^\infty t f_\Gamma(t) dt \quad (3.73)$$

$$= \frac{\alpha}{\beta} \quad (3.74)$$

More details of the Γ-distribution and its relationship to the longitudinal shower profile in the HPC will be explained in chapter 6.

3.11.2 Lateral Parametrization

For the description of the lateral shower profile of electromagnetic showers, it can be assumed that there is only a radial and no azimuthal dependence. The lateral energy density distribution of electromagnetic showers can then be factorized into radial and azimuthal components:

$$f_{lat}(r, \phi) = f_{rad}(r) f_{azi}(\phi) \ , \quad (3.75)$$

where $f_{azi}(\phi) = 1/2\pi$. For the description of the mean radial energy density distribution a superposition of two exponential functions is often used [26]. One of them describes the confined energetic core of the shower and the other the surrounding halo.

In order to develop some fast simulation algorithms, it is sometimes easier to use a simple rational function for f_{rad} [23]:

$$f_{rad}(r) = \frac{2rR_{50}^2}{(r^2 + R_{50}^2)^2} \ , \tag{3.76}$$

where the radius r and the parameter R_{50} are in units of Molière radii. This seems adequate as long as the resolution of the calorimeter is of the order of or larger than 1 Molière radius. The radius R_{50} in equation 3.76 denotes the value of r when the distribution function reaches the value 0.50.

$$F_{rad}(r) \equiv \int_0^r f_{rad}(r')dr' \tag{3.77}$$

$$= \frac{r^2}{r^2 + R_{50}^2} \tag{3.78}$$

Figure 3.8 shows the radial energy density distribution $f_{rad}(r)$ and the distribution function $F_{rad}(r)$ as a function of radius r. In order to find a simple description of the radial energy density distribution one has to find a fitting parametrization of the expectation value and the variance of the parameter R_{50} as a function of the shower depth t and the shower energy E.

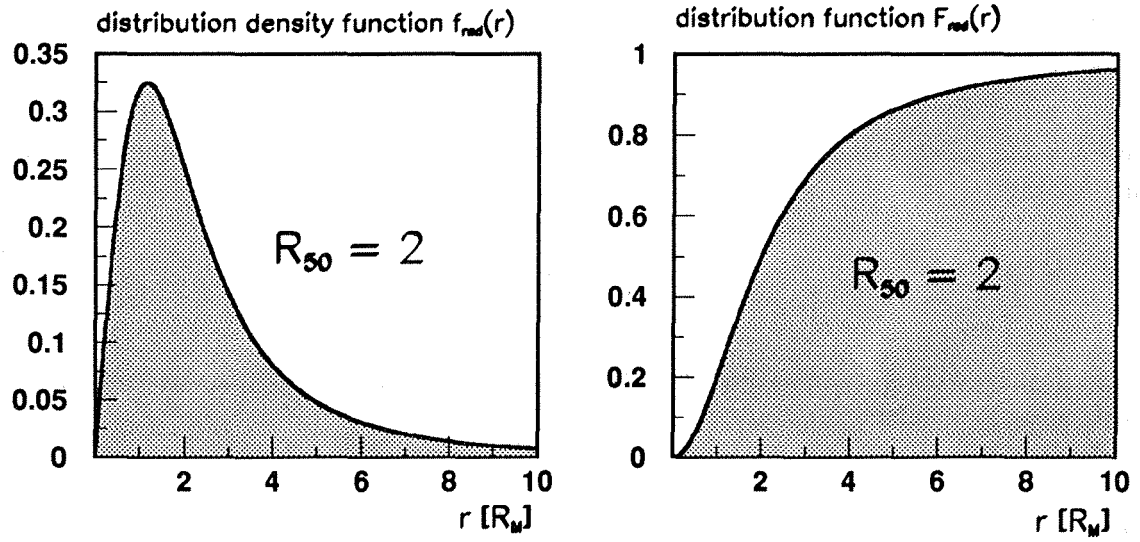

Figure 3.8: *Radial distribution density function $f_{rad}(r)$ (left) and distribution function $F_{rad}(r)$ (right) as a function of radius in units of R_M.*

3.12 Drift and Diffusion of Charges in Gases

This section describes the main effects which are important for the drift and diffusion of charges in gases ([13], [27]). This is necessary to understand the principles of charge transport in the $8mm$ drift gaps of the HPC. Especially for the studies on Krypton calibration, these results will be of major importance.

3.12.1 The Choice of the Gas Mixture

The movement of charged particles in gases is determined by the acceleration of the particles due to the electric field $\vec{E}$ and their collisions with the gas atoms. On average (time), only a mean constant drift velocity $\vec{v}_D$ is observed. For positive ions this drift velocity is a linear function of the electric field $\vec{E}$ and the pressure p of the gas:

$$v_D{}^+ = \mu^+ E p_0/p \tag{3.79}$$

The constant μ^+ is known as the *mobility* of positive ions and $p_0 = 1013mbar$. Due to their much bigger mean path length, electrons can win much more energy between two collisions. Therefore, the mobility is a factor $10^2 - 10^3$ higher than for ions. For the choice of the drift chamber gas, the following has to be demanded:

(1) small diffusion coefficient
(2) small electronegativity to avoid the absorption of electrons
(3) high gas amplification for relatively small $\vec{E}$ fields
(4) $\vec{v}_D$ nearly independent of $\vec{E}$
(5) high drift velocity $\vec{v}_D$ for fast read-out

Points (1) and (2) can be fulfilled by choosing a light inert gas such as He or Ar. Also the relative high gas amplification in the case of argon is very encouraging. Requirement (4) in this list is connected with problems. The wavelength of the electrons with an energy of a few eV is in the same region as the radius of the atomic orbitals of argon. This leads to a quantum mechanical interference effect which causes a strong variation in the collision cross section σ as a function of energy (*Ramsau* effect). This results in a strong dependence of the drift velocity on the electric field $\vec{E}$. In order to avoid this, mixtures of argon and a molecular gas (e.g. $CO_2, CH_4, Iso-C_4H_{10}$) are frequently used in drift chambers. In the case of molecular gases the electrons can initiate molecular oscillations. This can happen for CO_2 in the energy range from 0.1 to $1eV$ which corresponds to the energy range of the Ramsau minimum of argon. Using a mixture of argon and CO_2, the valley caused by the Ramsau effect can be compensated.

The gas mixture used in the HPC consists of 80% argone and 20% methane. The dependence of the drift velocity $\vec{v}_D$ on the electric field $\vec{E}$ is shown in Figure 3.9. The reason not to use the so-called *magic* gas (75% argone, 24.5% isobuthane and 0.5% freon-13B1) was the high drift velocity of $5.5cm/\mu s$, which can be obtained by using the HPC mixture with an electric field of $106V/cm$. In this way, it is possible to read out a $85cm$ long drift volume in less than $18\mu s$, well within the time between two LEP bunch crossings.

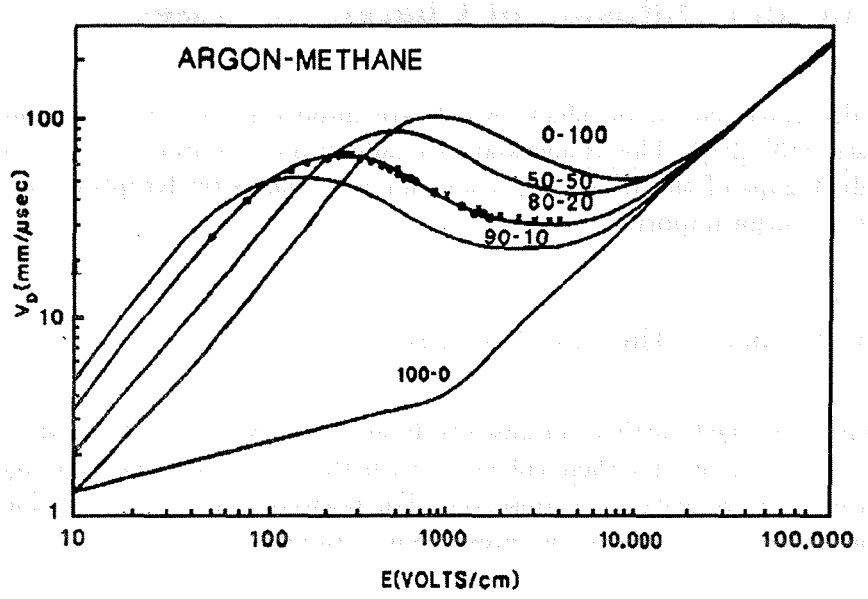

Figure 3.9: *Dependence of the drift velocity on the electric field for different argon-methane mixtures. [28].*

3.12.2 Drift of Charges in Electric and Magnetic Fields

Particles with the charge q and the velocity $\vec{v}$ feel the Coulomb force $q\vec{E}$ in the electric field $\vec{E}$ and the Lorentz force $q\vec{v} \times \vec{B}$ in the magnetic field $\vec{B}$. In the presence of electric and magnetic fields charged particles follow the curve of a helix. The movement can be divided into a translational movement with the velocity $\vec{v}_D$ and a circular movement with the frequency $\vec{\omega}_C$. This frequency is determined by the magnetic field and is called *cyclotron* frequency [13]:

$$\vec{\omega}_C = -\frac{q\vec{B}}{m} \tag{3.80}$$

For electrons the expression ω_C/B can easily be calculated from the constants e and m_e. This leads to the cyclotron frequency of $\omega_C = 211GHz$ for a magnetic field of $B = 1.2T$. If we consider the case of an electron moving in a gas volume the stochastic force $m\vec{A}(t)$ comes into play, which varies as a function of time and parametrizes the collisions with the gas atoms. This leads to the following equation of movement which is known as the *Langevin* equation:

$$m\dot{\vec{v}} = q(\vec{E} + \vec{v} \times \vec{B}) + m\vec{A}(t) \tag{3.81}$$

Since one is not interested in the detailed charge movement during single collisions, one can average this equation over time. It is known that for constant $\vec{E}$ - field the collisions with the gas atoms compensate the acceleration due to this field. This leads to a constant drift velocity $\vec{v}_D$ with $\dot{\vec{v}}_D$ equal to zero. Furthermore $< \vec{A}(t) >$ can be written as $< \vec{A}(t) >= -\vec{v}_D/\tau$ where τ is the mean time between two collisions. Equation 3.81 then leads to the following expression:

$$0 = \frac{q}{m}(\vec{E} + \vec{v}_D \times \vec{B}) - \frac{\vec{v}_D}{\tau} \tag{3.82}$$

Solving for $\vec{v}_D$ gives

$$\vec{v}_D = \frac{\mu}{1+\omega_C^2\tau^2}\left(\vec{E} + \frac{\vec{E}\times\vec{B}}{B}\omega_C\tau + \frac{(\vec{E}\cdot\vec{B})\cdot\vec{B}}{B^2}\omega_C^2\tau^2\right), \tag{3.83}$$

where $\mu = q\tau/m$ is defined as the mobility of the particle. In the presence of electric and magnetic fields the translational velocity or drift velocity $\vec{v}_D$ consists of three components: one parallel to $\vec{E}$, one parallel to $\vec{B}$ and one perpendicular to $\vec{E}$ and $\vec{B}$. For $\omega_C\tau = 0$ the drift velocity $\vec{v}_D$ follows the electric field $\vec{E}$, for $\omega_C\tau \gg 1$ $\vec{v}_D$ follows the magnetic field $\vec{B}$. In the case of the HPC for $\omega_C\tau$ we find a value of $\omega_C\tau = 6.7$ for $B = 1.2T$ [40]. Similar to the construction of a TPC the electric field is nearly parallel to the magnetic field. Let us consider $\vec{B} = (0,0,B_z)$ for the magnetic field and $\vec{E} = (E_x,0,E_z)$ for the electric field. We assume that $E_x \ll E_z$, because of a small misalignment of the system. This leads, by neglecting the second term of equation 3.83, to the following results:

$$v_x = \mu E_x \frac{1}{1+\omega_C^2\tau^2} \tag{3.84}$$

$$v_y = -\mu E_x \frac{\omega_C\tau}{1+\omega_C^2\tau^2} \tag{3.85}$$

$$v_z = \mu E_z \tag{3.86}$$

In the case of good alignment the drift velocity does not depend on the magnetic field. The z component represents the main part of the velocity. In regions near the lead wires or the brass chamber the situation can be completely different. There the electric field lines have to be perpendicular to the surface of the conducting material so that all angles between $\vec{E}$ and $\vec{B}$ are possible. Such effects will be discussed in the section about the Kr Monte Carlo.

3.12.3 Effects of Diffusion

Charges produced by ionizing effects in the drift volume quickly lose their energy in multiple collisions with the gas atoms and come to an average thermal energy. Simple kinetic theory of gases provides the average value for the thermal energy $\varepsilon_T = 3/2kT \simeq 0.04eV$ under normal conditions and the Maxwellian probability distribution of energies [13]:

$$F(\varepsilon) = C\sqrt{\varepsilon}e^{-(\varepsilon/kT)} \tag{3.87}$$

In the absence of other effects a localized charge distribution diffuses by multiple collisions following a Gaussian law:

$$\frac{dN}{N} = \frac{1}{\sqrt{4\pi Kt}}e^{-(x^2/4Kt)}dx \tag{3.88}$$

where dN/N is the fraction of charges found in the element dx at the distance x from the starting point at the time t. K is known as the diffusion coefficient. The standard deviation is given by

$$\sigma_x = \sqrt{2Kt} \quad or \quad \sigma_V = \sqrt{6Kt} \tag{3.89}$$

for linear and volume diffusion. In the presence of an electric field $\vec{E}$ the particles are accelerated between the collisions. This leads to the constant drift velocity $\vec{v}_D$. Since the mean free

path length λ depends on the electric field E the diffusion coefficient will also depend on it. The diffusion coefficient can be calculated using the following formula:

$$K(E) = \int \frac{1}{3} u\lambda(\varepsilon)F(\varepsilon)d\varepsilon \tag{3.90}$$

where $u = \sqrt{2\varepsilon/m}$ is the instantaneous velocity of electrons of energy ε. The magnetic field also has an influence on the diffusion coefficient. Since the electrons travel in circular paths with the cyclotron frequency ω_C the diffusion perpendicular to the magnetic field is reduced. For $\vec{B} = (0, 0, B_z)$ and a diffusion coefficient K for the field free gas we find the following:

$$K_z = K \tag{3.91}$$

$$K_x = K_y = \frac{K}{1 + \omega_C^2 \tau^2} \tag{3.92}$$

That means that the coefficients perpendicular to the magnetic field can be reduced drastically, if for a electron of the velocity u the radius u/ω_C of the helix is small compared to the mean free path length $\lambda = u\tau$ ($\omega_C \tau \gg 1$). In the case of the HPC ($\omega_C \tau = 6.7$) this leads to a reduction of the transverse diffusion coefficient by a factor of $1/(1 + \omega_C^2 \tau^2) \approx 1/46$. Only due to this effect it is possible to drift the charge over an distance of $85cm$ in an $8mm$ thick drift gap without loosing to much charge. Figure 3.10 shows the dependence of the transverse diffusion for the HPC gas mixture (argone-methane 80-20) on the electric field for different magnetic fields.

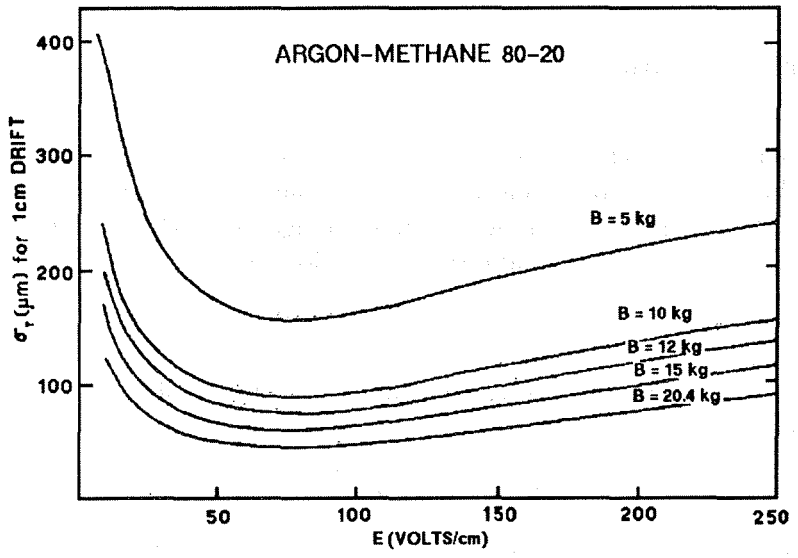

Figure 3.10: *Dependence of the transverse diffusion for the HPC gas mixture (argone-methane 80-20) on the electric field for different magnetic fields [28].*

3.12.4 Effects of Charge Loss

For the construction of a detector like the HPC, it is of major importance not to lose too much charge during the drift before reaching the chamber. Charge losses can occur because of diffusion effects and the absorption at the lead wires of the converter. As it was shown this effect is reduced drastically in the HPC because of the magnetic field of $1.2T$.

Furthermore, effects of recombination can occur where positive ions with negative ions or positive ions with electrons can recombine. The rate of recombination is proportional to the density of positive and negative ions.

For molecular gases, it is possible that electrons of a few eV can form a negative ion together with one of the gas molecules. The negative ions have a much reduced drift velocity $\vec{v}_D$ compared to the fast electrons. Therefore these ions can not contribute to the fast electron signal and are lost. The probability of this process is very small for inert gases and for N_2, H_2 or CH_4. This is also an argument for choosing an argon-methane mixture for the HPC gas. For the electronegative gases O_2, Cl_2, NH_3 and H_2O this effect is not negligible. Also notable, is that water in the gas system of the HPC reduces the transmission of charge and the drift velocity of the electrons drastically. Therefore, one has to use a very dry gas system ($< 100ppm\ H_2O$). After opening a module, one has to dry it out over several months to achieve the optimal drift velocity and charge transmission [29].

Chapter 4

Calibration of the HPC

For the calibration of the HPC a test-sample of known energy with significant energy deposition in the HPC is needed. Furthermore, we need a sample of large statistics to be able to calibrate 144 different modules. For this purpose we consider Bhabha scattering [30]:

$$e^+e^- \rightarrow e^+e^- \tag{4.1}$$

The final state electrons have a beam energy of 45.6 GeV. Due to the sizeable branching ratio of $(3.12 \pm 0.07)\%$ [31] for the process $Z^0 \rightarrow e^+e^-$ we have enough statistics to perform a module by module calibration. For the selection of the Bhabhas events the following criteria were applied:

- accept only events with two charged tracks
- division of the event in two hemispheres
  - acolinearity $< 10^\circ$
  - acoplanarity $< 2^\circ$
- one shower with more than 30 GeV in the HPC

The energy calibration requires some additional hard cuts in order to select single Bhabha showers which are fully contained in the HPC:

- accept only events with less than 5 neutral showers
- accept only showers linked to a charged track with 30 $GeV < P_{track} < 60$ GeV
- reject showers with leakage in the outer rings
- reject showers in θ-cracks
- reject showers in ϕ-cracks

After this cuts we were left with

21793 (8311) Bhabha showers for DANA92_C (DELANA_E).

This corresponds to roughly 150 (60) showers for each of the 144 modules. In this chapter the calibration of the HPC using 1992 data will be explained. Furthermore some corrections on

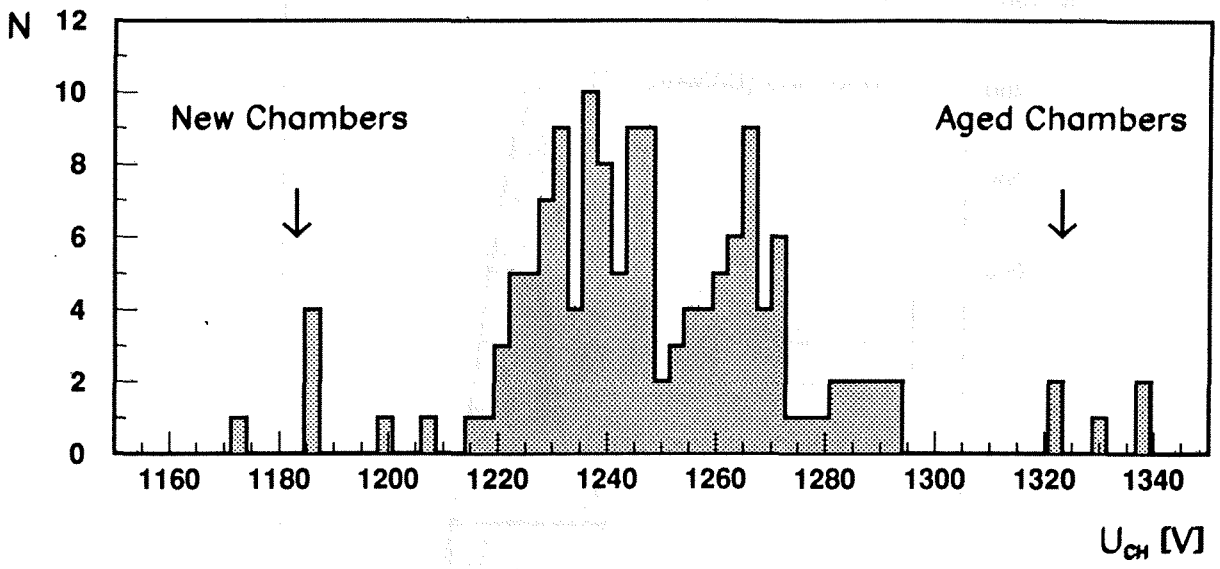

Figure 4.1: *Chamber voltages for 144 modules after Kr equalization. Younger modules run at relative low voltages while very aged modules run at higher chamber voltages.*

in chamber gain[3].

In a linear calorimeter one would expect the Bhabha peak after Kr equalization to be at 45 GeV. It is observed that the energy of the middle (outer) ring Bhabhas is decreased by 5% (10%) with respect to the inner ring Bhabhas. This effect is commonly known as *croissant effect*. The origin of this effect is not precisely determined yet. It is clear that it results from the interplay of material effects in front of the calorimeter, threshold effects inside the HPC and the lack of a proper treatment of the non-pointing geometry in the pattern recognition. A correction for this effect was done in the offline software by performing a Bhabha equalization. In addition to this procedure, two corrections were applied to get an improved energy resolution:

- ageing correction for the whole HPC evaluated from several Kr calibrations
- attenuation correction module by module

Figure 4.2 shows the Bhabha peak for all 144 modules for the processing DANA92_C. For the Bhabha resolution we find:

$$\sigma_{45} = (2.85 \pm 0.1)\ GeV \tag{4.4}$$

which corresponds to $\sigma_E/E = 6.3\%$. In the previous chapter it was shown that the energy resolution for a sampling calorimeter is proportional to $1/\sqrt{E}$. Figure 4.3 shows the resolution σ_E/E versus generated energy E for single electron Monte Carlo. The fit delivers nearly the expected behaviour:

$$\frac{\sigma_E}{E} = \frac{0.31}{E^{0.49}} \tag{4.5}$$

[3] A reduction of the chamber voltage by $68V$ corresponds to a loss in gain by a factor of two [37].

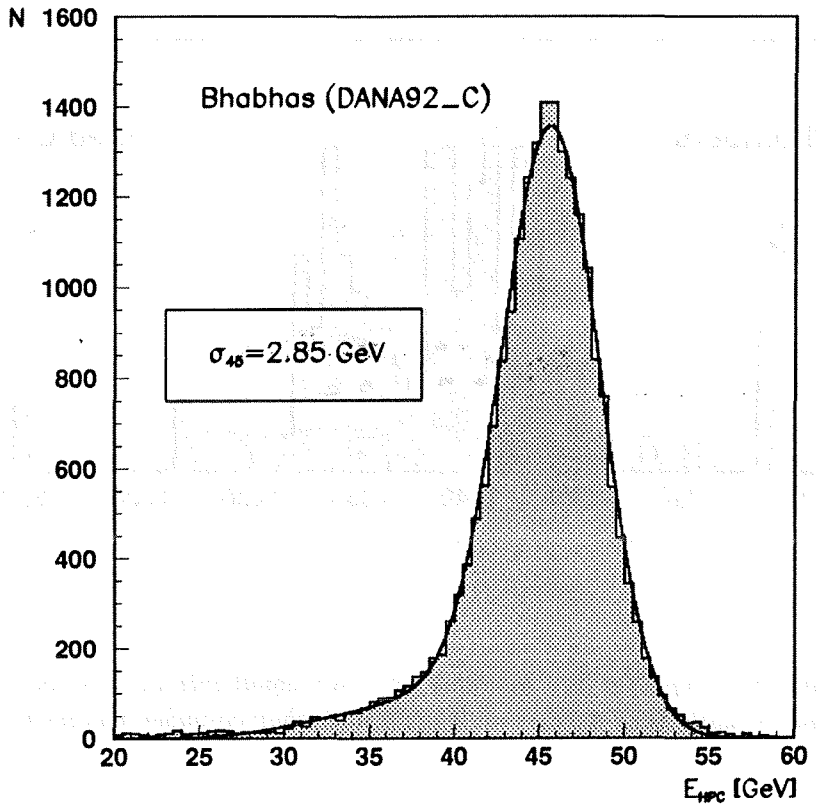

Figure 4.2: *Bhabha peak for 1992 data for all 144 modules (DANA92_C). The selection criteria for the Bhabhas are explained in section 4.*

For real data we have only two points: Comptons[4] and Bhabhas. After a fixing [32] is applied we find the following expression for the resolution[5]:

$$\frac{\sigma_E}{E} = \frac{0.44}{E^{0.60}} \oplus 0.042 \tag{4.6}$$

The constant term results from overall variations (residual uncertainties of corrections of e.g. temperature, pressure or electronic shifts) which are not simulated in the Monte Carlo.

4.2 Spatial Calibration

Due to its finely segmented read-out, the HPC has an excellent spatial resolution. The resolution in $R\phi$ is determined by the pad size of the read-out. For Bhabha showers the resolution in ϕ is [38]:

$$\Delta\phi = 3.1 mrad \tag{4.7}$$

Since the Z information is evaluated from the drift time of the charge, the resolution in

[4] For further details on Comptons see section 6.1.3.

[5] The sign $\oplus$ denotes addition in quadrature.

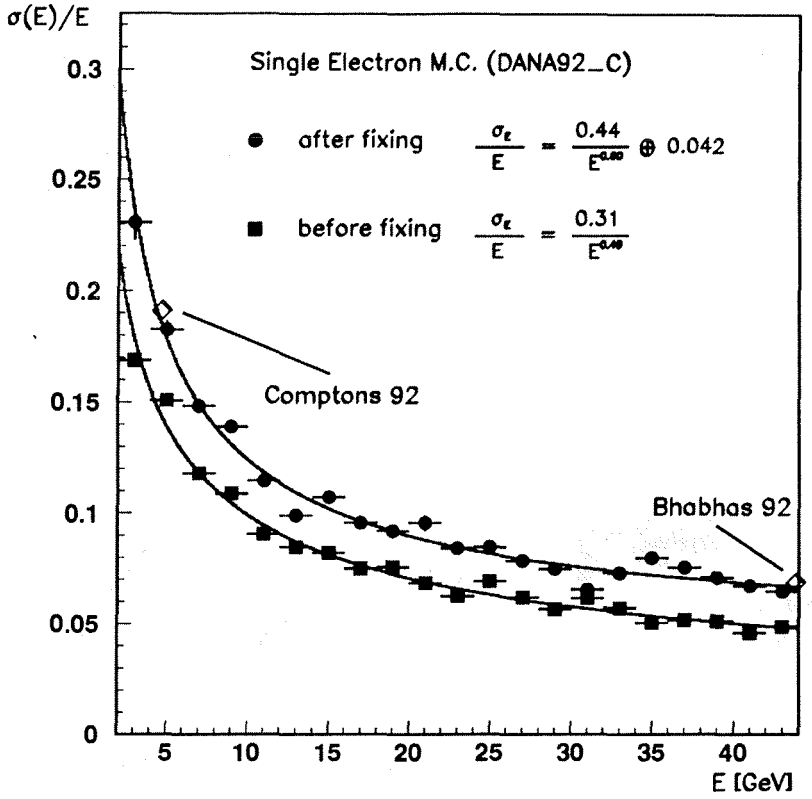

Figure 4.3: *Energy resolution as a function of energy for single electron Monte Carlo (DANA92_C) [32].*

Z depends on the single timeslot width of 3.7 *mm* and on the algorithm used in shower reconstruction. Furthermore, some hardware problems e.g. unstable drift velocities, field deformations due to short circuits in the lead wires or changing water concentrations in the modules, can lead to a drastic degradation in Z resolution. By applying corrections for all these hardware problems the Z resolution could be improved within the year 1992 by nearly one order of magnitude. For the first time the proposal values [8] could be reached.

An important tool for the Z-calibration is the so called ΔZ-plot. ΔZ denotes the difference between the Z coordinate of a HPC shower cluster and the Z coordinate of the extrapolation of the associated track to the radius of the cluster in DELPHI coordinates. By shifting ΔZ for each module to zero, a new alignment can be done. This was done for 1992 data using the described Bhabha sample. Essential for this method is the reliability on the TPC. After this procedure the following software corrections for hardware problems have been applied:

- linear correction in the ΔZ vs Z_{HPC}-plot for each module to correct Z-origin and drift-velocity
- linear correction in the ΔZ vs Z_{HPC}-plot per layer and ring to eliminate systematics
- an individual correction function for each module to consider drift-field-abnormalities caused by short circuits
- correction for run instabilities

Figure 4.4 shows the applied corrections for module 111. The first ΔZ vs Z_{HPC}-plot shows a short around $50cm$ in local module coordinates. Next to it the applied correction function is shown.

Due to the non-pointing geometry and the different material effects in different rings, it is necessary to quote separate resolution numbers for the inner, middle and outer ring:

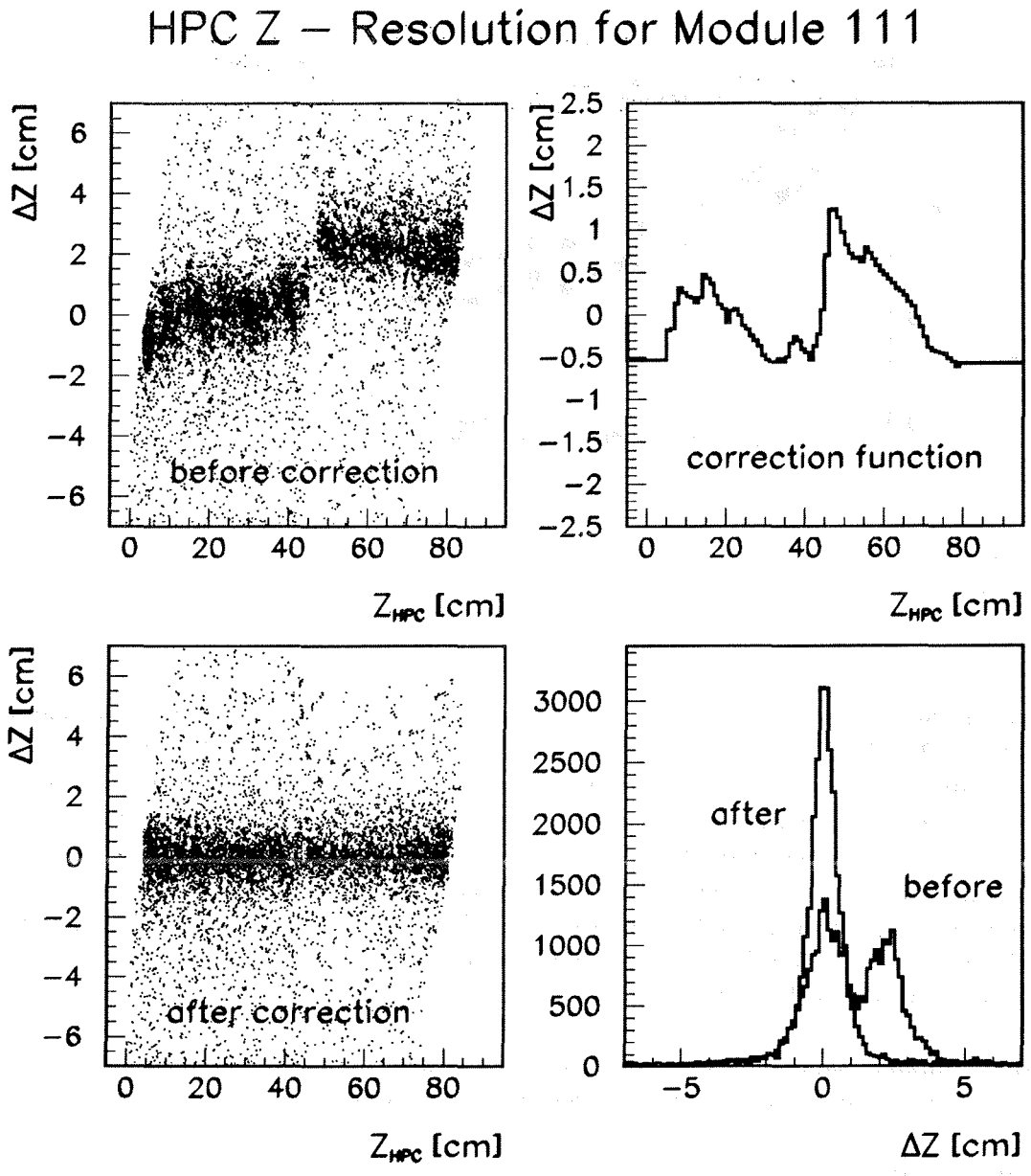

Figure 4.4: *Z corrections for module 111. The ΔZ vs Z_{HPC}-plots on the left show the situation before and after the corrections. The resolutions are compared in the last plot.*

ΔZ	$0.23cm$	$0.35cm$	$0.45cm$
	inner ring	middle ring	outer ring

Figure 4.5 shows the ΔZ information for the inner ring after the corrections. The plots for the other rings are very similar. From the Z-resolution one can easily compute the resolution in θ:

$\Delta\theta$	$1.1mrad$	$1.2mrad$	$1.1mrad$
	inner ring	middle ring	outer ring

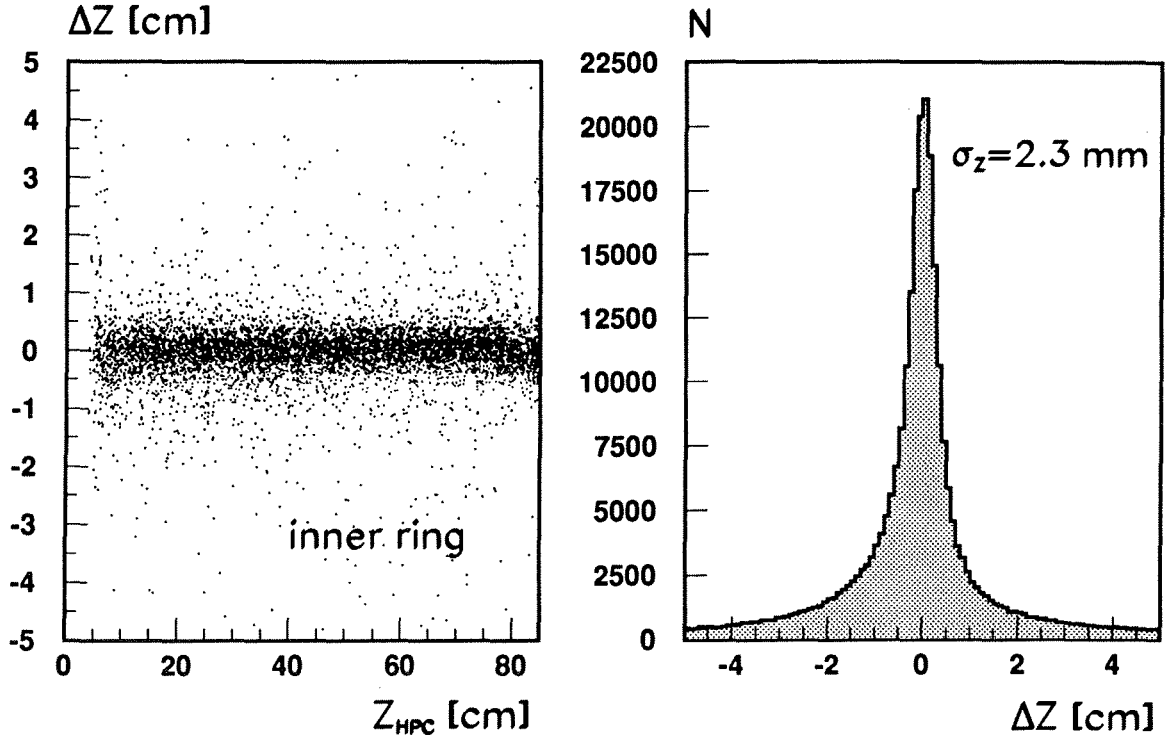

Figure 4.5: *Spatial resolution of the HPC in the inner ring. For the processing DANA92_C a resolution of $\sigma_Z = 2.3mm$ was achieved.*

Since the value $\Delta\theta$ is more important for photons than the value ΔZ, it is interesting to realize that it is nearly independent of the ring. This means that for physics use, the outer rings are not worse, in comparison to other rings in that respect.

The numbers for $\Delta\theta$ and $\Delta\phi$ refer to the angles θ, ϕ from the interaction point to the HPC. These angles are different from the measured angles ϑ and φ of the shower axis inside a HPC module. The errors on these values are independent of the ring [38]:

$$\Delta\vartheta = 14mrad \tag{4.8}$$

$$\Delta\varphi = 26mrad \tag{4.9}$$

In summary, one can say that the calibration for 1992 (DANA92_C) is well understood. The Z resolutions agree with the proposal values. The constant term for the energy resolution could be reduced drastically for 1992 data. In order to find a better agreement with the Monte Carlo an energy loss correction in shorts seems to be possible with the increased statistics of 1993.

Chapter 5

Monte Carlo Study of Brass and Graphite Chambers

5.1 Ageing Problem of the HPC

As it was mentioned in the previous chapter the HPC has ageing problems. An average module lost more than a factor of two in amplitude since start of the data taking. For several modules the signal decreased by more than a factor of four. The ageing speed evaluated from the signal loss of Bhabhas in time was measured for 1991 to be [32]

$$V_{91} = (0.24 \pm 0.03)\ \%/day\ , \tag{5.1}$$

and for 1992 to be [32]

$$V_{92} = (0.27 \pm 0.01)\ \%/day\ .\ ^{1} \tag{5.2}$$

The higher ageing speed in 1992 is fully consistent with the raising of voltages between 1991 and 1992. This means that up to now, there is no hint for a slowing down of the ageing. A rise in chamber gain by a factor of three, corresponds nearly to a factor of two increased ageing speed. In order to slow down the ageing speed, the chamber voltages were decreased in 1991 from the designed $1350V$ to $1200V$. Since the muon efficiency (2 out of 9 layers required) dropped down to nearly 30% [39] the average voltages were raised again in 1992 to $1250V$.

The measured signal loss due to ageing can be compensated by raising the chamber voltages. As it was explained in section 4.1, the response of all modules has been equalized using a Kr equalization. At the moment no measurable degradation in the performance of the HPC due to ageing has been noticed. Figure 5.1 shows the E and Z resolutions obtained from 1992 Bhabhas (DANA92_C) as a function of the equalized voltages for the modules in the inner ring[2]. As it can be seen there is no dependence of the resolutions on the ageing status. Even the very aged module 58 has reasonable resolutions. The plots for the middle and outer rings lead to the same result.

The ageing in the future can lead to problems. The voltages cannot be raised arbitrarily,

[1] One day denotes a time of 24h with high voltage switched on.

[2] Due to known converter problems the modules 59 and 89 were excluded from this plot.

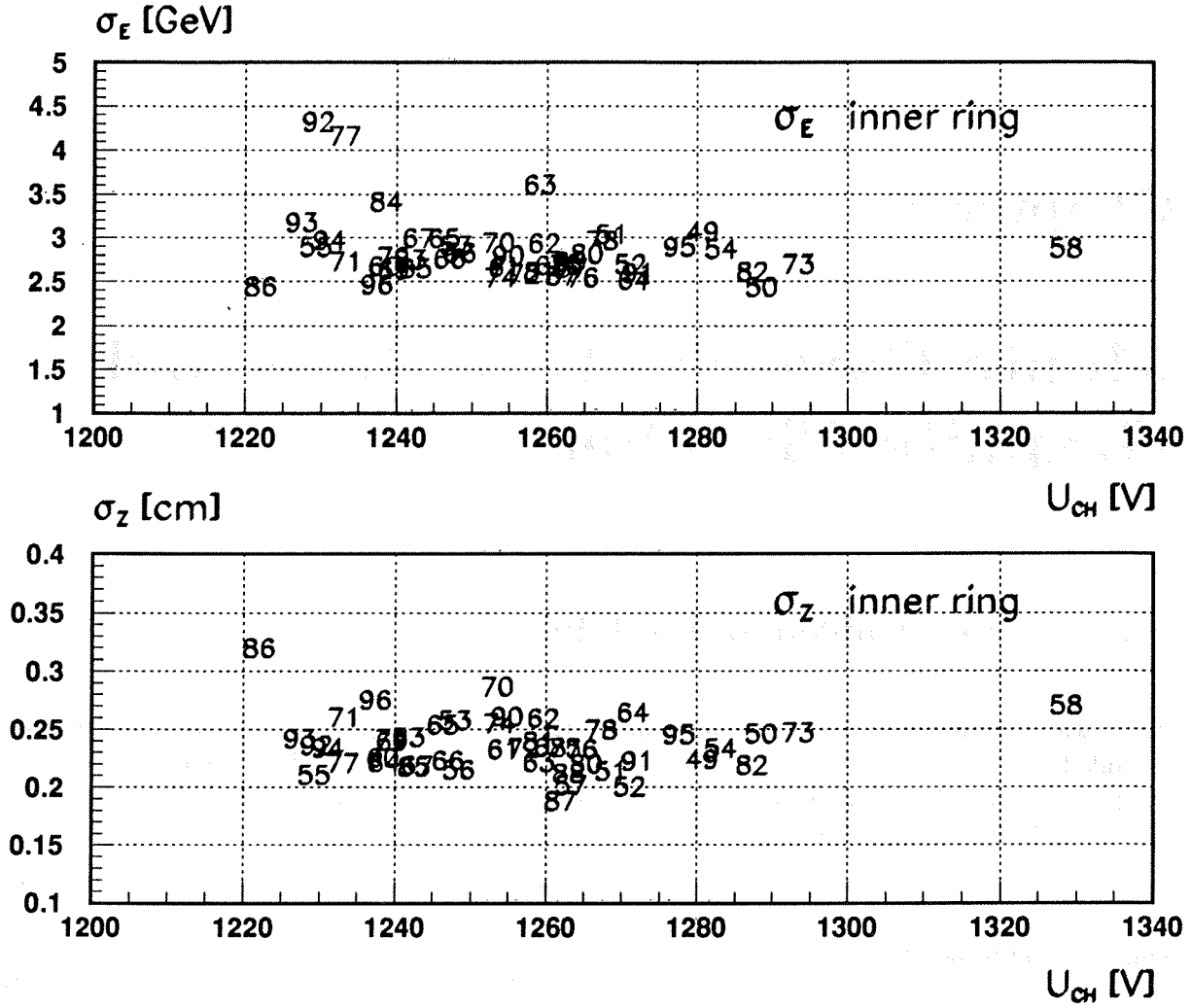

Figure 5.1: *E and Z resolutions for the modules in the inner ring as a function of equalized chamber voltages. Up till now there is no measurable degradation in the performance of the HPC. The numbers in the plot denote the module numbers.*

because above a certain limit a breakdown of the chambers will occur. At the moment a safe limit of $1500V$ is considered for the maximum possible chamber voltage. Tests in the West Area[3] are scheduled to get more information on that limit. Assuming that the limit of $1500V$ is correct, one can extrapolate that a factor of two reduced ageing speed would save the HPC until the year 2000 [37].

One proposal for the reduction of the ageing speed was the installation of graphite inserts in the read-out chambers of the HPC. Figures 5.2 and 5.3 show the geometry of these inserts. First results from ageing tests looked very encouraging. The studied chambers showed, in the first months, effectively no ageing. The idea was, that due to the grid and the deformed

[3] West Experimental Area at CERN

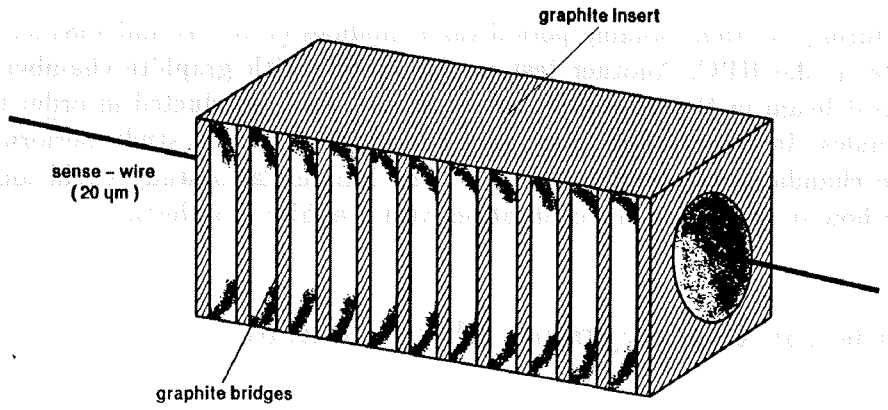

Figure 5.2: *3-dimensional geometry of a graphite insert. The sense wire of diameter* $20\mu m$ *is fixed behind the graphite bridges. The inner radius of the graphite insert is* $3.4mm$.

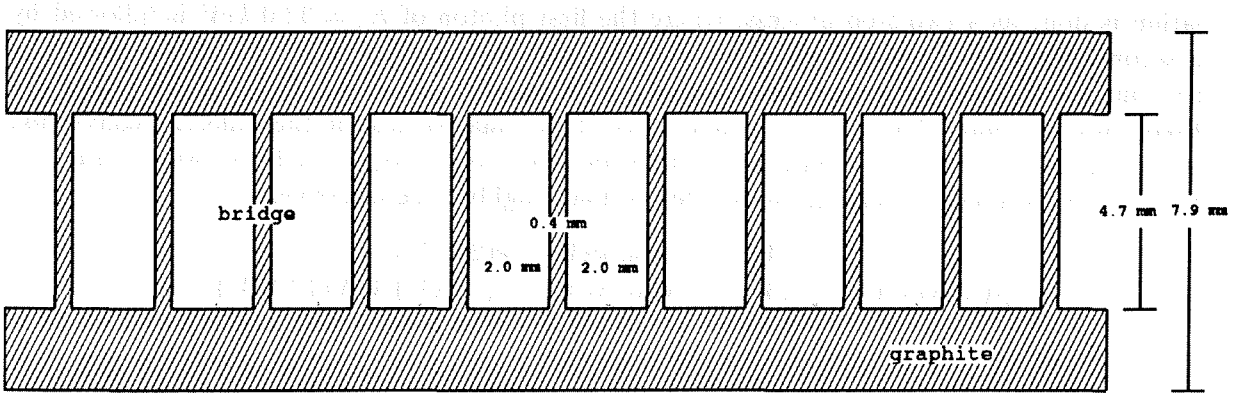

Figure 5.3: *Top view of a graphite insert. The thickness of the graphite bridges is* $400\mu m$. *The corresponding gaps have a size of* $2.0mm \times 4.7mm$.

field structure in front of the sense wire, heavy ions would be hindered in reaching the sense wire and producing an insulating layer around the wire. Furthermore, the graphite atoms transported from the gas flow were considered to change the electrical conductivity of the insulating layer in a way of reduced ageing. However, after a certain running period, the graphite chambers seem to age with the same speed as normal brass chambers. A possible explanation for this is the hypothesis, that the reduced ageing speed in the beginning is caused by a quenching gas (e. g. water) disappearing from the modules with time.

In order to install all 144 modules with graphite more than 60000 of these inserts would

be needed. During the 1992 running period three modules (113, 137 and 138) had been fitted with graphite in the HPC. Another test module (C94) with graphite chambers was available at the test beam in the West Area. Several tests were conducted in order to study the graphite modules. In this chapter the results from a Monte Carlo study performed on brass and graphite chambers will be summarized. The Monte Carlo study could answer several questions on how to perform a Kr calibration with graphite chambers.

5.2 Tools for the Krypton Monte Carlo

For the study of the Kr signal in graphite chambers a Monte Carlo program was written. The main simulation steps are:

- The Kr decays are randomly generated in the whole drift volume. Therefore the exact geometry of one drift gap is simulated which has a height of 8mm and a length of $65cm$ ($85cm$) for short (long) modules. Due to the periodic structure of the graphite insert in the direction of the wire ($400\mu m$ bridge, $2mm$ gap) the simulation needs only to be done within one such period.
- Due to the magnetic field the Kr decay ($E = 41.4\ keV$) can be considered as nearly point-like. Deviations from that are caused by the two step nature of the process. The simulation is done as a two step process, where the first photon of $E_\gamma = 32.0\ keV$ is followed by a second one with a mean delay time of $147ns$ and an energy of $E_\gamma = 9.4\ keV$. The cross sections for the interaction of the generated photons with the inner shells of the atoms are taken into account. The relative populations of the final states for the different conversion processes are listed below. Considering an mean ionization energy of $\approx 15eV$, we generate for an event with hundred percent energy deposition roughly 2500 electrons.

$$\gamma(32\ keV) \rightarrow \begin{cases} 74\% & : \quad e(30\ keV) + e(2\ keV) \\ 13\% & : \quad e(18\ keV) + e(2\ keV) + X(12\ keV) \\ 13\% & : \quad e(18\ keV) + e(10\ keV) + 2e(2\ keV) \end{cases}$$

$$\gamma(9.4\ keV) \rightarrow \begin{cases} 95\% & : \quad e(7.6\ keV) + e(1.8\ keV) \\ 5\% & : \quad X(9.4\ keV) \end{cases}$$

- For the drift towards the chamber effects of diffusion have to be considered. As it was shown in section 3.12.3 the standard deviation of the resulting distribution is proportional to the square root of the drift time. Assuming a constant drift velocity we find:

$$\sigma_t = D_t\sqrt{Z} \tag{5.3}$$

for the transverse diffusion, and

$$\sigma_l = D_l\sqrt{Z} \tag{5.4}$$

for the longitudinal diffusion. The diffusion effects are simulated using random numbers obeying a Gaussian distribution. Stepping through a drift gap in $1cm$ steps all electrons are removed which hit the boarder of the drift gap.

Experimental tests lead to a longitudinal diffusion coefficient of

$$D_l = 700\frac{\mu m}{\sqrt{cm}} \tag{5.5}$$

for the conditions of the HPC [38]. The transverse diffusion coefficient depends on the magnetic field which is different in DELPHI and in the West Area.

DELPHI	$B = 1.2T$	$D_t = 81\frac{\mu m}{\sqrt{cm}}$
West Area I	$B = 0.9T$	$D_t = 107\frac{\mu m}{\sqrt{cm}}$
West Area II	$B = 0.7T$	$D_t = 135\frac{\mu m}{\sqrt{cm}}$

- Detailed studies of the geometry of the lead converter and of the interplay of the electric and the magnetic field near to the lead wire reveal that the *effective* height of a drift gap is smaller than $8mm$. Due to the complicated field configuration near to the lead wire, charges are absorbed if they come close enough to the lead. This leads to a reduction of the effective height of the drift gap to roughly $7.4mm$ [40].
- The geometrical structure of the graphite insert leads to an additional screening of the generated electrons. Due to an attractive effect, where charges inside the geometrical shadow of the grid are attracted to the chamber, the effective geometry will be different from the pure geometrical model. This effect can be called *sucking* effect. Figure 5.4 shows the equipotentials

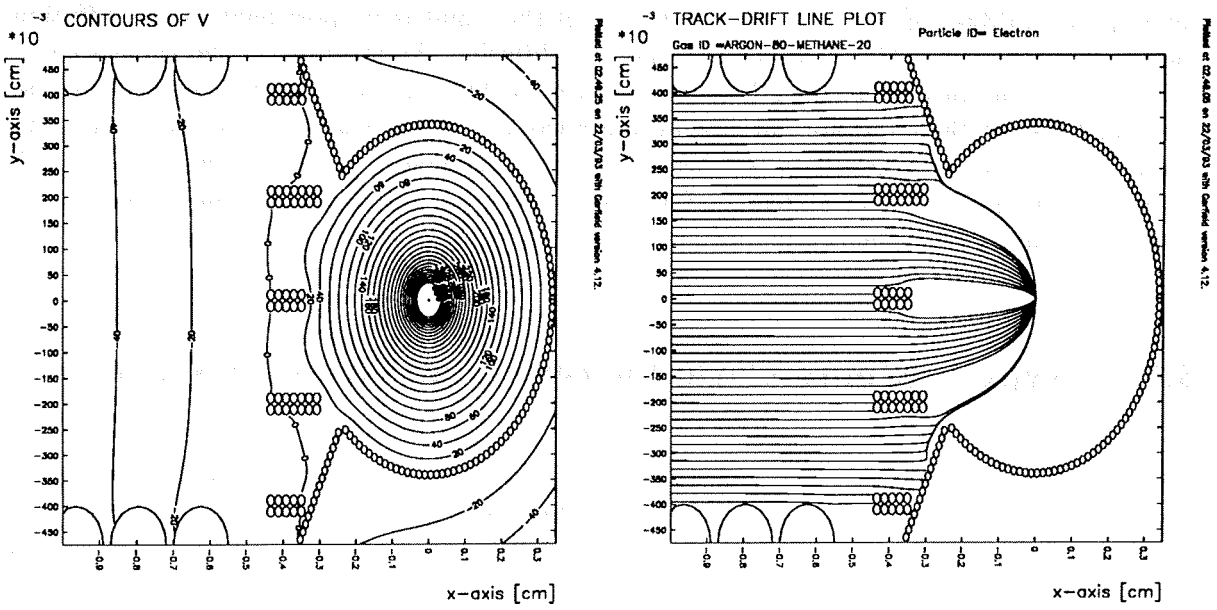

Figure 5.4: *Equipotentials and drift lines for electrons in a pseudo-graphite structure calculated by the drift chamber simulation program* Garfield. *The sense wire was set to* $1250V$ *and the field gradient between two lead wires was* $18V$. *A magnetic field of* $1.2T$ *was used.*

and the drift lines for a pseudo-graphite structure calculated by the drift chamber simulation program *Garfield* [41] [4]. Since *Garfield* is only able to handle 2-dimensional structures the full geometry of a graphite insert cannot be simulated. Using the pseudo-geometry shown

[4] *Garfield* uses a thin wire approximation to calculate electric and magnetic field configurations in two dimensions. Geometric objects have to be formed using thin wires.

in Figure 5.4, the appearance of sucking effects is revealed. Since this simulation is only 2-dimensional quantitative predictions cannot be deduced from this model. Therefore different effective geometries were tested to achieve best agreement between measured data and Monte Carlo prediction.

The simulation program can evaluate the response function of the system by counting the number of detected electrons and dividing through the number of generated electrons. Weighting the response function with the generated charged energy and folding with 5% resolution of the chamber produces a prediction for the expected Kr-peak. In order to keep the model simple and avoid biases, the efficiency of the chamber has been simulated as a step function at 6 keV. That means that a comparison between data and Monte Carlo can only be valid at higher energies of the spectrum.

Essential for the shape of the Kr-peak is the *transparency* of the grid. This transparency depends on the magnetic fields, the electric fields and on the geometrical structure of the grid. An effective bridge width of $250 - 300\mu m$ compared to the $400\mu m$ real width seems to be a good description for the real data. Even more important is the dependence on the transverse diffusion coefficient. It is interesting to realize that an electron cloud produced from a Kr decay after the drift with $D_t = 81\mu m/\sqrt{cm}$ has nearly the same dimensions as the distance between two bridges of the grid. Since the size of the cloud is proportional to the diffusion coefficient, this gives a hint that by changing the diffusion the response of the system could be changed dramatically. The gap height of $4.7mm$ has little influence on the results, because it is much larger than the normal size of a Kr cloud. Monte Carlo studies with different effective heights could prove the effect to be negligible. Therefore in this presentation, we will always use the pure geometric height of $4.7mm$. This corresponds to the elimination of one parameter from a problem in a multidimensional space.

5.3 Krypton Monte Carlo for Brass and Graphite Chambers

The first Kr calibration in the new graphite chambers revealed a much worse resolution compared to the well known brass chambers. The brass chambers produce two easily identified and well separated Kr peaks at 32 keV and 41.4 keV. The Kr-peaks in graphite chambers look much different. The 41.4 keV peak and the escape peak[5] are smeared into one broad distribution. Figure 5.5 compares the Monte Carlo results of the Kr-peaks in brass and in graphite chambers (module length L=65cm). For brass chambers losses of charge are only due to diffusion effects near the lead converter. For graphite chambers an additional screening effect, because of the grid, comes into play. Since the average size of the electron cloud is of the same order as the bridge distance, the response of one event depends very heavily on the generated position in x and y. Figure 5.6 illustrates this effect by comparing three simulated Kr events with the bridge geometry. The electrons have been drifted over $40cm$. The diffusion coefficient was $81\mu m/\sqrt{cm}$. One has to keep in mind that, in the complete simulation, one has a sum of different cloud sizes because of different Z-positions. This situation produces a response function with a broad distribution between zero and one while for brass chambers a

[5]The escape peak denotes the 32 keV peak. The 9.4 keV photon is not converted into charged particles.

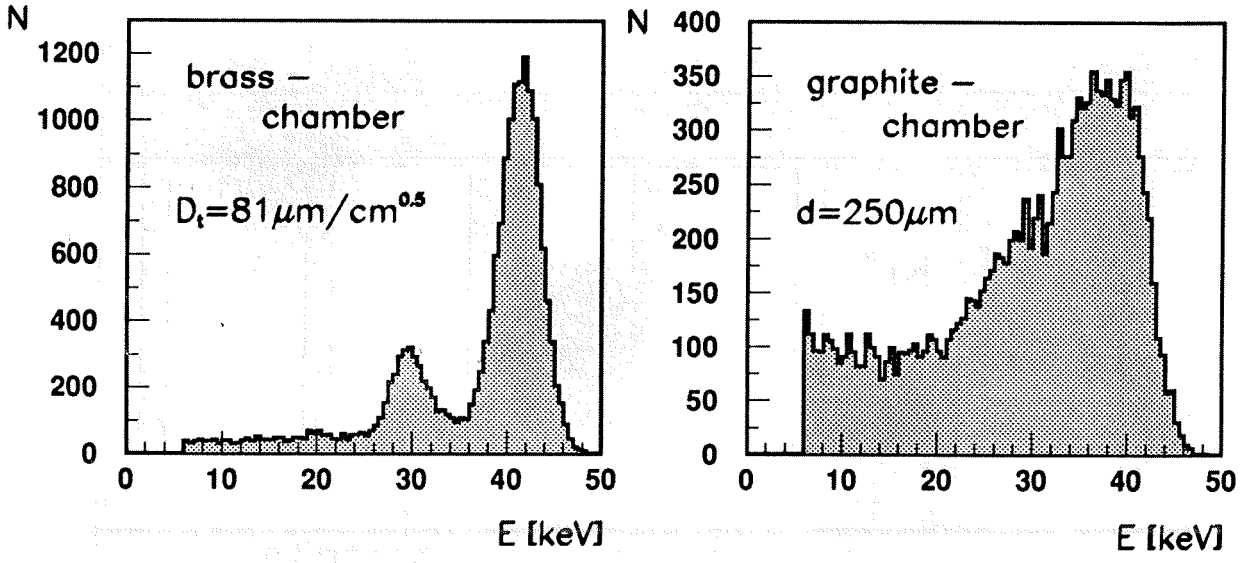

Figure 5.5: *Kr-Monte Carlo in brass and graphite chambers for DELPHI conditions (D_t = 81$\mu m/\sqrt{cm}$). The brass chamber is simulated without any screening in front of the sense wire. For the graphite chamber an effective bridge width of* 250μm *is used.*

peak at one is dominating completely. This results in a drastically reduced resolution for the Kr-peak in graphite compared to the peak in brass chambers.
The degradation in energy resolution is only important for nearly point-like sources of charge as for example the Kr decay. The situation is completely different for a shower. The charge is distributed over several centimeters in the drift gap so that the measured average is almost stable. Moreover, a better picture of the charge deposition in a shower is expected, because the critical regions for charge losses next to the lead wires are cut away by the grid geometry.

5.4 Krypton Simulation for Different Magnetic Fields

As it was described in section 5.2, several test modules were fitted with graphite inserts. For the modules in the HPC the magnetic field was 1.2T, while C94 was running with 0.9T (0.7T). It was a difficult problem to understand why the module C94 with a larger transverse diffusion coefficient seems to have a better resolution than the modules in the HPC. Increased diffusion normally leads to increased charge loss and a worse resolution.

The Kr-Monte Carlo could deliver the explanation for this behaviour. For this purpose, several Monte Carlo samples (each consisting of 20000 Kr events) were generated with different transverse diffusion coefficients. This was done for short modules (L = 65cm) and an effective bridge width of 250μm.

Figure 5.7 shows the different Kr-peaks for four different diffusion coefficients. The first plot shows the Kr-peak for a diffusion coefficient of D_t = 40$\mu m/\sqrt{cm}$ (B = 2.4T) which is much too optimistic. The 41.4 keV-peak is nicely separated from the 32 keV escape peak.

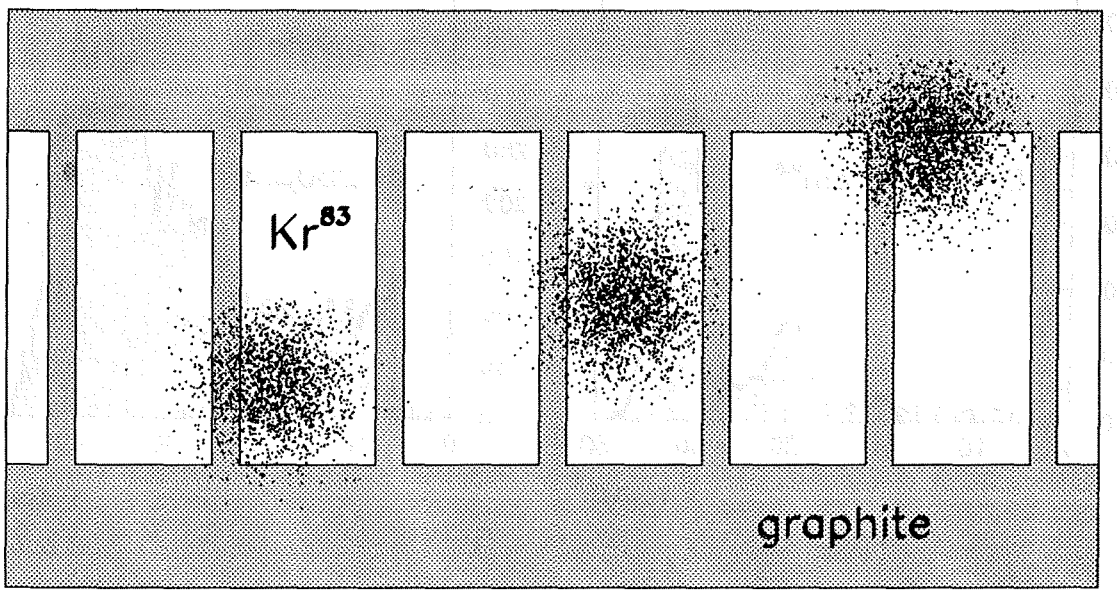

Figure 5.6: *Visualization of three Kr events, generated at different X Y positions, with the bridge geometry of a graphite grid. The generated Z-position was 40cm. The diffusion coefficient was $81\mu m/\sqrt{cm}$.*

Increasing the diffusion to $D_t = 81\mu m/\sqrt{cm}$ ($B = 1.2T$) leads to the conditions in the HPC. A broadly smeared peak is visible. By increasing the diffusion again to $D_t = 107\mu m/\sqrt{cm}$ or $D_t = 135\mu m/\sqrt{cm}$ corresponding to the conditions of the module C94 ($B = 0.9T$, $B = 0.7T$), the resolution is improved again. The width of the peaks is reduced and a separation between main and escape peak seems to be visible.

Things become clearer if one looks at the response of the system. Figure 5.8 shows the response functions for the four different cases. In the first plot, the peak at one is dominating the situation completely. By increasing the diffusion to $D_t = 81\mu m/\sqrt{cm}$ the peak at one drops down and a broad distribution appears. By increasing the diffusion again to $D_t = 135\mu m/\sqrt{cm}$ a dramatic change is visible. A peak at 87% arises. This peak affects a major part of all events. This peak is responsible for the improved resolution by increased diffusion. Since this peak is centered at 0.87 and not at 1.00 the corresponding Kr-peak is not the same as the peak in brass chambers. The peak is shifted to lower energies as it can be seen in Figure 5.7.

The reason for this peak in the response function is easy to understand. As was shown in Figure 5.6, the size of an average electron cloud from a Kr decay with $D_t = 81\mu m/\sqrt{cm}$ is in the order of the typical dimensions of the grid. Increasing the size of the cloud leads on average to increased charge losses at the grid. But the important point now, is that the response is more stable. It is connected to the creation of a peak at 87%. Further improvement in resolution by increasing the diffusion is limited by the losses in the converter. In order to get

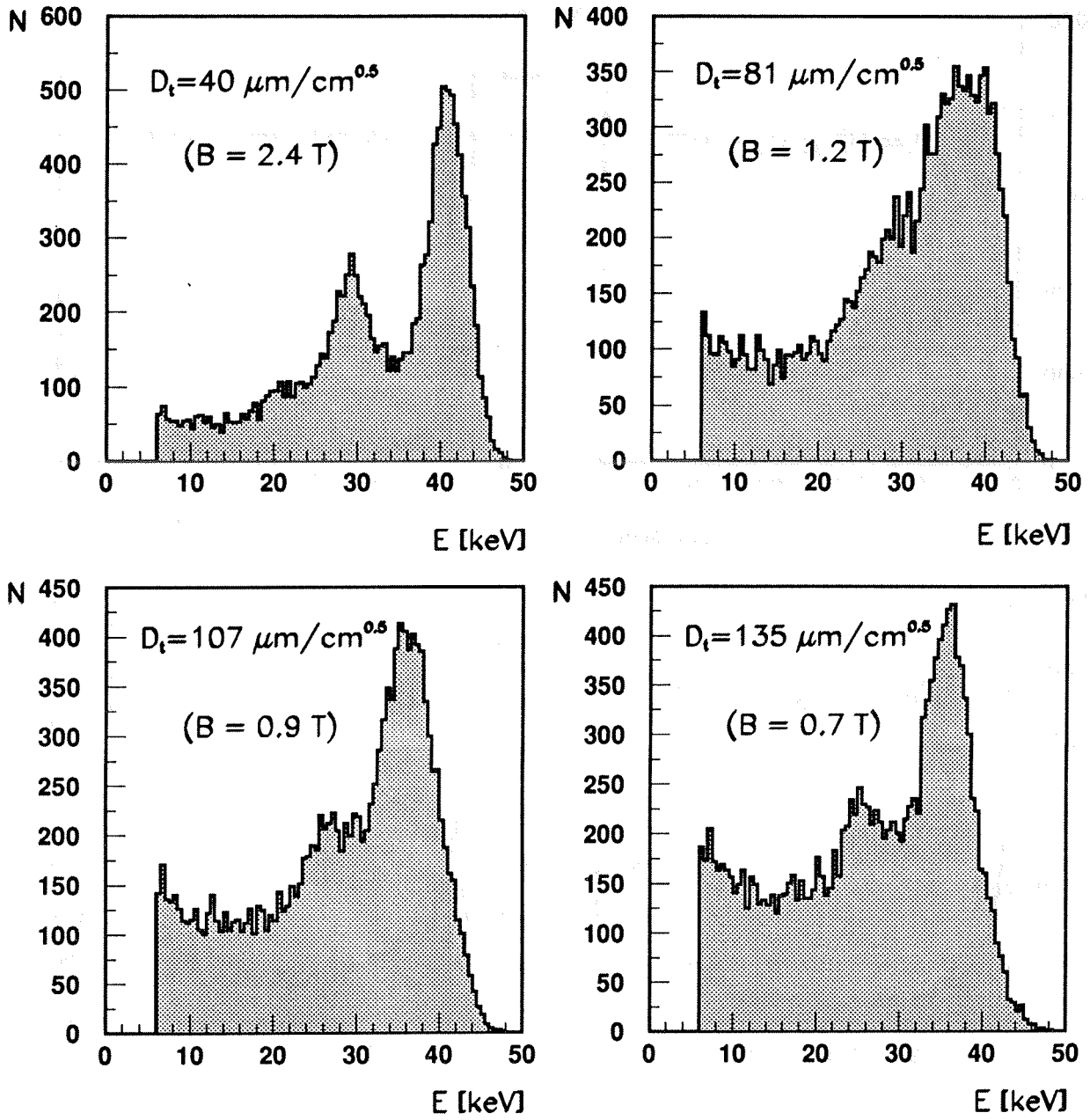

Figure 5.7: *Kr-peaks for four different transverse diffusion coefficients. The Monte Carlo was generated with an effective bridge width of* $250\mu m$ *and a module length of* $65cm$.

a better estimate of the systematics we consider Figure 5.9. It shows the dependence of the response function on the Z-coordinate of the generated event for the two diffusion coefficients $D_t = 81\mu m/\sqrt{cm}$ and $D_t = 135\mu m/\sqrt{cm}$. Both plots show two bands which come closer to each other at higher Z-values. The lower band comes from events produced in front of a bridge while the upper band comes from events produced in front of a gap. It is clearly visible that the projection on the ordinate leads to a much broader distribution in the case of

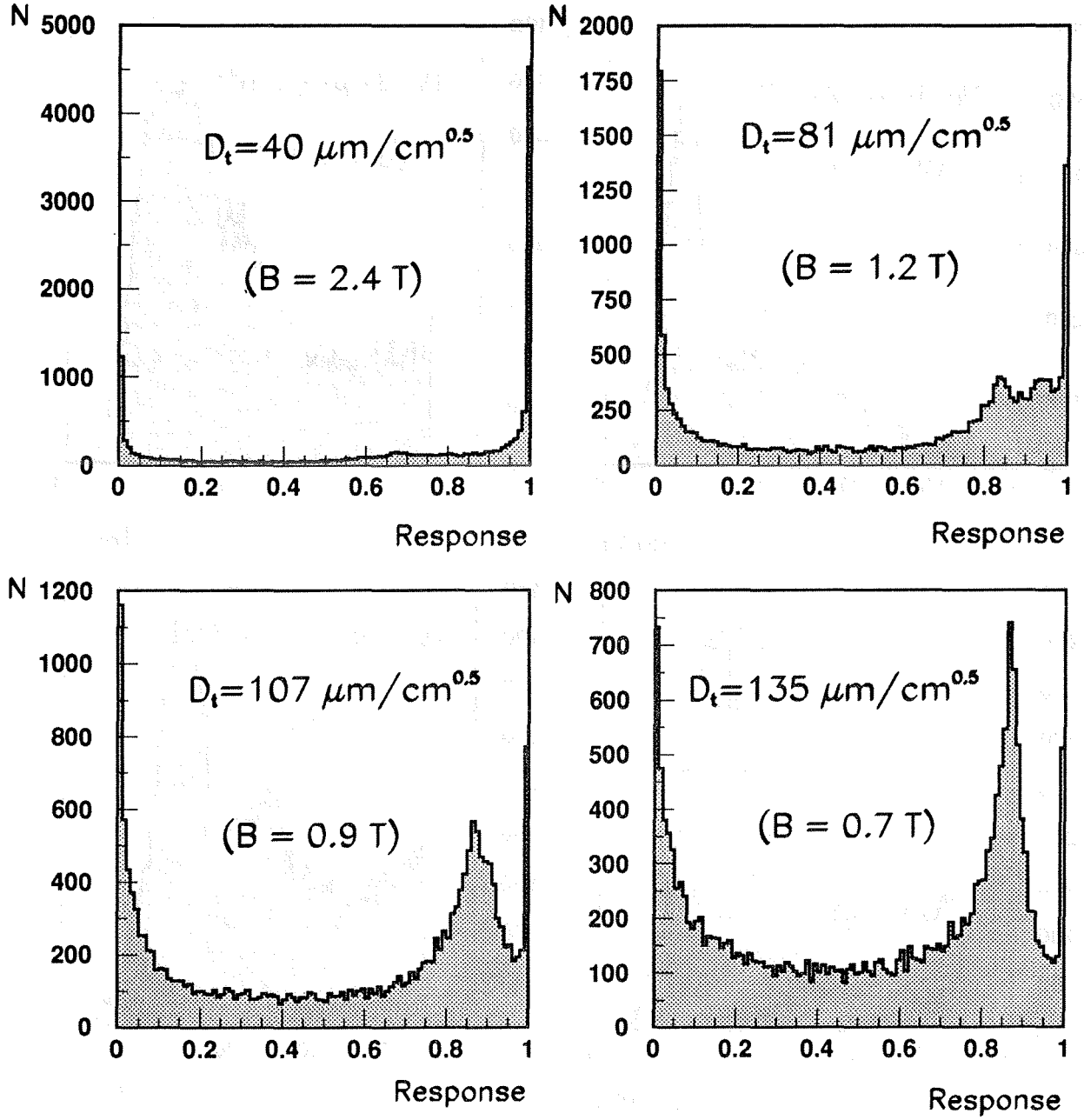

Figure 5.8: *Response functions for four different diffusion coefficients. The Monte Carlo is generated with an effective bridge width of* $250\mu m$ *and a module length of* $65cm$.

$D_t = 81\mu m/\sqrt{cm}$ than in the case of $D_t = 135\mu m/\sqrt{cm}$.

To get an idea of how the resolutions change as a function of diffusion coefficient we generated ten Monte Carlo samples with different magnetic fields. In order to judge the quality of a Kr-peak the histograms were fitted with two Gaussian functions and a quadratic background. Figure 5.10 shows the definition of a quality factor Q and the main peak position E_{Main}. The position E_{Main} is normally used to equalize the modules after a Kr calibration.

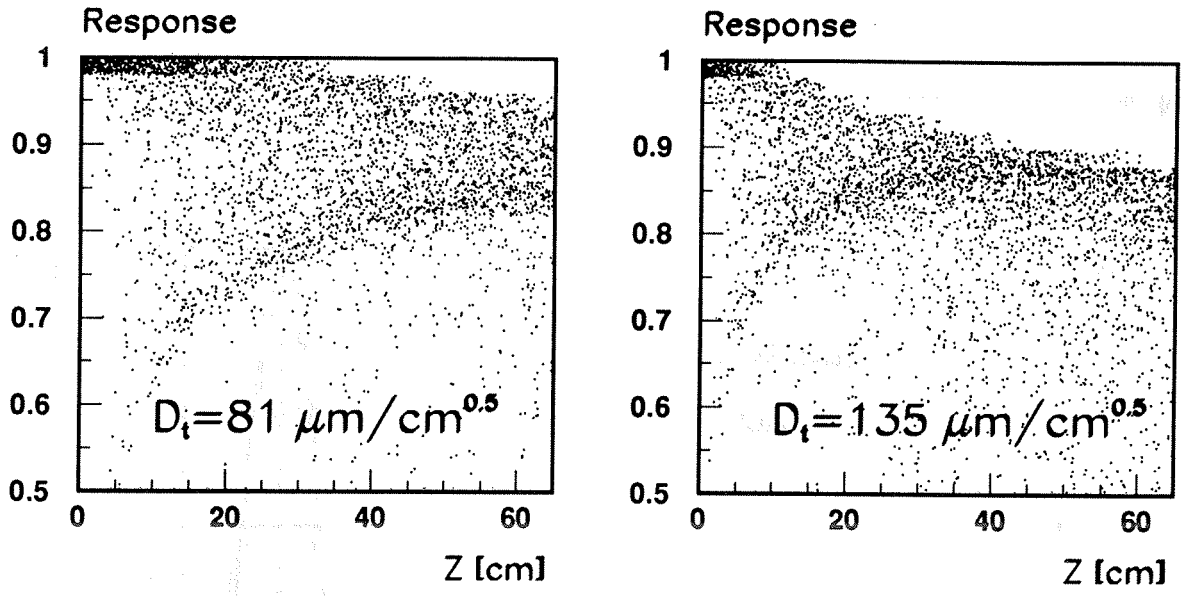

Figure 5.9: *Dependence of the response function on the Z-coordinate of the event generation for two different diffusion coefficients.*

Figure 5.11 shows Q and E_{Main} as a function of the diffusion coefficient. The errors on these points are calculated from the 8 parameter fit using error propagation. It is visible that the quality of the Kr-peak drops down to a minimum at $D_t = 70\mu m/\sqrt{cm}$. Q then increases as we approach the conditions of the module C94 in the West Area ($B = 0.9T$, $B = 0.7T$). At very large values of the diffusion coefficients the quality Q drops down, because the losses at the converter begin to dominate. Unfortunately this curve has its local minimum next to the conditions of the HPC ($B = 1.2T$) which makes a calibration even harder. The position of the main peak E_{Main} is shifted smoothly downward. For $B = 0.7T$ it drops to roughly 35 keV.

5.5 Comparison between Data and Monte Carlo

This section describes the comparison between data and Monte Carlo for modules 137 and 138 in the HPC and for the test module C94 in the West Area. These modules are all short modules (L=65cm). The measured real data were all taken at a chamber voltage of 1250V. Due to the different magnetic fields different effective geometries have to be applied in the Monte Carlo. Figure 5.12 shows the change in the predicted Kr-peaks for various effective bridge widths. A movement of the peak position is visible together with a change in resolution.

Figure 5.13 shows the comparison between data and Monte Carlo[6]. The data have been normalized to the same number of events as the Monte Carlo. For $B = 1.2T$ an effective bridge width of 300μm seems to describe the data best, while for $B = 0.9T$ and $B = 0.7T$ an

[6]The measured data were provided by T. Tabarelli [42].

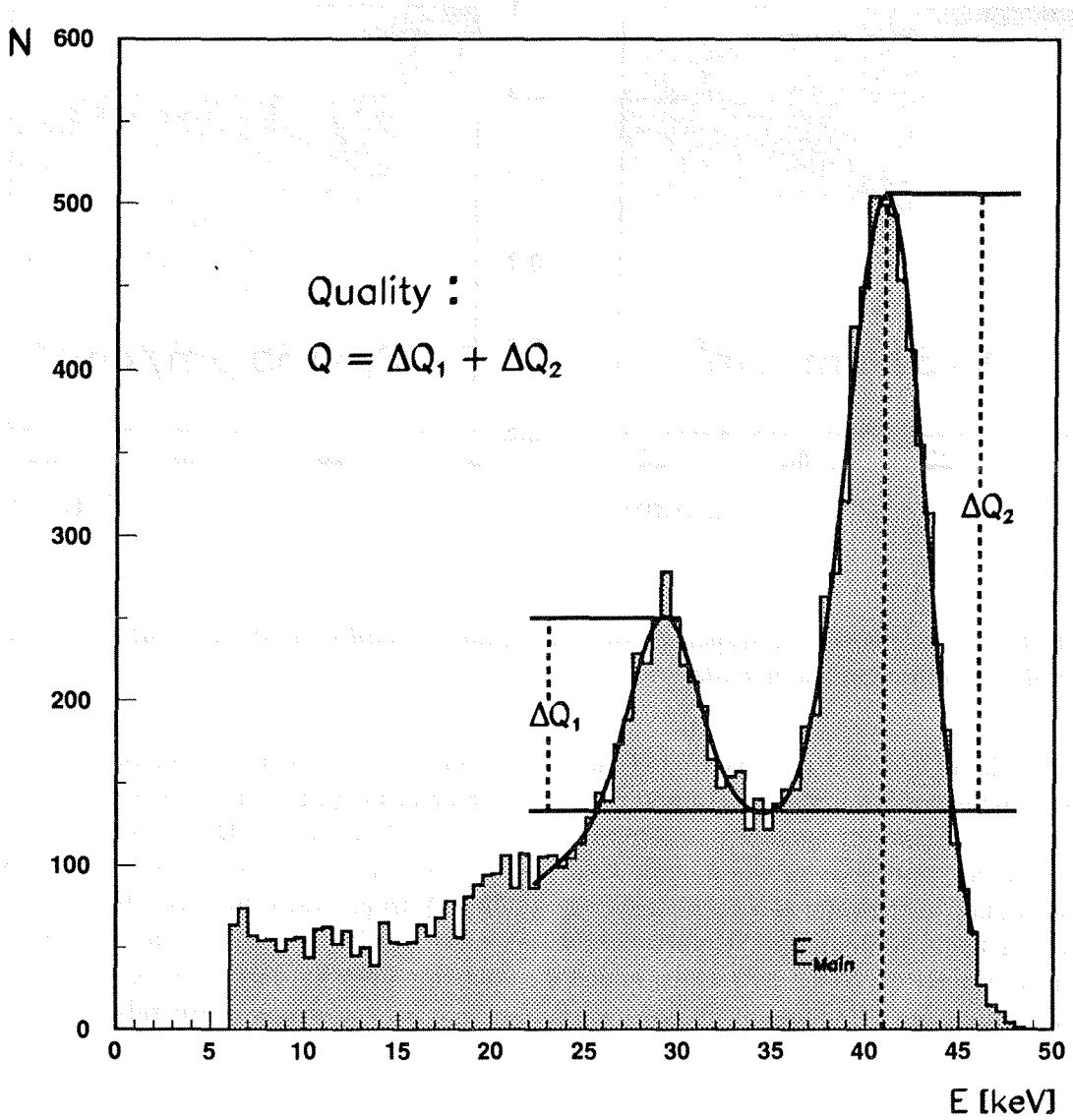

Figure 5.10: *Definition of a quality factor Q and the main peak position E_{Main} from a fit with two Gaussian functions and a quadratic background.*

effective bridge width of $250\mu m$ fits best. There appears to be very good agreement between data and Monte Carlo. The increased resolution with decreasing magnetic field seems to confirm our understanding of the behaviour of these modules. Even the drop between the two peaks at $B = 0.9T$ and at $B = 0.7T$ is in agreement with the data.

If one considers again Figure 5.9, it is visible that Kr events generated at large Z-positions

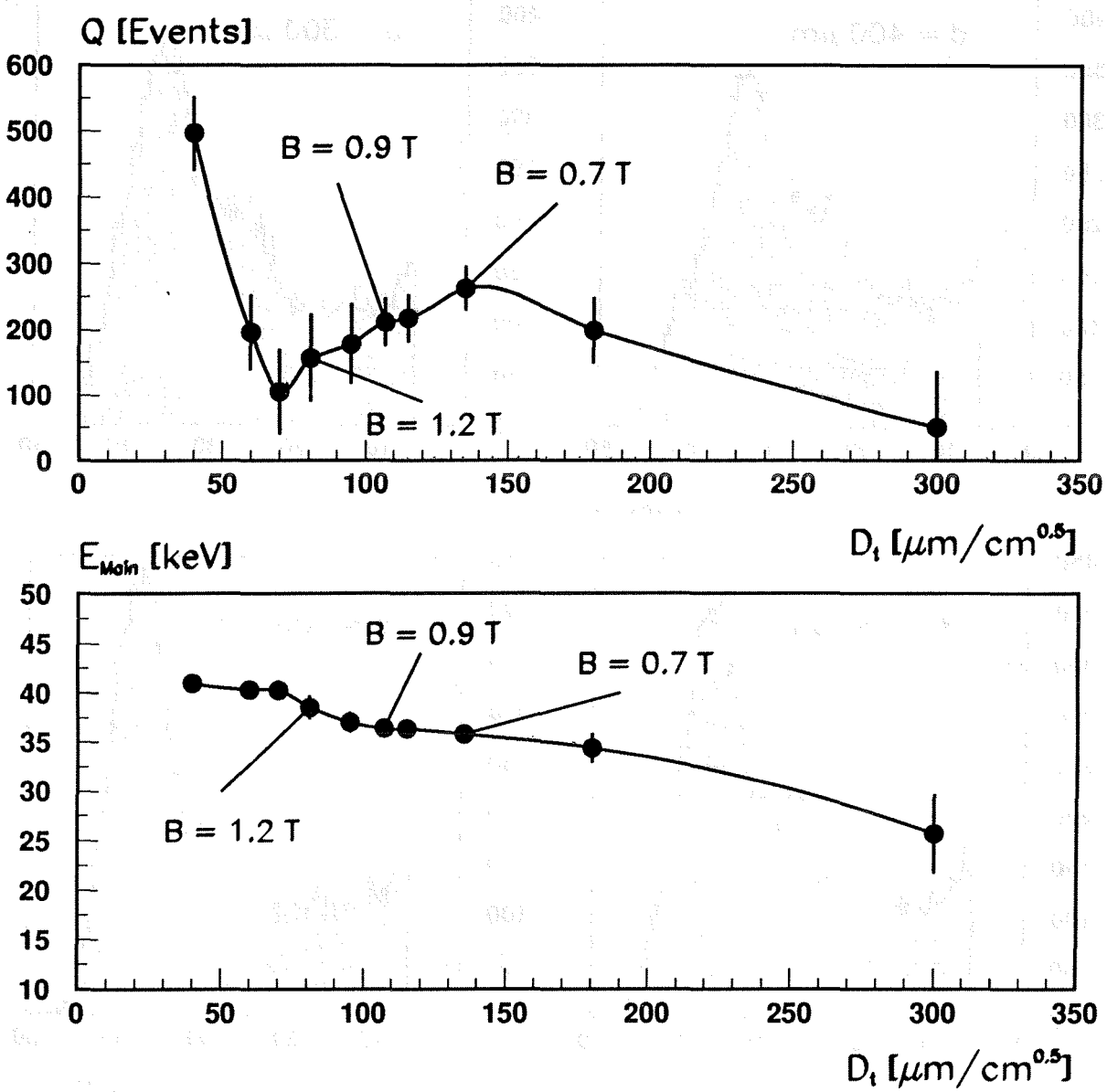

Figure 5.11: *Quality factor Q and main peak position E_{Main} as a function of the diffusion coefficient.*

produce a better separation between main and escape peak than events with smaller Z-coordinates. This implies that long graphite modules should have a better resolution in the Kr-peak than short modules. Unfortunately the long module 113 in the HPC had converter problems in the 1992 running period, so that a comparison between data and Monte Carlo was impossible. Module 113 had some strange field configurations in the converter directly in front of the chamber. From studies on ΔZ-plots it is known that the drift velocity dropped

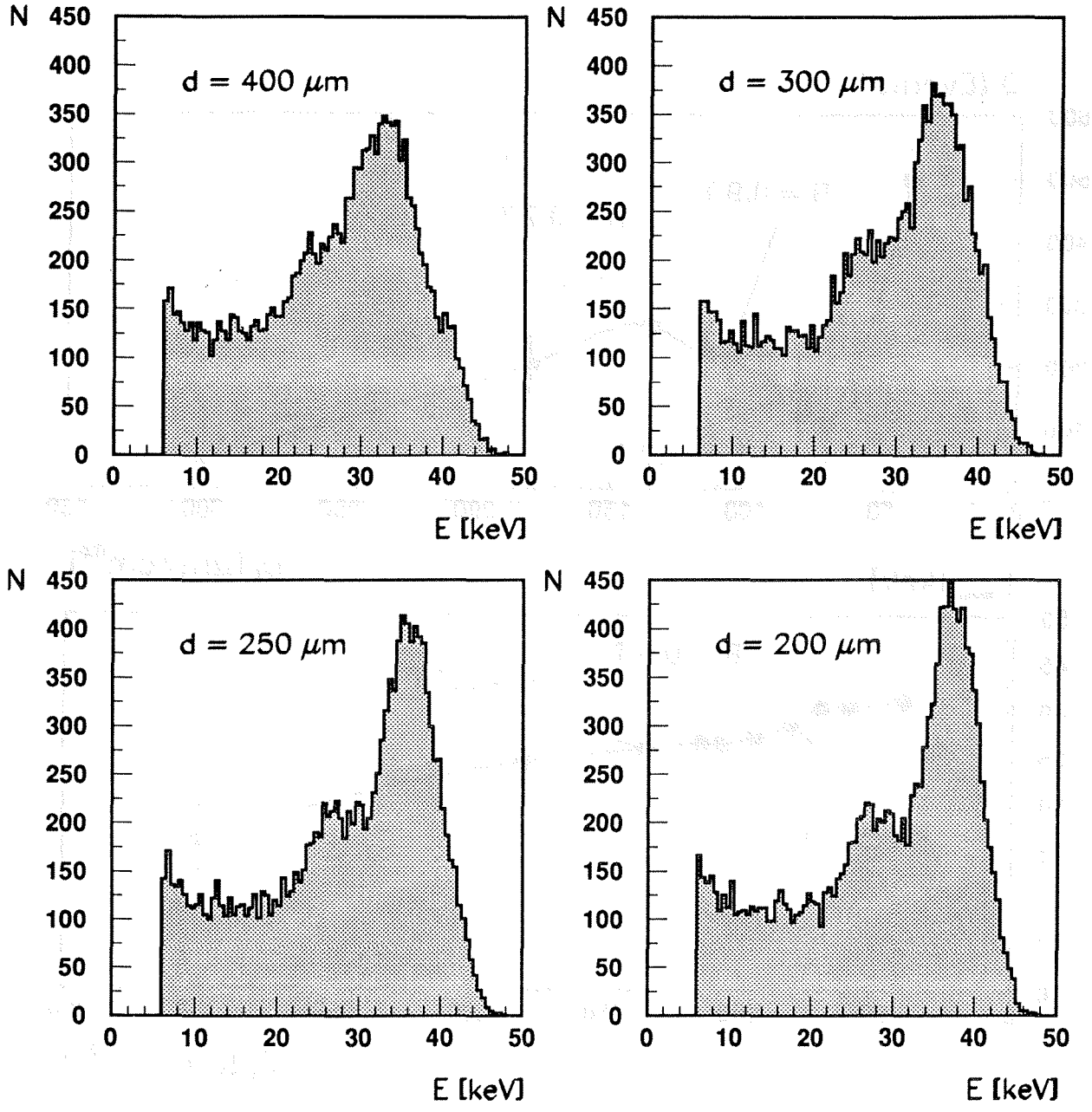

Figure 5.12: *Monte Carlo Kr-peaks for different effective geometries of the grid. The diffusion coefficient was $D_t = 81\mu m/\sqrt{cm}$. The module length was 65cm.*

down in this region nearly by a factor of ten. This produces a time delay of roughly $1\mu s$. Due to this time delay we expect from the increased diffusion a better Kr resolution. Figure 5.14 compares the measured Kr-peaks for the modules 113 and 137[7]. The measured data show very nicely the expected behaviour.

[7]The measured data were provided by T. Tabarelli [42].

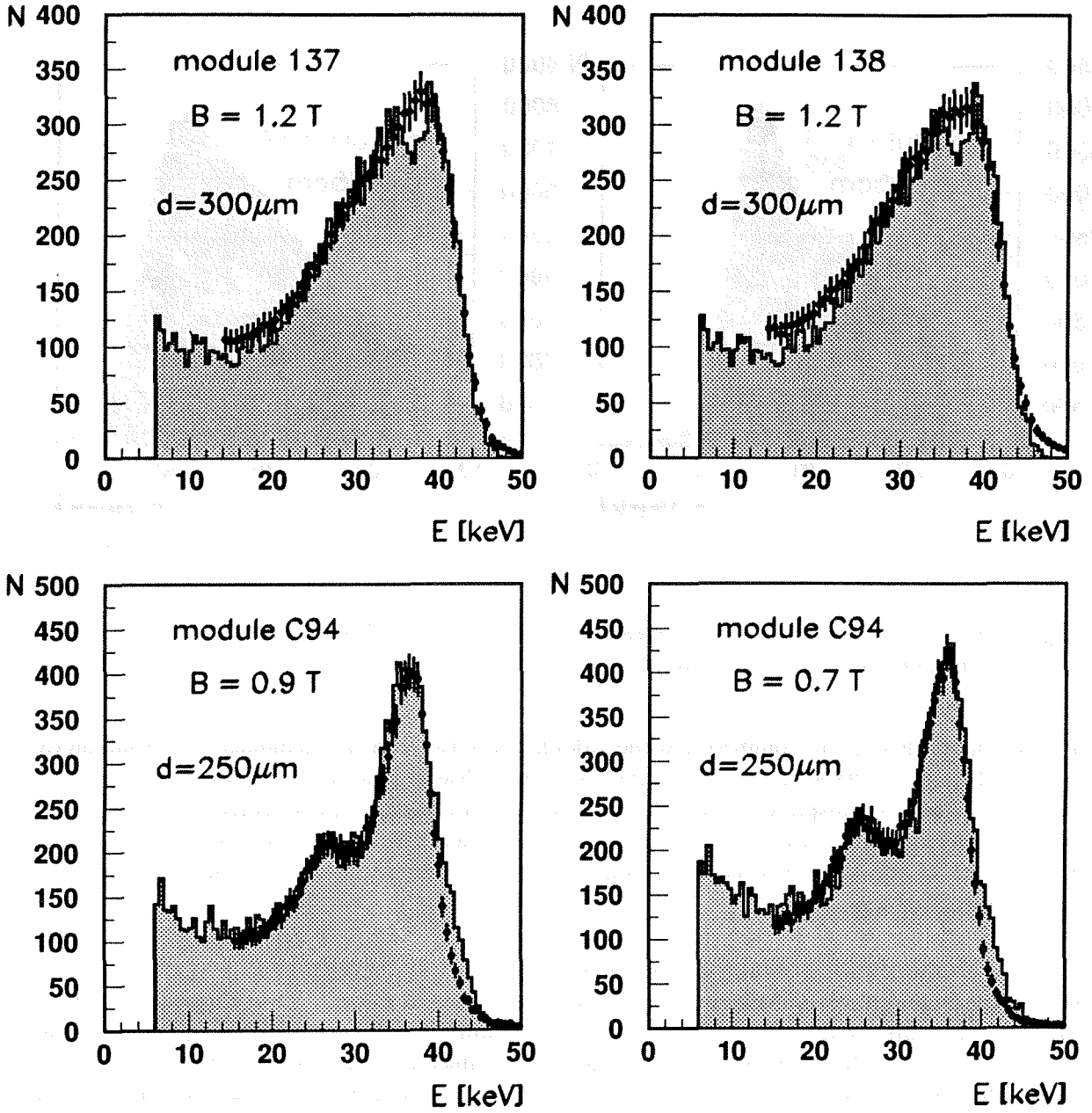

Figure 5.13: *Comparison of the Kr-peak between data and Monte Carlo for modules 137, 138 ($B = 1.2T$) and module C94 ($B = 0.9T$ and $B = 0.7T$).*

5.6 Summary

The transparency of the graphite grid plays an important role for the resolution of the Kr-peak. A good resolution is needed to fit the peaks when performing a Kr calibration. In order to perform a pad to pad calibration all 18432 channels need to be fitted using an automated procedure. Since the Kr-Monte Carlo reveals the dependence of the resolution on electric

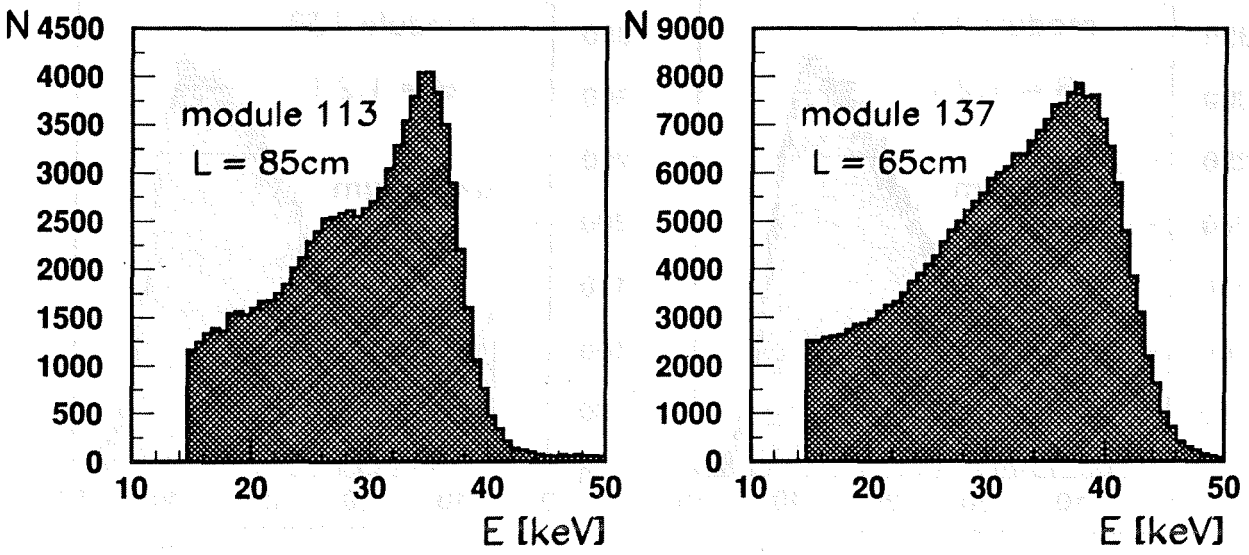

Figure 5.14: *Kr-peaks for the modules 113 and 137 in the HPC. Module 113 has a length of 85cm, module 137 is a short module.*

and magnetic fields, the conditions while taking a Kr-run can be optimized. The magnetic field in DELPHI is fixed at $1.2T$, but the chamber voltages can be raised for the purpose of calibration. This corresponds, in our Monte Carlo, to a change of the effective geometry. The increased sucking effects at higher chamber voltages lead to an improved resolution in the Kr-peak. Kr calibration test runs taken at $1350V$ chamber voltage confirmed this prediction in an impressive way.

The Kr Monte Carlos produce a consistent picture of the dependence of the Kr signal on the magnetic and electric fields and on the various geometric effects. The differences between brass and graphite chambers are understood. The dramatic influence of the magnetic field has been discussed in a detailed way. The change in resolution for different electric fields is due to an effect of transparency. Thus one can say that a Kr calibration for graphite chambers is possible in a same way as for brass chambers.

In parallel to this Kr simulation, a Monte Carlo program simulating showers and minimal ionizing particles (mip's) has been developed. Some results of it are mentioned here. The screening by the graphite insert perpendicular to the sense wire leads, for muons of fixed energy, to an improved energy resolution compared to the brass chamber. The explanation is that the bad regions next to the lead wires, which introduce large fluctuations, are cut away. Furthermore, this cut in the y-direction leads to an increased attenuation length[8] for graphite chambers as compared to brass chambers. Consistent results have been achieved for Kr-, mip- and shower-Monte Carlo. The predicted values for the attenuation length are in good agreement with the measurements for graphite and brass chambers in the West Area.

[8] For more details see Ref. [43].

Chapter 6

A Longitudinal Shower Fit for Electron Identification

For many kinds of physics analysis, it is important to have a good identification of low energetic electrons. The main methods used to study both inclusive and exclusive decay channels involving B hadrons include the semi-leptonic decay modes into electrons and muons. This is motivated by the relative high transverse momentum spectra (with respect to the beam axis), as well as by the sizeable semi-leptonic branching ratio of the B hadrons. The measurement of forward-backward-asymmetries and the $B\bar{B}$ mixing are typical examples of these kinds of analyses. Moreover, there are several decay channels $B \rightarrow J/\psi X$ involving only charged particles, therefore allowing a complete reconstruction of the parent B mass and energy. This allows in principle a detailed study of individual lifetimes and of the b fragmentation. The J/ψ can be identified by the leptonic decay modes $J/\psi \rightarrow e^+e^-$ or $J/\psi \rightarrow \mu^+\mu^-$. The first step for such an analysis is to identify the leptons in the presence of other tracks. For typical hadronic events ($Z^0 \rightarrow q\bar{q}$) the rate of the lepton production is of the order of 2 %. Therefore a misidentification probability of at least 1 % together with a good efficiency is needed. The electron momentum spectrum of the semi-leptonic B decay has its maximum at roughly 3 GeV so that a electron identification algorithm needs to work mainly in the low energetic region of the HPC.

In order to study branching ratios or polarization effects in τ-decays the channel $\tau^- \rightarrow e^-\bar{\nu}_e\nu_t$ is often studied. The identification of the produced electrons is easier than in the case of B decays because the electrons are not surrounded by a jet environment. Moreover, the topology of the whole event can give some powerful tools for electron identification[1]. The momentum spectrum of this channel peaks nearly at 8 GeV.

This section describes the longitudinal shower fit in the nine layers of the HPC using the Γ-distribution introduced in section 3.11.1 as a tool for electron identification. The goal is to obtain a working algorithm in the barrel region which is producing a χ^2 for the distinction between electromagnetic showers (e^+, e^-, γ) and minimal ionizing particles (mainly π^+, π^-). As it will be shown later the algorithm works also in θ-cracks of the HPC and can give an energy correction for these regions. Some other important tools for the electron identification such as

[1] For more details see also section 6.1.4.

dE/dx from the TPC, E/p-cut, ΔZ-cut or $\Delta\phi$-cut will also be explained here briefly as the overall method of electron identification depends on all of these. The algorithm of longitudinal shower fitting has been tested using data and Monte Carlo from 1991 (DELANA_E) and 1992 (DANA92_C). Mainly Bhabha events (section 6.1.2), Compton events (section 6.1.3) and τ events (section 6.1.4) have been considered for testing because their electrons can be separated very pure just using the topology of the events. In order to get realistic values for efficiency and purity in jets, the behaviour of the algorithm has been studied using 1991 B - Monte Carlo (section 6.1.1) and 1992 K^0- data (section 6.1.5).

6.1 Test Samples for the Electron Identification

For the development of an electron identification routine huge test samples of electrons, pions and jet events were needed.

6.1.1 Monte Carlo Samples

The following Monte Carlo events were used for the studies. A fraction of them was generated using the CSF[2] at CERN.

- 10000 Bhabha events DELANA_E
- 10000 Bhabha events DANA92_C
- 32000 single electrons DELANA_E
  ($E = 0 - 45.6\ GeV$ and $|\cos\theta| < 0.72$)
- 3000 single electrons DELANA_E
  ($E = 2.5, 5.0, 10, 20, 30, 45\ GeV$ and $|\cos\theta| < 0.72$)
- 32000 single electrons / HPC part reprocessed with DANA92_C
  ($0 - 45.6\ GeV$ and $|\cos\theta| < 0.72$)
- 22000 single pions DELANA_E
  ($2 - 45.6\ GeV$ and $|\cos\theta| < 0.72$)
- 31000 $\tau\bar{\tau}$ events DELANA_E
- 2650 $b\bar{b}$ events DELANA_E
  (one b from each event was forced to decay due to weak interaction in $b \rightarrow Xe\nu$)

6.1.2 Real Data Bhabha Events

For the studies Bhabhas from 1991 (DELANA_E) and 1992 (DANA92_C) are used. The selection criteria are the same as described in section 4. In order to study Bhabha showers in θ-cracks events with deposits in θ-cracks are included in the samples.

[2] CSF: Central Simulation Facility

6.1.3 Compton Scatter Events

In order to provide a sample of events with clearly identified electrons of known energy significantly lower than the Bhabhas entering the HPC, we consider Compton scattering.

$$e^+e^- \rightarrow e^+e^-\gamma \tag{6.1}$$

The photon is detected in FEMC or SAT, the electron (or positron) is scattered at a wide angle and enters the HPC, and the positron (or electron) goes down the beam pipe. The mean energy of Compton electrons lies around 4 GeV.

Consider the kinematics of final state radiation. By conservation of energy and momentum, the radiation of a final state scattered electron or positron must be longitudinal. Therefore, the electron will form together with the radiated photon(s), in most cases one shower with an energy of 45 GeV. This means that this case cannot be distinguished from normal Bhabha scattering.

But if we consider initial state radiation, then by conservation of energy and momentum that radiation must also be longitudinal. The radiating lepton will disappear undetected with reduced energy down the beam pipe. The other incident lepton scatters now elastically on the radiated photon with some wide angle and is detectable in the HPC. The photon can either be found in the FEMC or the SAT. The photon-lepton scattering is back-to-back in its own rest frame. In the overall center of mass system it is not back-to-back since one lepton has escaped down the beam pipe. The Lorentz transformation from the local rest frame to the overall center of mass system will produce the momentum triangle of conservation of momentum. One lepton moment is along the beam axis (E_{invis}, $\vec{p}_{invis}$). Vectorially it sums up with the other lepton (E_{vis}, $\vec{p}_{vis}$) and the photon (E_γ, $\vec{p}_\gamma$) to zero (see Figure 6.1). The

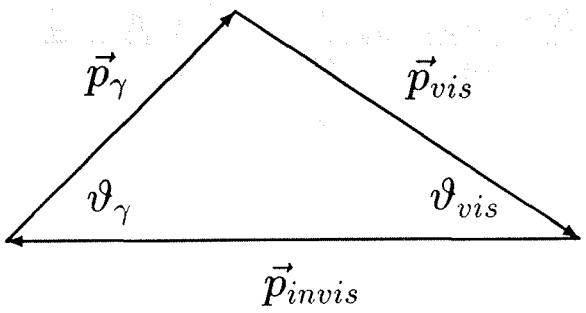

Figure 6.1: *Momentum triangle for Compton scattering in DELPHI*

conservation of momentum and energy can be written as:

$$E_\gamma + E_{vis} + E_{invis} = \sqrt{s} \tag{6.2}$$

$$\vec{p}_\gamma + \vec{p}_{vis} + \vec{p}_{invis} = 0 \tag{6.3}$$

After some algebra we obtain [44]:

$$p_{vis} = \sqrt{s}[(1 + \cos\vartheta_{vis}) + \left(\frac{\sin\vartheta_{vis}}{\sin\vartheta_\gamma}\right)(1 + \cos\vartheta_\gamma)]^{-1} \tag{6.4}$$

With this formula, p_{vis} can be calculated from $\sqrt{s}$ and the measured angles ϑ_γ and ϑ_{vis}. In order to increase the statistics of electromagnetic showers in the HPC one could try to select photons entering the HPC, where the corresponding electron is detected in FEMC and SAT. The efficiency for this process is very low since the forward tracking is difficult, as there are two radiation lengths of material in front of the calorimeter. For the selection of Compton events the following standard selection cuts from the leptonic teams have been applied:

- one charged track to the HPC with an associated shower
- one shower in the FEMC (SAT) of energy greater than 10 *GeV* and less than 45 *GeV*
- acoplanarity less than 10°

Figure 6.2 shows the momentum spectra for 1991 and 1992 Comptons[3]. For DELANA_E 2175 Comptons were selected, for DANA92_C 5112 were found.

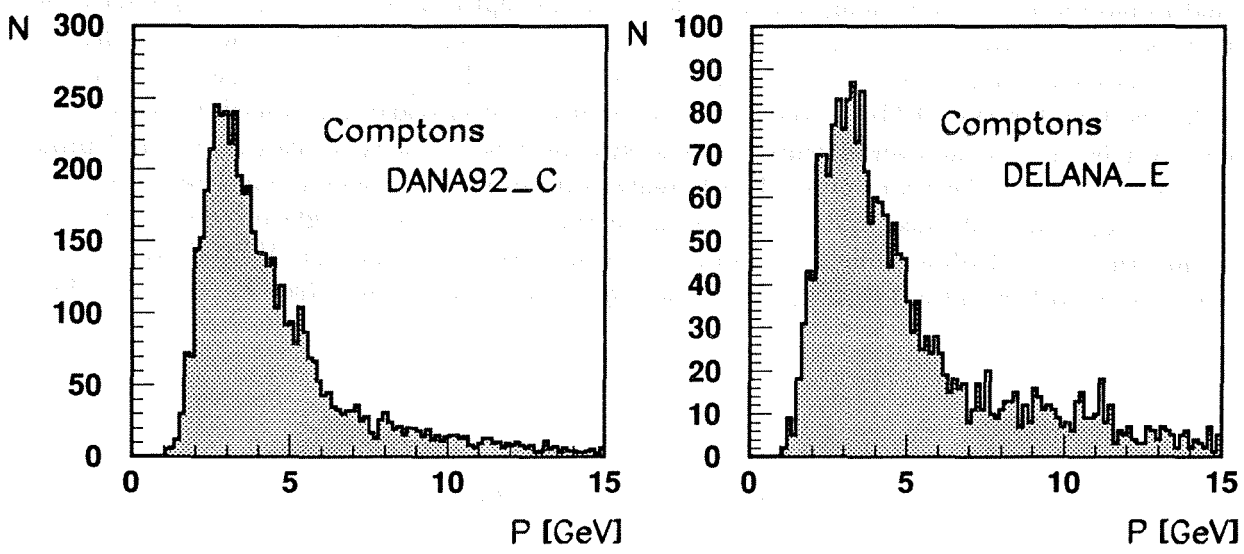

Figure 6.2: *Momentum spectra for Comptons (DELANA_E and DANA92_C)*

6.1.4 τ – Events

For the development of our electron identification routine several tests were done using the electron channel from τ-decays ($\tau^- \rightarrow e^- \bar{\nu}_e \nu_\tau$). Before identifying of this exclusive τ-decay an enriched sample of $\tau^+\tau^-$ events was selected with a loose 'filter'. For this, the standard selection criteria from Team 3 were used. The selection was optimized to minimize distortions of the momentum spectrum and decay mode dependent biases. The selection criteria mainly consist of the following [46]:

[3]The selection was done using the routine ELCOMP provided by the electron identification task group [45].

- one track in the barrel ($|\cos\theta| < .74$)
- nprongs ≤ 12
- $2 \leq Ntracks \leq 8$
- at least 1 track in both hemispheres
- isolation angle $> 90°$
- visible energy $> 2\ GeV$
- $P_{rad} < 200\ GeV/c$ and $E_{rad} < 200\ GeV$

42000 events passed this pre-selection for 1991 data (DELANA_E). In order to separate the electron channel from this sample it was necessary to apply some additional cuts. Figure 6.3 shows the topology of an event where one τ decays into an electron and two neutrinos. Since there is only one charged track (the electron) in one hemisphere, it is easy to find an algorithm for the separation of this topology. The goal is then to reject channels with similar topologies like $\tau^- \rightarrow \mu^-\bar{\nu}_\mu\nu_\tau$, $\tau^- \rightarrow \pi^-(K^-)\nu_\tau$ or $\tau^- \rightarrow \rho^-\nu_\tau$. The following selection criteria have been applied[4]:

- $E_{HPC} < 75\ GeV$ in whole event to reject Bhabhas
- $\theta_{Acc} > 1°$ to reject e-pairs and μ-pairs
- divide event in two hemispheres and accept only tracks isolated in a hemisphere
- $N_{MUB} = 0$
- $E_{HAD} < 2\ GeV$
- dE/dx-Cut

After this procedure an enriched electron sample was obtained. The purity evaluated from the Monte Carlo was more than 90%. The advantage of the usage of this channel is that the selection can be done very pure. One obtains an electron sample with drastically higher

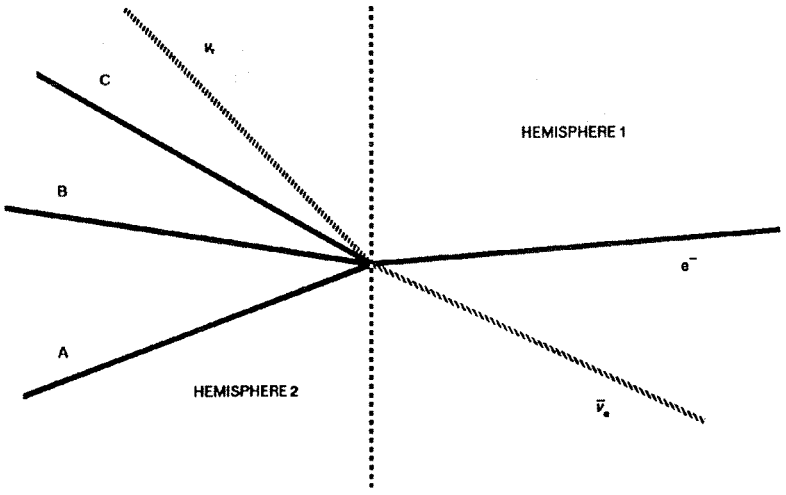

Figure 6.3: *Topology of the electron channel in a τ-decay. Only one charged track (e^-) is isolated in one hemisphere while the two neutrinos disappear unobserved. The particles A, B and C from the decay of the second τ define the second hemisphere.*

[4]For more details see also Ref. [47].

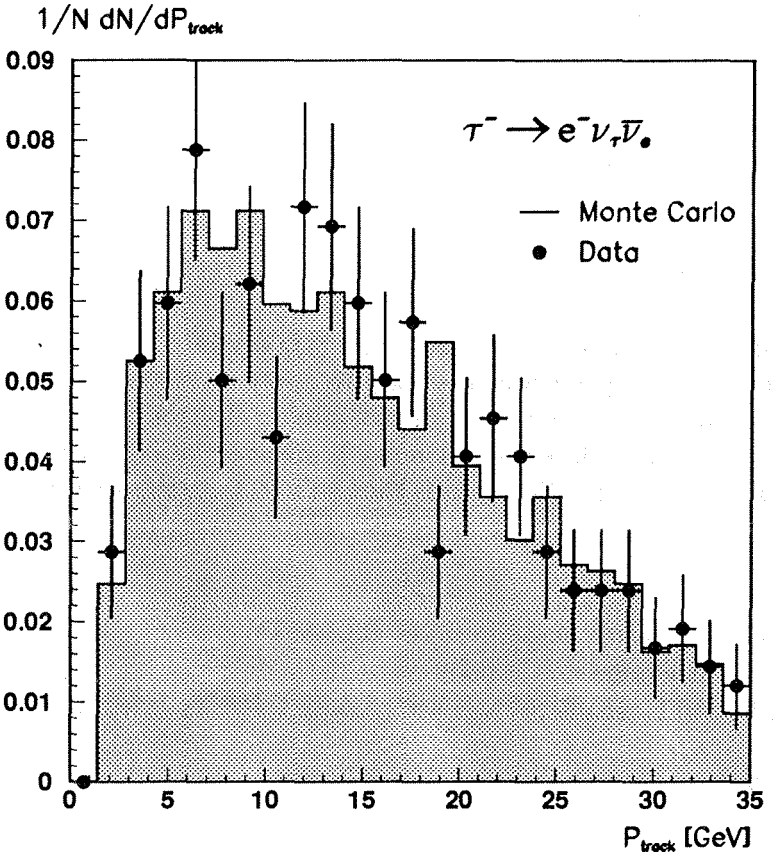

Figure 6.4: *Comparison of the momentum spectra between τ data and Monte Carlo.*

energies as the Compton electrons and lower as the Bhabhas. This selection was done for data and Monte Carlo of 1991 (DELANA_E). From the Monte Carlo sample we were left with 1500 electrons while the data sample delivered roughly 500 electrons. A comparison of the momentum spectra is shown in Figure 6.4.

6.1.5 K^0 – Events

In order to obtain a pure background sample of pions we used an enriched multi-hadronic sample of K_S^0 's, which decay in 68.61% of the cases into two charged pions. The selection of this sample was done on 1992 data (DANA92_C) by the hadron identification task group [48]. The K^0 (50% K_S^0 and 50% K_L^0) has a mass of [31]:

$$m = 497.671 \pm 0.031 MeV. \tag{6.5}$$

For the mean lifetime in its rest frame, the following values are quoted in the literature [31]:

$$\begin{aligned} K_S^0: \qquad \tau &= (0.8922 \pm 0.0020) \cdot 10^{-10} s \\ c\tau &= 2.675 cm \end{aligned} \tag{6.6}$$

$$K_L^0: \qquad \tau = (5.17 \pm 0.04) \cdot 10^{-8} s \qquad c\tau = 15.5m \tag{6.7}$$

In order to extract the pion tracks from these multi-hadronic events, the invariant mass was calculated for all possible combinations of two charged tracks using the assumption that these particles have pion mass ($m = 139.568 MeV$). Two pions which result from the decay of a K_S^0 will produce an invariant mass near the K^0 mass. Two arbitrary particles will normally produce an invariant mass which is far from the K^0 mass and thus easily can be rejected. Demanding the decay length for the K_S^0 to be smaller than $29cm$ and the opening angle between the two pions at the decay point to be smaller than 17° leads to a nearly pure pion sample. Figure 6.5 shows the calculated invariant mass for all possible combinations of particles together with the momentum spectrum of the pions. After the cut $0.47\ GeV < X_{mass} < 0.51\ GeV$ a sample with roughly 15000 pions was available.

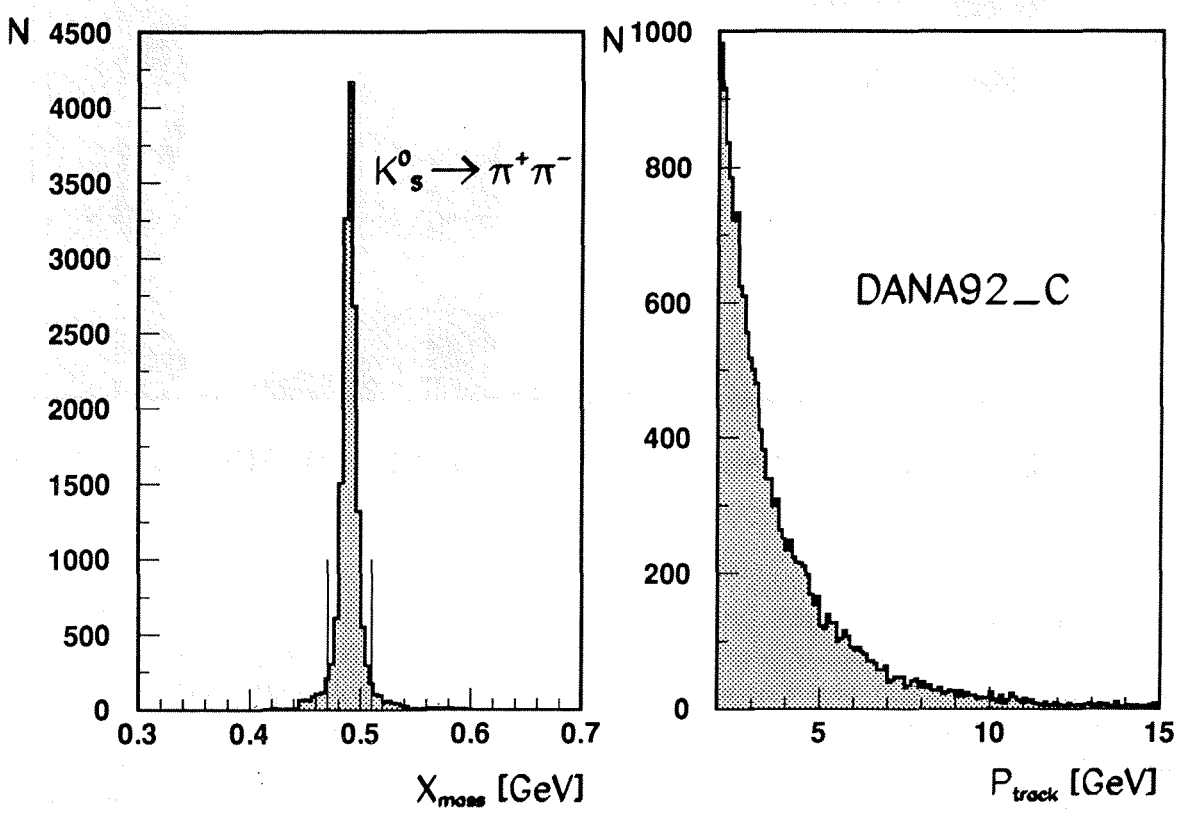

Figure 6.5: *Invariant mass and momentum spectrum of the K_S^0-signal for 1992 data (DANA92_C). The Figure shows also the cut in the invariant mass which was applied in order to get a pure pion sample [32].*

6.2 Tools for the Electron Identification in DELPHI

The identification of electrons can be accomplished by exploiting the physical differences of the interactions of electrons and hadrons with matter. As it is shown in chapter 3, the electron has a much different behaviour than, for example, the pion because it has a very small mass and does not participate in strong interactions.

The track reconstruction for electrons in DELPHI is more difficult than for normal hadrons, because the electrons suffer bremsstrahlung losses due to the material in front of the calorimeter. Figure 6.6 shows the statistics of electron and pion reconstruction in 2650 $b\bar{b}$–Monte Carlo events (DELANA_E). For these calculations only particles with $p > 2.0\,GeV$ and $|\cos\theta| < 0.72$

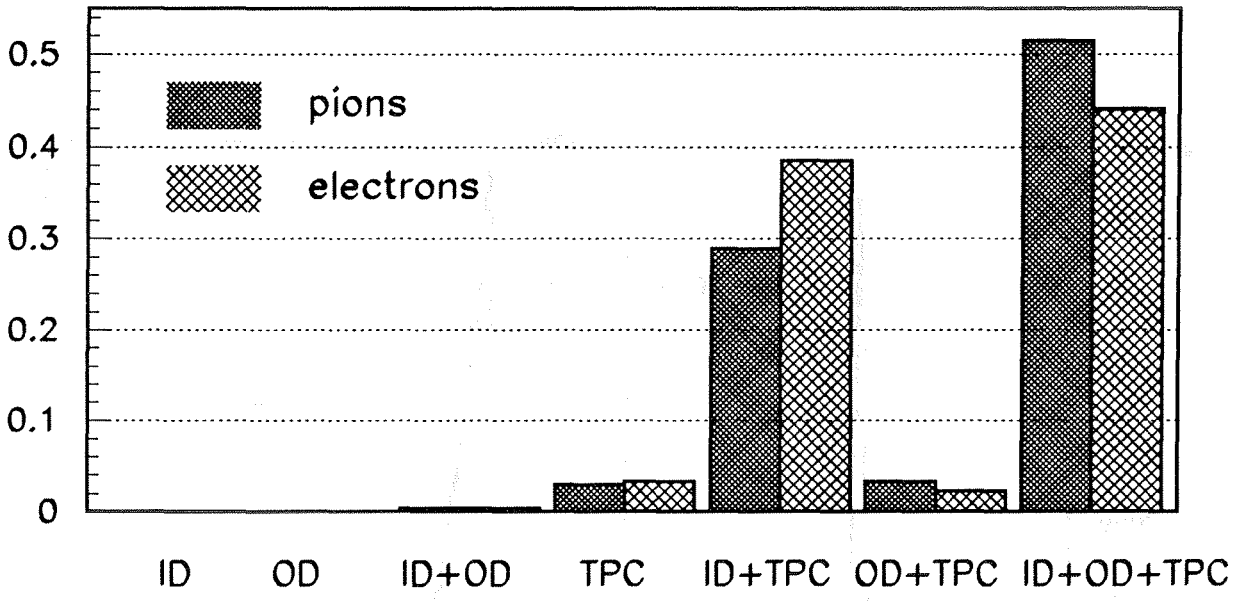

Figure 6.6: *Statistics of electron and pion reconstruction in $b\bar{b}$–Monte Carlo (2650 Events). For both electrons and pions with $p > 2.0$ GeV and $|\cos\theta| < 0.72$, the fraction of particles was calculated for which the reconstruction consist of ID, OD, ID+OD, TPC, ID+TPC, OD+TPC or ID+OD+TPC. The main difference between the electrons and pions is that outer detector hits are missing nearly 8% more often in the electron reconstruction than in the pion reconstruction. Roughly 10% of the electrons and pions from the simulation bank have no link to the reconstruction bank [32].*

were considered. The Figure shows the probabilities that a reconstruction consists of ID, OD, ID+OD, TPC, ID+TPC, OD+TPC or ID+OD+TPC. It becomes clear that the OD in the full reconstruction for electrons is missing 8% more often than for pions. This can be explained by the high material concentration inside DELPHI. Due to the radiation of a hard bremsstrahlung photon the electron suffers distortion from its expected helical track. Because

of the excellent spatial resolution of the outer detector ($\sigma_{R\phi} = 110\mu m$), the OD-hit is often not linked to the original track by the reconstruction algorithm[5].

The material in DELPHI in front of the HPC is mostly concentrated at three radii which are located between TPC and OD.

$$\begin{aligned} R &= 127cm \quad 0.32X_0 \\ R &= 149cm \quad 0.16X_0 \\ R &= 191cm \quad 0.18X_0 \end{aligned}$$

Together with the material of the beam pipe and the vertex detector this leads roughly to $0.7X_0$ in front of the barrel calorimeter for $\theta = 90°$. This means that, on average, the electron energy is reduced by a factor of $e^{-0.7} = 0.497$ before reaching the HPC. From simulation studies with HPCSIM it is known that a generated electron of 45 GeV, after the successive processes of bremsstrahlung, pair production and the generation of δ-electrons, enters the HPC as an avalanche of roughly 100 particles. For most of the cases, these particles appear in the same shower. In the case of the radiation of a hard photon separate showers can be formed in the HPC. This situation is more probable for low energetic electrons because the tracks, due to the low momenta, are more curved and this leads to a better separation in $R\phi$-direction. A searching algorithm is available, which tries to find the radiated photons in the near of a reconstructed electron using a method of tangent extrapolation.

Apart from these reconstruction problems of electron tracks various numbers of tools for electron identification are available in DELPHI. The main possibilities will be described here briefly, after which a detailed description of the algorithm of longitudinal shower fitting will follow[6].

6.2.1 Shower Shape in the HPC

Due to the processes of pair production and bremsstrahlung, electrons form an electromagnetic shower in the HPC. Apart from cracks and leakage effects, nearly all the energy of the electron is deposited in the calorimeter. In contrast to this, pions can only produce ionization along its path. Due to the drastic reduction of chamber gain in 1991 and 1992 only the Landau and path-length fluctuations are visible. Occasionally, an entering hadron initiates a hadronic shower in the HPC which leads to a large energy deposition. The hadronic shower looks similar to an electromagnetic shower but characteristically starts later in the HPC than an electron shower.

Figure 6.7 shows the longitudinal profile of a typical electromagnetic shower, a shower due to Landau and path-length fluctuations and a hadronic shower. Starting from the expected longitudinal shower profile for an electron shower described with a Γ-distribution[7], an algorithm of longitudinal shower fitting was developed. The algorithm described in this chapter delivers a good χ^2 for case (a) and can be used to reject the cases (b) and (c).

[5]The reconstruction is done by a fast non-fit procedure which is called a *Kalman Filter*.

[6]More details on existing electron identification routines in DELPHI can be found in Ref. [49], [50] and [51].

[7]More information about the Γ-distribution can be obtained from the sections 3.11.1 and 6.3.2.

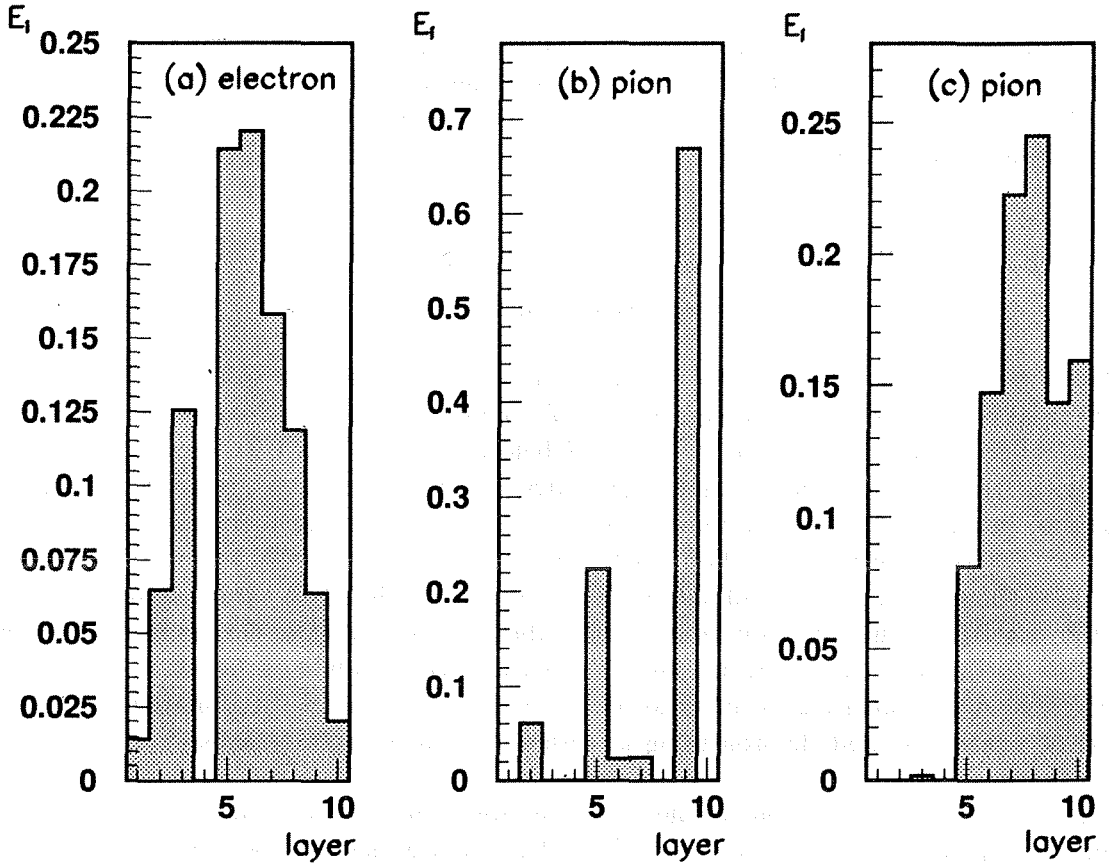

Figure 6.7: *Comparison of the typical behaviour of an electron and a pion in the HPC. The histograms denote the layer energy E_i normalized to the total energy. Histogram (a) shows the typical longitudinal profile of an electromagnetic shower. The effect of Landau and path-length fluctuations is shown in histogram (b). Figure (c) describes the development of a hadronic shower initiated by a pion.*

Moreover, an additional distinction between electrons and hadrons can be derived from the transverse shower shape. A hadronic shower is expected to produce an increased transverse shower width compared to an electron shower. Since the full 3-dimensional structure of the shower is read out, a similar fit can be performed in the transverse shower direction. In the Z direction finely segmented information on the shower shape is available because of a timeslot width of $3.7mm$. In $R\phi$-direction the information on the shower shape is limited by the pad size. However, a strong correlation between longitudinal and transverse shower fit is expected.

6.2.2 The E/p – Cut

In absence of cracks and leakage effects electrons lose all their energy inside the HPC. Hadrons are not expected to shower in the HPC, but rather deposit their energy in the hadron calorimeter. The comparison of the deposited energy in the HPC, E, with the reconstructed momentum p from the tracking detectors leads to a powerful tool for the electron identification. Figure 6.8 shows E/p versus p for single electron Monte Carlo events (DELANA_E) before

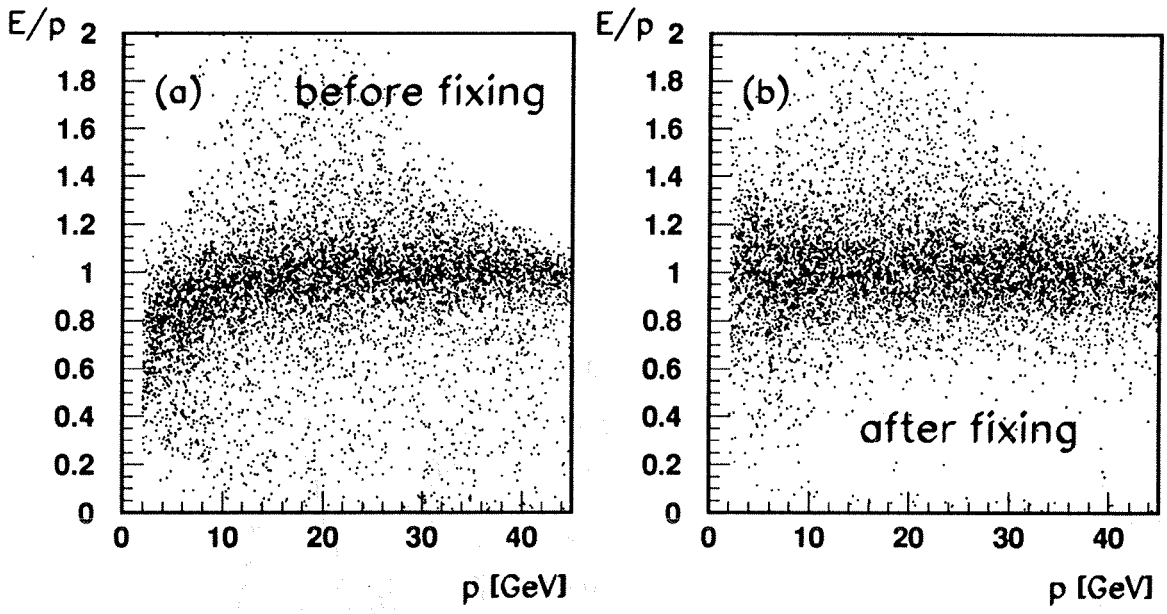

Figure 6.8: *E/p versus p for single electron Monte Carlo (DELANA_E) before and after a fixing was applied. Before the fixing a drop of E/p for electrons less than 15 GeV is clearly visible. Histogram (b) shows the corrected E/p distribution.*

and after a fixing (to be explained below) was applied. Before the fixing for energies greater than 15 *GeV*, E/p is flat and stays at one. Below 15 *GeV* a drop of E/p is clearly visible. At energies around 2 *GeV* E/p decreases to roughly 0.7. This drop can be explained by two effects:

- The material in front of the HPC leads to the radiation of hard photons. If these photons form separate showers in the HPC, their energy is normally not linked to the electron track[8].
- Depending on the chamber gain and the electronic amplification of the HPC only clusters above a certain threshold are visible. Since there is no recovery for this effect inside HPCANA, clusters below this threshold are lost and cannot contribute to the total energy. In the moment HPCANA takes just the sum of all clusters to compute the total energy. Since this effect has a bigger influence on low energetic particles this leads to a contribution to the total drop of E/p.

From Monte Carlo studies with and without matter in front of the HPC, it was found that both effects deliver nearly the same contribution to the total drop of E/p. In order to find an easy way of applying an E/p-cut, the E/p-distribution was fixed to obtain a flat distribution at $E/p = 1$ [9]. The fixing routine also provides a smearing for the Monte Carlo to get a better agreement between the energy resolutions of data and Monte Carlo. The result is shown in histogram (b) of Figure 6.8. Similar flat distributions have been obtained for data (Comp-

[8] Additional information concerning the material in front of the HPC can be found in Ref. [52].

[9] The fixing routine DSFHPC was provided by the electron identification task group [32].

tons) for the processings DELANA_E and DANA92_C.

Histogram (a) of Figure 6.9 shows the E/p distribution for single pion Monte Carlo (DELANA_E). Most of these particles are below $E/p = 0.5$. This means that just by using a simple E/p-cut at 0.5 one can get a quite good separation between electrons and pions. Histogram (b) compares the E/p-distributions for pions (from K^0_S) in the data with electrons (from Comptons). The plot was made using $p > 2$ *GeV* and $E > 0.5$ *GeV*.

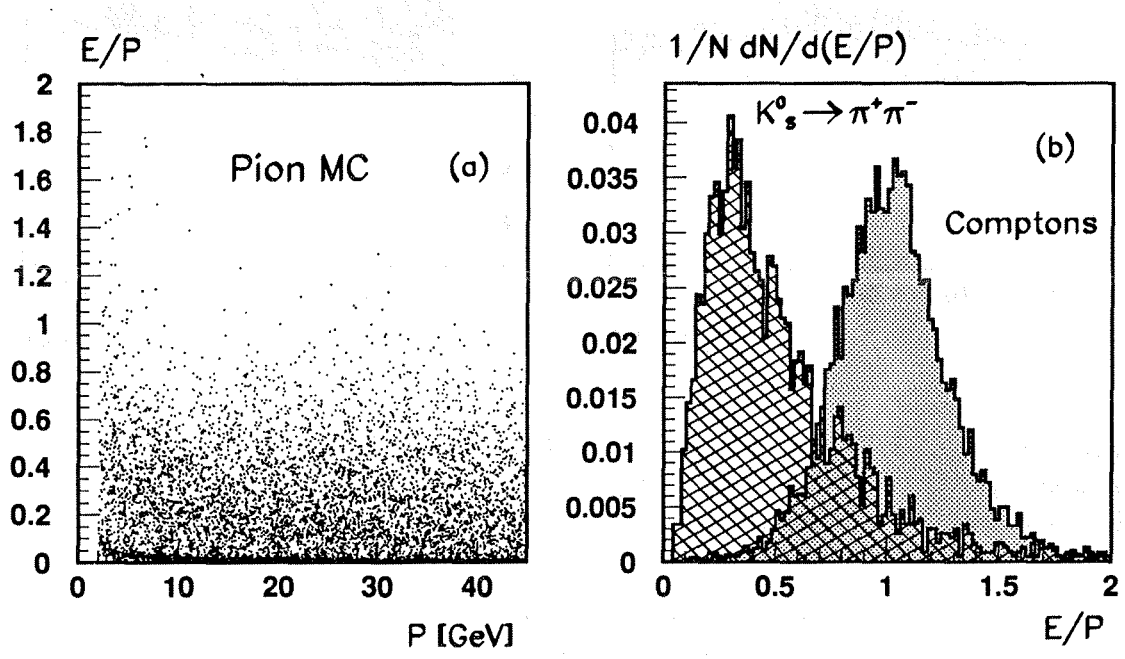

Figure 6.9: *Histogram (a) shows E/p versus p for single pion Monte Carlo (DELANA_E). Histogram (b) compares the E/p-distributions for pions (from K^0_S) and electrons (from Comptons) in data for the processing DANA92_C.*

6.2.3 The dE/dx measured by the TPC

The TPC measures, for each track, the deposited charge in its gas volume using a pad segmented read-out. From our single electron Monte Carlo, it was derived that, on average, more than 130 wires contribute to the signal per track. Such a detailed information can be used as a dE/dx measurement.

Figure 6.10 shows a comparison of the dE/dx measurement between single electron and single pion Monte Carlo (DELANA_E). It can be seen that electrons in the studied momentum range are in the Fermi plateau, while the pions are still in the relativistic rise. Especially for energies below 10 *GeV* a separation between pions and electrons is easily possible. For the two samples in the momentum range between 2 *GeV* and 10 *GeV* the following mean values and standard deviations can be obtained:

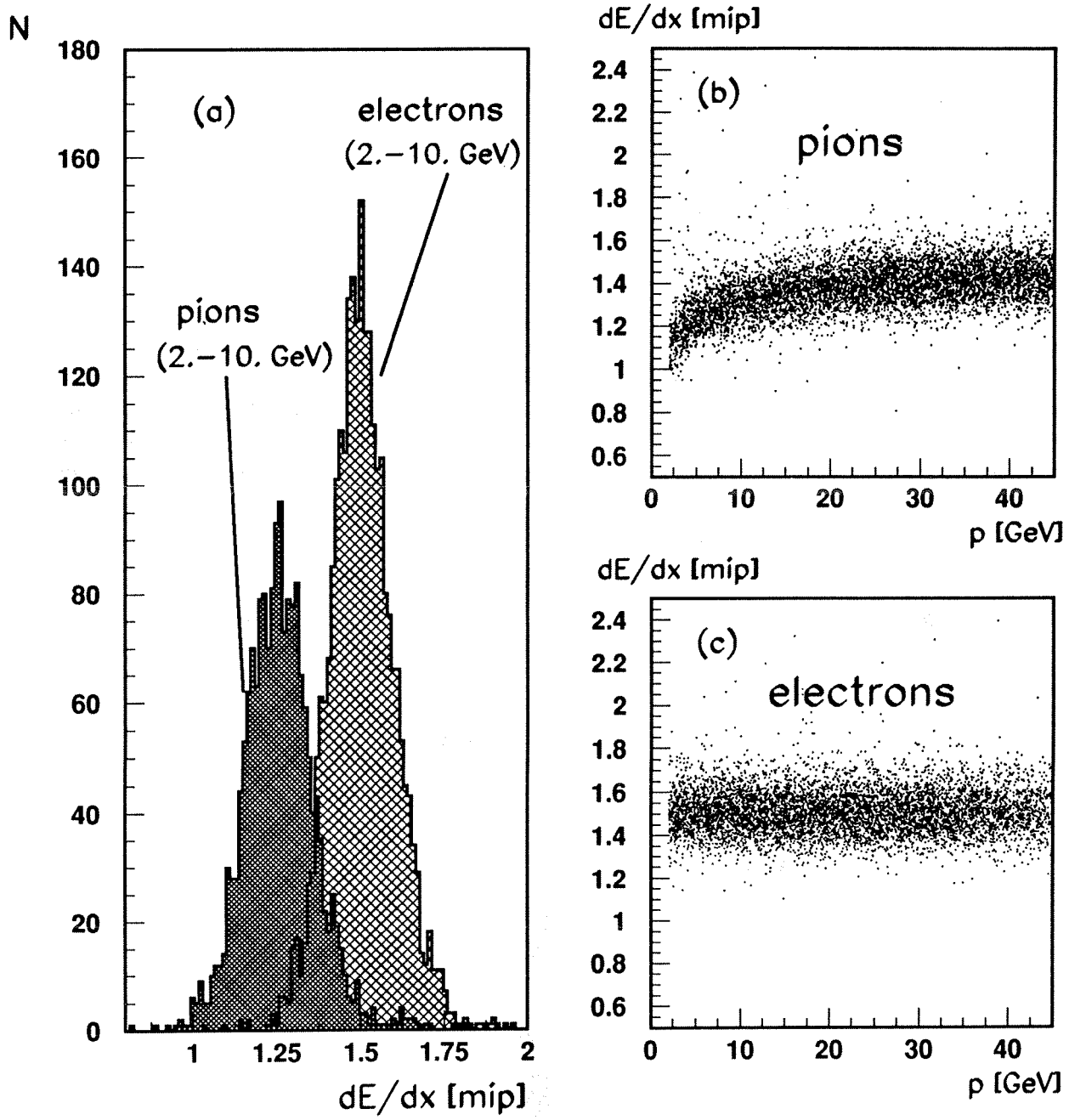

Figure 6.10: *dE/dx for single pion and electron Monte Carlo (DELANA_E) in units of mip. While the pions are still in the relativistic rise the electrons in the studied energy region are on the Fermi plateau (histograms (b) and (c)). For particles with momenta less than* 10 *GeV a separation is possible just by applying a simple cut in dE/dx. (histogram (a))*

electrons:	$M_e = 1.500\ mip$	$\sigma_e = 0.091\ mip$
pions:	$M_\pi = 1.256\ mip$	$\sigma_\pi = 0.097\ mip$

A cut at about 1.5 standard deviations below the expectation value of $1.5 mip$ for electrons provides a significant additional rejection of pions while retaining most of the electrons. Also,

the hadrons removed in this manner can work as a hadronic test sample for other electron identification tools (e.g. the longitudinal shower fit). This enables measuring of efficiencies essentially within the data and relaxes the requirements on the Monte Carlo.

6.2.4 The $Z_{HPC} - Z_{TPC}$ Cut

Another method of rejecting hadronic particles results from using a $\Delta Z = Z_{HPC} - Z_{TPC}$ plot. Z_{TPC} denotes here the Z position of the track extrapolation to the starting radius of the shower, while Z_{HPC} describes the Z position of the shower axis at this starting radius. Since hadronic events produce on average only a few clusters in the HPC, only a very crude shower axis can be defined. In contrast for electromagnetic showers with several dozen clusters this axis is defined very well. Figure 6.11 shows the ΔZ-distributions for different data samples (DANA92_C). Applying a cut at e.g. 1.5 σ for the electrons, leads to an additional rejection of pions.

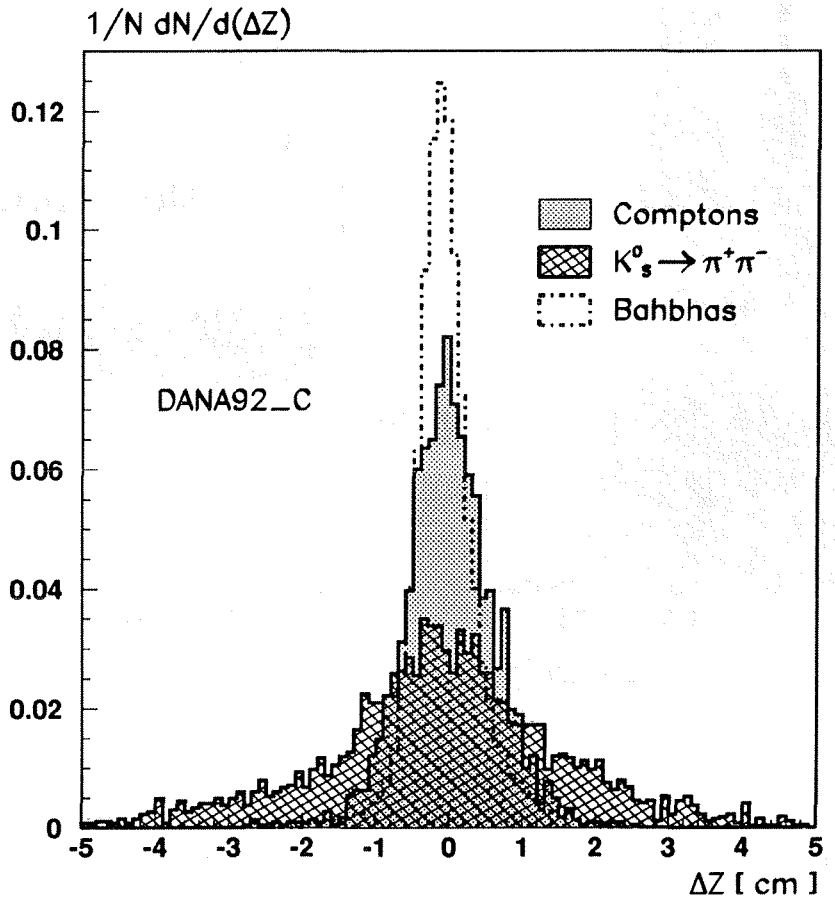

Figure 6.11: $\Delta Z = Z_{HPC} - Z_{TPC}$ *for different data samples from the processing DANA92_C. The electrons are represented by 1992 Bhabhas and Comptons. The pions are isolated from the* K^0_S*-decay into two charged pions.*

6.2.5 Other Methods

Other geometrical methods like $\Delta\varphi = \varphi_{HPC} - \varphi_{TPC}$ have been tested and applied successfully. φ_{HPC} denotes the direction of the shower axis at the starting point of a shower, while φ_{TPC} results from the φ-direction of the track extrapolation at this starting point. Since there are differences between the number of clusters in showers for electrons and pions the $\Delta\varphi$-distributions look different and can be used for separation algorithms.

In order to reach higher purities one can try to make a cut on the deposited energy in the hadron calorimeter. Since the segmentation of the hadron calorimeter is very crude, the deposited energy in jets cannot be linked to single tracks and the information can only be taken as a veto. Another veto can be taken using the muon chambers to reject muons from an electron sample.

Furthermore, tests have been applied using the information of the barrel RICH detector. It seems possible to get an additional contribution to the electron identification in the energy region below 3 GeV. At least an additional measured track point between TPC and OD will result in an improved track extrapolation.

In order to have a clever algorithm for electron identification, it is sometimes possible to use the whole topology of the event to define a powerful pre-selection. This is sometimes much more effective than to use a fixed procedure for every track. Examples for the usage of the topology of an event have been explained in section 6.1.

6.3 Longitudinal Shower Fit

As described in section 3.11.1, the longitudinal shower shape in a sampling calorimeter can be parametrized using the well known Γ-distribution for the energy release, dE/dt, as a function of shower depth t $[X_0]$:

$$\frac{dE}{dt} = E \cdot \beta \cdot \frac{(\beta t)^{\alpha-1} \cdot e^{-\beta t}}{\Gamma(\alpha)} \quad , \tag{6.8}$$

where E is the shower energy α and β are empirical parameters to be determined from the data. α and β are functions of the initial energy, E, and of the polar angles θ and ϕ of the track extrapolation to the HPC. In this description we consider the dependence of α and β on the angles θ and ϕ to be very small so that a parametrization can just be written as a function of energy E.

$$\alpha = \alpha(E) \tag{6.9}$$

$$\beta = \beta(E) \tag{6.10}$$

The shower depth t is measured in radiation lengths and can be calculated by taking into account the θ- and ϕ-dependent geometrical factors for the material distribution in front of the HPC and the correct material distribution inside the HPC.

Performing a fit we have the three fit parameter E, α and β. This leads to the definition of a χ^2-like variable to quantify the electromagnetic character of a shower profile.

6.3.1 Model for the Material Distribution in DELPHI

Figure 6.12 shows the effective material distribution in front of the calorimeters, measured in radiation lengths, after integration over ϕ as a function of the polar angle θ. The Monte Carlo illustrates the different contributions of TPC, RICH and OD/FCB to the whole material distribution. In our simplified model we neglect the peak due to the TPC and barrel RICH end-plates at 90° and assume a constant material distribution of $0.7X_0$ in front of the HPC. It has to be scaled by a factor $1/\sin\theta$ for the different material thickness as a function of θ. The angle θ here denotes the direction of the track extrapolation at the starting point of the shower.

$$t_0 = \frac{0.7X_0}{\sin\theta} \tag{6.11}$$

In addition to that, an extra $0.43X_0$ for each of the 40 gaps (39 read-out gaps + 1 trigger gap) is considered. It needs to be scaled by a factor $1/(\sin\theta\cos\phi)$ where ϕ denotes the difference between the ϕ-coordinate where the track hits the HPC border and its ϕ-direction at this point. In order to deal with leakage effects, the number of drift gaps is extended to 50 to get a prediction for the deposited energy behind the HPC. The number of radiation lengths t_N in drift gap N can then be calculated in the following way:

$$t_N = t_0 + N \cdot \Delta t \tag{6.12}$$

$$\tag{6.13}$$

$$= \frac{0.7X_0}{\sin\theta} + N \cdot \frac{0.43X_0}{\sin\theta\cos\phi} \tag{6.14}$$

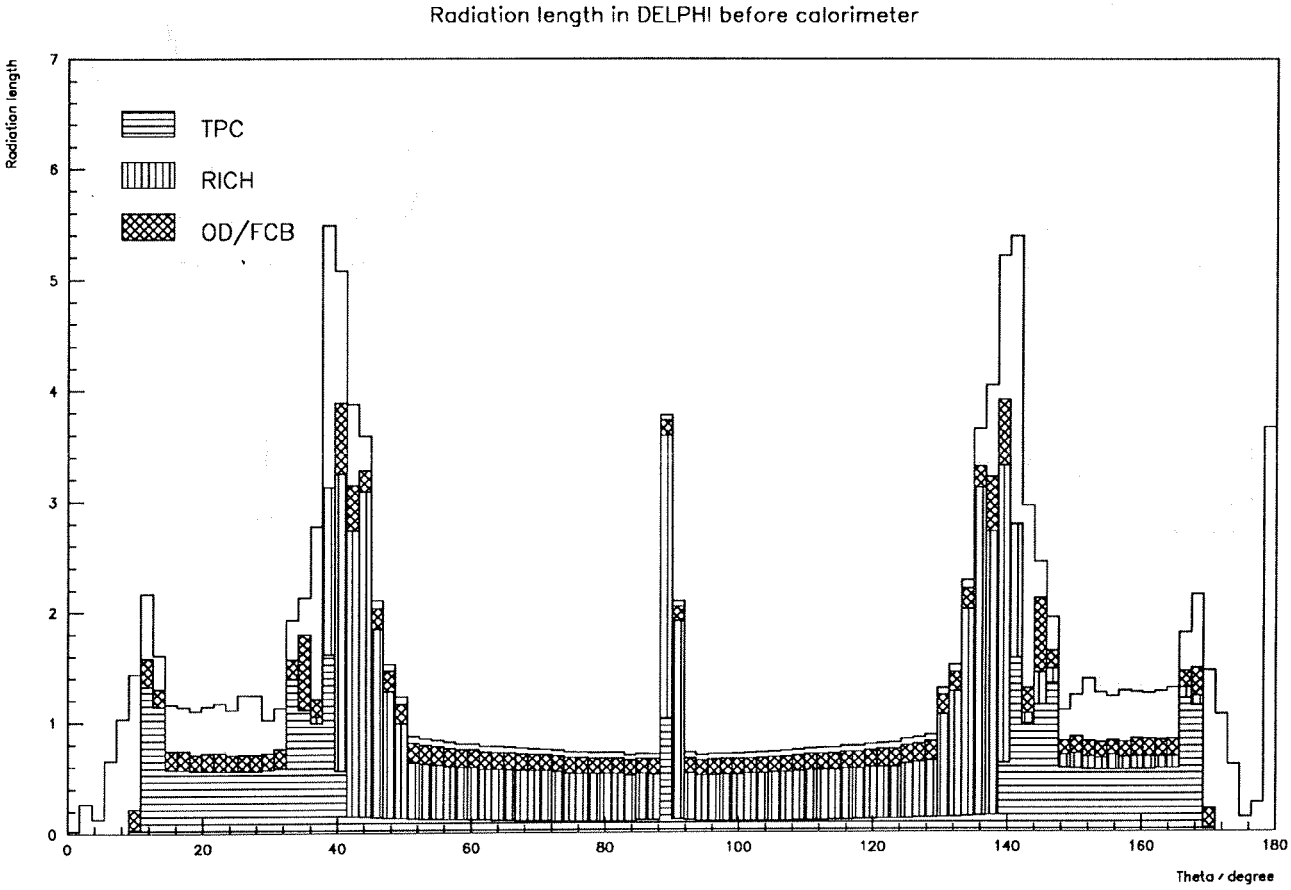

Figure 6.12: *Different contributions of TPC, RICH and OD/FCB to the total material distribution inside DELPHI. The peak at 90° denotes the end-plates of the TPC and the barrel RICH. At angles less than 50° and greater than 130° the influence of the two end-caps leads to a rise of radiation length in front of the FEMC [53].*

$$with \qquad N = 1, 2, ...50. \tag{6.15}$$

The values for N from 1 to 9 correspond to the three first layers with small pads and 3 gaps per layer. $N = 10$ denotes the trigger gap and $N = 11, ...22$ ($N = 23, ...40$) corresponds to the layers with medium (big) pads and 4 (6) gaps per layer. Figure 6.13 shows the simplified model of the material distribution in front of and inside the HPC.

Using these assumptions, one can easily compute the predicted energy per layer E_i^Γ ($i = 1, ...10$) for a shower with energy E and parameters α and β:

$$E_i^\Gamma = \sum_{N=j}^{k} \Delta E_N = \sum_{N=j}^{k} E \cdot \beta \cdot \frac{(\beta t_N)^{\alpha-1} \cdot e^{-\beta t_N}}{\Gamma(\alpha)} \cdot \Delta t \tag{6.16}$$

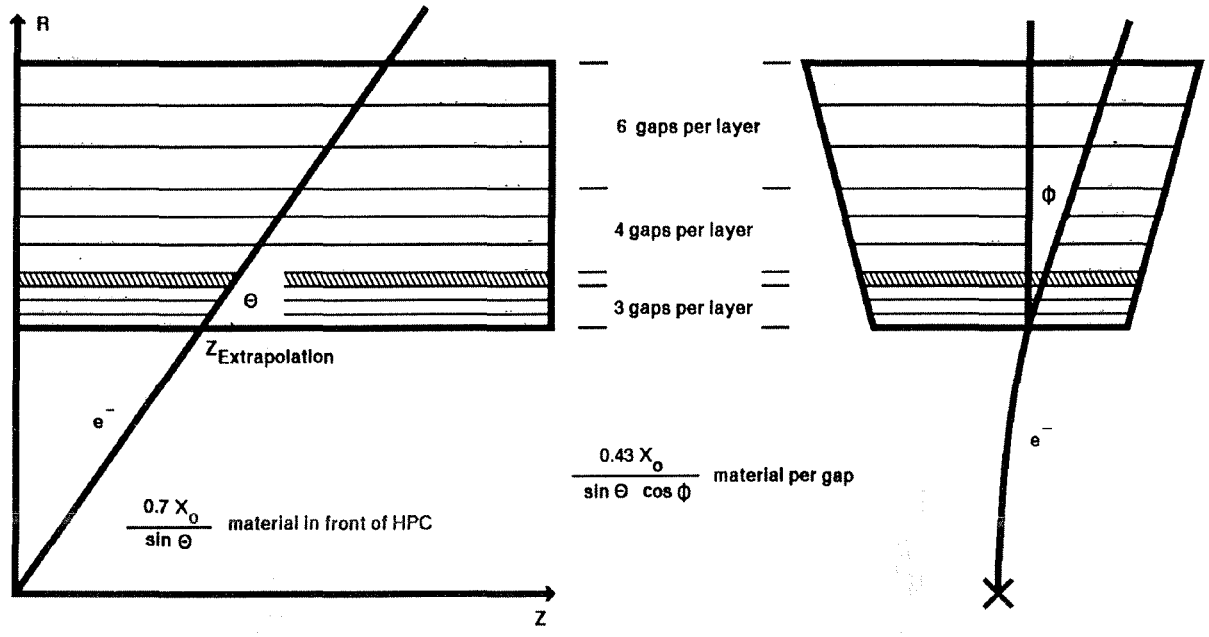

Figure 6.13: *Simplified model of the material distribution in front of and inside the HPC.*

small pads	$i = 1,2,3$	$j = 1 + 3(i-1)$	$k = 3i$
trigger gap	$i = 4$	$j = 4$	$k = 4$
medium pads	$i = 5,6,7$	$j = 11 + 4(i-5)$	$k = 10 + 4(i-4)$
large pads	$i = 8,9,10$	$j = 23 + 6(i-8)$	$k = 22 + 6(i-7)$

The sum of the squares of the differences between the measured energies E_i^{mea} in the 9 HPC layers and the values E_i^{Γ} obtained using this parametrization weighted by their sigmas σ_{E_i}, can then be used as a χ^2-like variable to quantify the electromagnetic character of a shower profile[10]. The next section will describe the parametrization of α and β as a function of energy. Since once such a parametrization is obtained, in addition to that, their deviation of the fit parameters α and β from the expected mean values can be included in the definition of the χ^2 variable. As it will be shown later, this corresponds to the elimination of the first large shower fluctuations.

6.3.2 Energy Parametrization of the Model

The next step in performing a longitudinal shower fit is to find an adequate parametrization of α and β as a function of energy. Bhabhas, for example, have an $\alpha = 6 \pm 1$ and $\beta = 0.7 \pm 0.1$ while for low energetic showers both parameters are smaller. The question is: How does one calculate the α's and β's from the measured energy distributions E_i^{mea} in the layers? For this, the expectation value M_Γ and the variance V_Γ of the Γ-distribution need to be

[10] A more precise definition will be given in section 6.3.4.

calculated. They can be expressed as the first algebraic and the second central moment of the Γ-distribution $f_\Gamma(t)$ [11]:

$$M_\Gamma \equiv < t > \equiv \int_0^\infty t f_\Gamma(t) dt \tag{6.17}$$

$$= \frac{\alpha}{\beta} \tag{6.18}$$

$$V_\Gamma \equiv < (t - < t >)^2 > \equiv \int_0^\infty (t - < t >)^2 f_\Gamma(t) dt \tag{6.19}$$

$$= < t^2 > - < t >^2 \tag{6.20}$$

$$= \frac{\alpha}{\beta^2} \tag{6.21}$$

Using equation 6.8 we can evaluate now the first and second moments from the measured energies E_i^{mea} in a shower.

$$< t >_{mea} = \frac{1}{E} \int_0^\infty t dE \tag{6.22}$$

$$\simeq \frac{\sum_i t_i E_i^{mea}}{\sum_i E_i^{mea}} \tag{6.23}$$

$$< t^2 >_{mea} = \frac{1}{E} \int_0^\infty t^2 dE \tag{6.24}$$

$$\simeq \frac{\sum_i t_i^2 E_i^{mea}}{\sum_i E_i^{mea}} \tag{6.25}$$

The summations here need to be calculated for a single shower over all sampling layers i with the weights 1, t and t^2. Including all this information one can derive first approximations for the values α_{mea} and β_{mea} as a function of the measured energies E_i^{mea} or the moments $< t >_{mea}$ and $< t^2 >_{mea}$.

$$\alpha_{mea} = \frac{< t >_{mea}^2}{< t^2 >_{mea} + < t >_{mea}^2} \tag{6.26}$$

$$\beta_{mea} = \frac{< t >_{mea}}{< t^2 >_{mea} + < t >_{mea}^2} \tag{6.27}$$

The values for α_{mea}, β_{mea} and E will be used as initial values for our three parameter fit. Unfortunately, the α_{mea} and β_{mea} are correlated, since we want to include their deviation from the expectation value in the χ^2 definition. Figure 6.14 shows a correlation plot between α_{mea} and β_{mea} for Bhabha data. The strong correlation is clearly visible.

In order to perform a fit, the solution can either be, to use the full correlation matrix to define the χ^2, or to define some new parameters $V^{mea} = f(\alpha_{mea}, \beta_{mea})$ and $W^{mea} = g(\alpha_{mea}, \beta_{mea})$ which are nearly Gaussian distributed and uncorrelated. It was decided to choose the second method. For V^{mea} and W^{mea} the following expressions satisfy these requirements:

$$V^{mea} = \frac{\beta_{mea}}{\alpha_{mea} - 1} \tag{6.28}$$

$$W^{mea} = \sqrt{\frac{\beta_{mea}^3}{\alpha_{mea} - 1}} \tag{6.29}$$

[11] $f_\Gamma(t)$ has been defined in section 3.11.1.

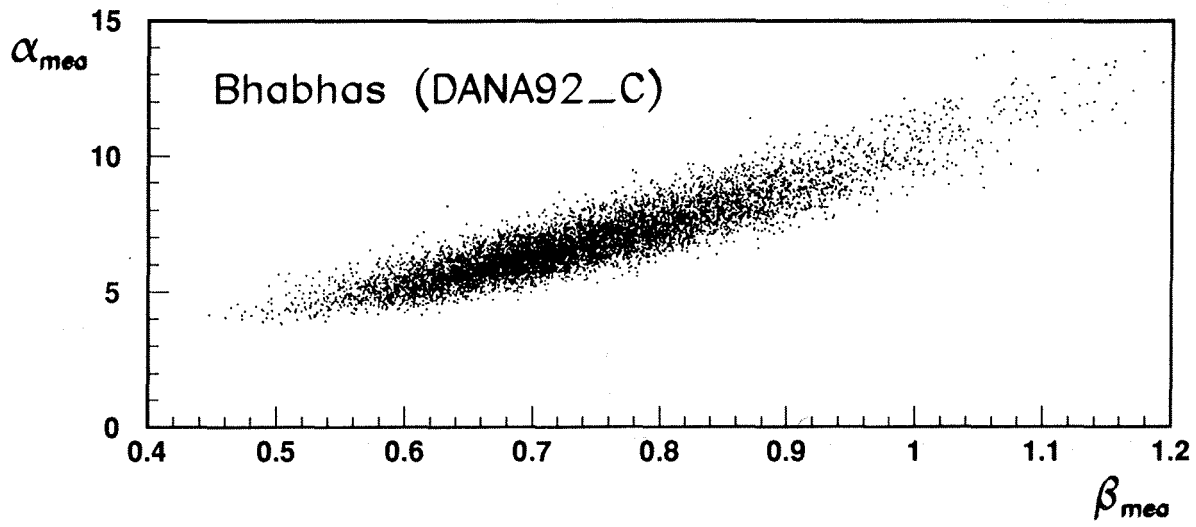

Figure 6.14: *Correlation plot between α_{mea} and β_{mea} for Bhabha data. The plot shows the correlation only in the inner ring.*

Figure 6.15 shows V^{mea} and W^{mea} to be nearly Gaussian distributed and uncorrelated. In addition, it can easily be shown by differentiating the Γ-distribution that V^{mea} corresponds to the reciprocal of t_{max}, where t_{max} denotes the shower position in radiation lengths of the distribution maximum.

$$t_{max} = \frac{1}{V^{mea}} \tag{6.30}$$

Instead of including the information on α and β in the χ^2 definition, we now include the information on V and W. Therefore, instead of parametrizing the mean values and standard deviations of α_{mea} and β_{mea} as a function of energy, we now perform this procedure for V^{mea} and W^{mea}. For this purpose we generated single electron Monte Carlos at the energies 2.5 GeV, 5 GeV, 10 GeV, 20 GeV, 30 GeV and 45 GeV (see section 6.1.1). The measured mean values V^M and W^M and their corresponding standard deviations σ_V and σ_W together with a logarithmic fit function are shown in Figure 6.16. The data have been fitted using a logarithmic function of the form

$$f(E) = \frac{1}{A + B \ln E} \ . \tag{6.31}$$

Table 6.1 lists the parameters A and B which results from the fit of the function $f(E)$ on the Monte Carlo data.

In addition, the standard deviations σ_{E_i} of the nine layers need to be parametrized as a function of energy. Therefore, the function of the form

$$f(E) = C \cdot E^D \tag{6.32}$$

was used. The resulting parameters C and D are listed in Table 6.2.

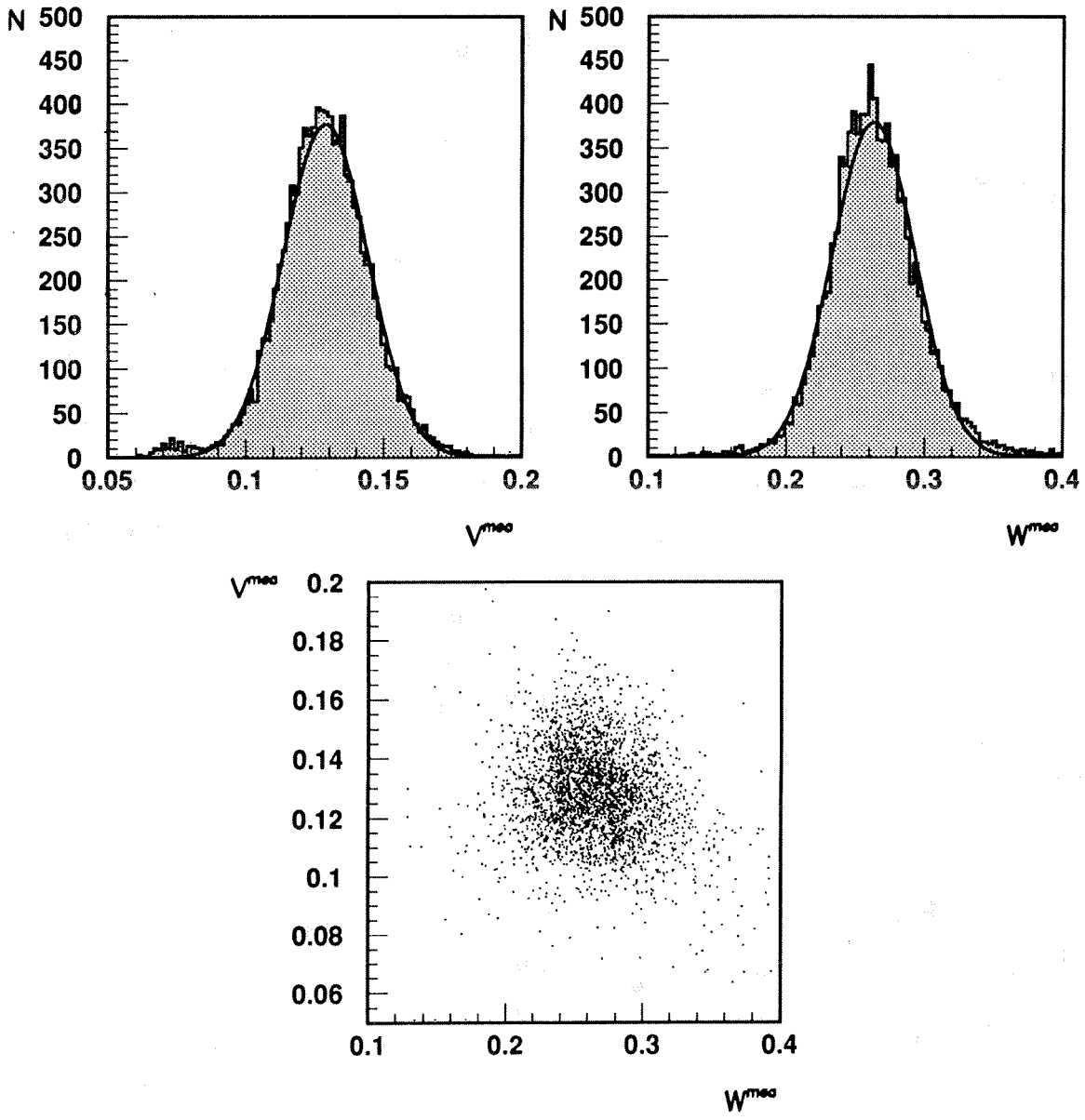

Figure 6.15: *V^{mea} and W^{mea} for Bhabhas (DANA92_C) in the inner ring. It is evident that they are nearly Gaussian distributed and uncorrelated.*

6.3.3 Fitting θ–Cracks

The model for the parametrization of longitudinal shower shapes previously described is valid only in non-crack regions. A recovery of ϕ-cracks is nearly impossible because of their pointing geometry. Photons and for example 45 *GeV* Bhabhas in a ϕ-crack of the HPC deposit almost no energy. Only very low energetic electrons lose some energy in the calorimeter because of their curvature in $R\phi$ direction.

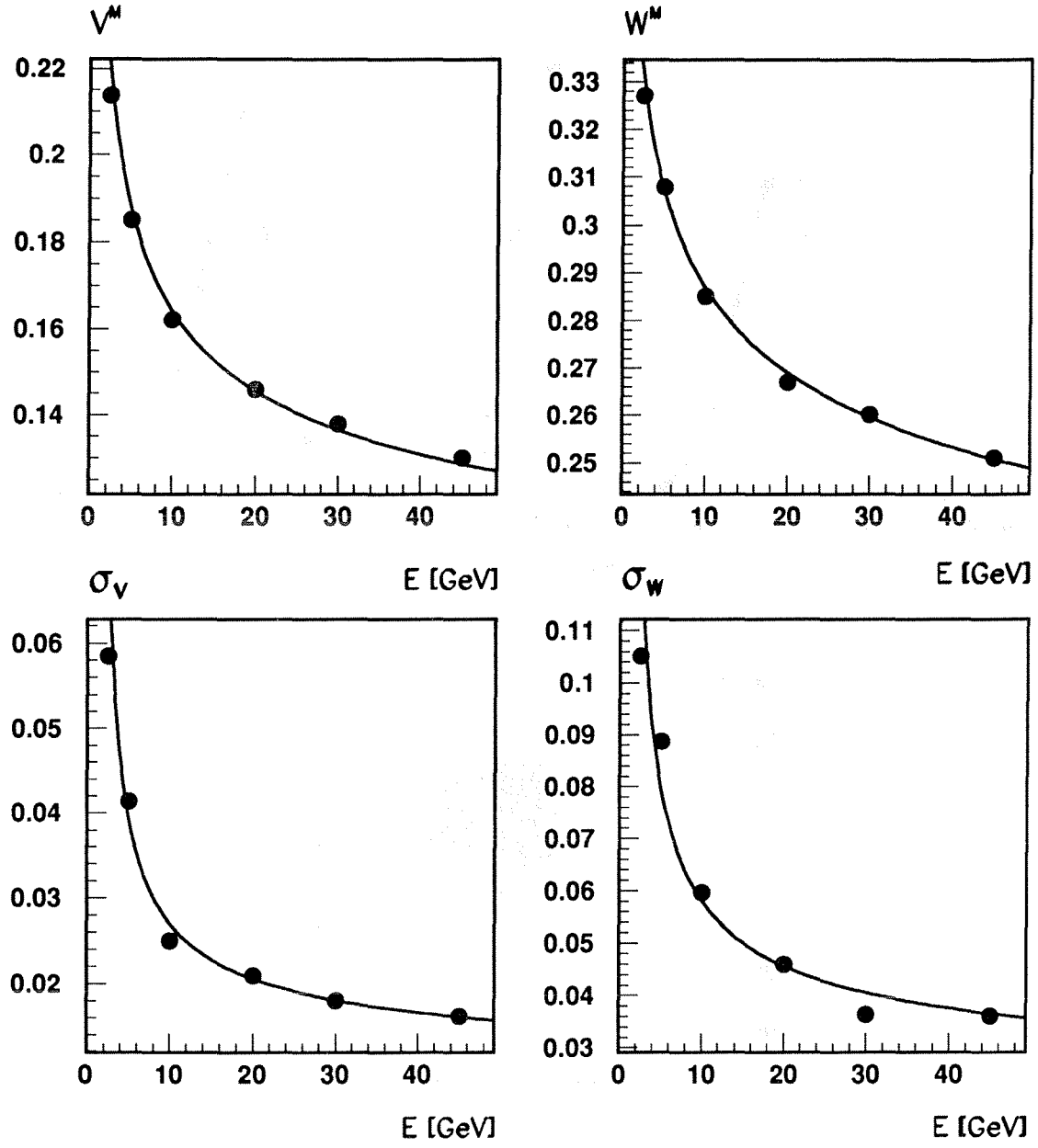

Figure 6.16: *Parametrization of V^M, W^M, σ_V and σ_W as a function of energy*

θ-cracks are much easier to fit. All particles deposit at least a fraction of their energy in the calorimeter, because of their non-pointing geometry. Since we have nearly 35% of the Comptons of 1992 in θ-crack regions, it is worthwhile to develop an algorithm which describes θ-cracks. Figure 6.17 shows some examples for electromagnetic showers in θ-crack regions. In order to fit also θ-cracks our original model needs to be modified in some points.

- The material distribution inside a θ-crack needs to be changed. A lead-weight-function $f(Z)$ is used which is one outside cracks and drops down nearly to zero inside cracks. This

	A	B
V^M	3.519	1.119
W^M	2.711	0.333
σ_V	-1.408	16.730
σ_W	1.638	6.782

Table 6.1: *Parametrization of V^M, W^M, σ_V and σ_W using the function $f(E) = 1/(A + B \ln E)$.*

	C	D
σ_{E_1}	0.115	0.364
σ_{E_2}	0.175	0.480
σ_{E_3}	0.139	0.669
σ_{E_5}	0.129	0.732
σ_{E_6}	0.161	0.595
σ_{E_7}	0.177	0.581
σ_{E_8}	0.060	0.993
σ_{E_9}	0.037	0.966
$\sigma_{E_{10}}$	0.016	1.053

Table 6.2: *Parametrization of σ_{E_i} using the function $f(E) = C + E^D$.*

lead-weight-function $f(Z)$ is multiplied by the change in radiation length Δt per gap so that inside cracks the increment of material is nearly zero.

In order to find a good model for the lead-weight-function $f(Z)$, tests have been done with the real geometry of a crack using step functions at the end of one module and at the beginning of the next module. Better results can be obtained by using two Fermi functions at the crack positions with different *'temperatures'* being used for different layers[12]. For the layers with medium and large pads higher *'temperatures'* were applied, which result in a bigger smearing of the Fermi functions. This procedure is a mean description of the transverse shower shape. Since we have a broader shower in the layers with medium and large pads, we need a broader smearing in the corresponding Fermi functions. Figure 6.18 shows the Fermi functions $f_1(Z)$ – $f_3(Z)$ which were used for layers with small, medium and large pads.

- One needs to consider a sensitivity effect in θ-cracks. Since the HPC is blind inside cracks we use again two Fermi functions to describe this effect. The used function $f_4(Z)$ is shown in Figure 6.18.

- In order to get a better description of the transverse shower shape, one can use three tracks instead of one to step through the HPC. Figure 6.19 describes this method. Normally, the opening angle and the different weights between the tracks need to be parametrized as a function of energy. Since the improvement is only visible in crack regions, one can work with an average value of 3° opening angle and the weights 20%, 60% and 20%. The procedure brings improvements especially in crack regions but takes a factor of three more CPU time.

6.3.4 Definition of the χ^2

The previous sections described the parametrization of longitudinal shower profiles using the Γ-distribution. A model for the material distribution was derived and an energy parametriza-

[12]The Fermi function used are of the type $f(Z) = 1/(e^{A\cdot(Z-Z_0+B)} + 1)$, with $Z_0 = 92.4cm$ $(183.0cm)$ for the first (second) θ-crack. The constants A and B are tuned layer-dependent in order to achieve best recovery.

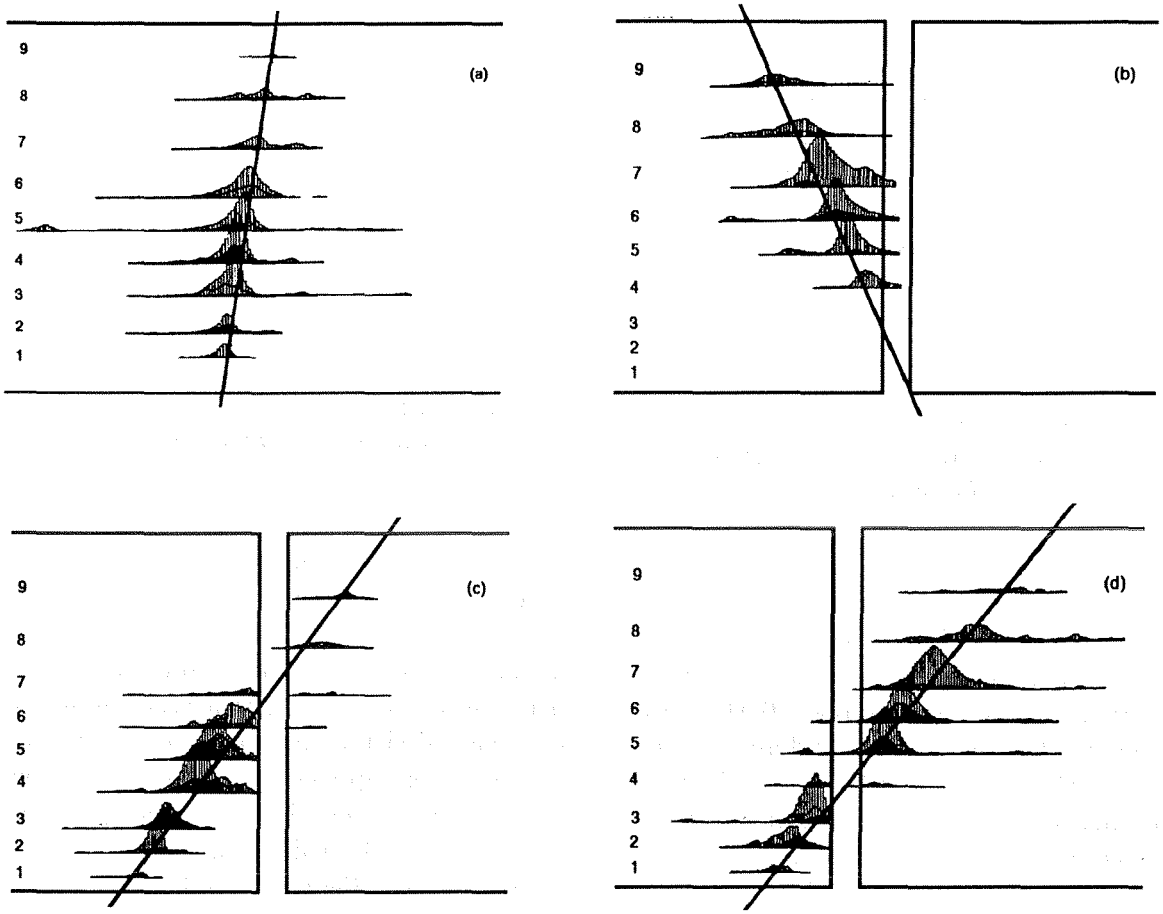

Figure 6.17: *Some examples for electromagnetic showers in crack regions. Figure (a) shows a normal shower in the HPC. In figure (b) the first three layers are lost due to the crack. Figure (c) shows the loss of the last three layers and in figure (d) the loss of the middle layers is visible. The graphics was obtained using the program package IGHPC [54].*

tion of the main parameter was explained. Using all the information, we define our χ^2 in the following way:

$$\chi^2 = \sum_{i=1,i\neq 4}^{10} \frac{(E_i^{\Gamma} - E_i^{mea})^2}{\sigma_{E_i}^2} + \frac{(V^M - V)^2}{\sigma_V^2} + \frac{(W^M - W)^2}{\sigma_W^2} \tag{6.33}$$

The three parameter for the fit are V, W and the shower energy E which is implicitely included in all contributing terms. In total, we have eleven contributions to the χ^2; nine contributions from the layer energies and two from V and W. The nine measured parameters E_i^{mea} lead with the two constraints $V = V(E)$, $W = W(E)$ and the three fit parameter E, V and W to eight degrees of freedom. It is interesting to realize that for this fit only measured values from the HPC are used. The fit is independent of the track momentum p_{track}.

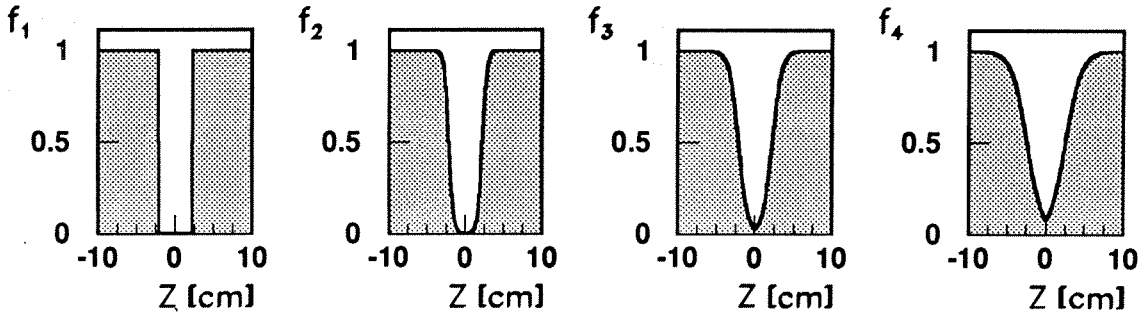

Figure 6.18: *Model of two Fermi functions describing a θ-crack. $f_1(Z)$, $f_2(Z)$ and $f_3(Z)$ denote the used functions for the changed material distribution in layers with small, medium and large pads ($Z_0 = 0$). The sensitivity effect is considered by using function $f_4(Z)$.*

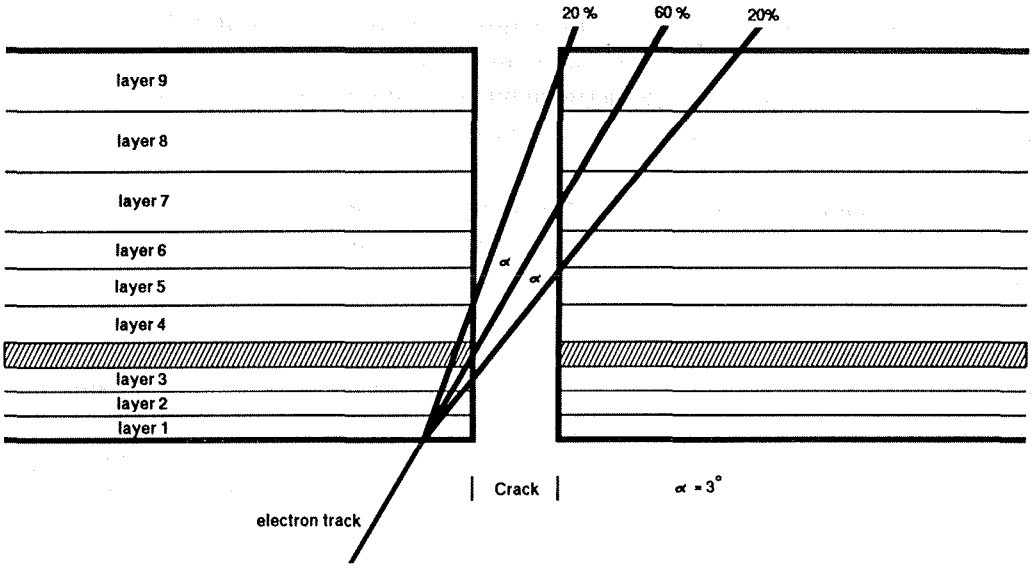

Figure 6.19: *Improved Model for θ-cracks. Usage of three tracks instead of one to step through a crack with an opening angle of* 3° *and the weights* 20%, 60% *and* 20%.

In the first approach the standard deviations for the two parameters V and W and the layer energies E_i were evaluated from the measured distributions. In this treatment all shower fluctuations contribute to the width of the distributions. Since we want to exclude these fluctuations from our model, we need to decrease the standard deviations in a way that afterwards the pulls[13] of the eleven contributions to the χ^2 are centered around zero with a width of one. This was done in an iterative procedure where different scale factors for the eleven contributions were obtained using single electron Monte Carlos. The energy dependence of the σ's

[13]The pull is defined as the difference between measured and expected value divided by σ.

was not changed in that way. The final fine tuning was done by using real data electrons from Tau, Compton and Bhabha events. The widths of the pulls were found for different energies and for all eleven contributions to be at one within an error of 20%.

Theoretically, the shape of a χ^2 distribution for a problem with n degrees of freedom is described by the following equation:

$$f(z,n) = \frac{1}{2^{n/2}\Gamma(n/2)} z^{n/2-1} e^{-z/2} \tag{6.34}$$

The expectation value $M(z)$ and variance $V(z)$ are given by:

$$M(z) = n \qquad V(z) = 2n \tag{6.35}$$

The maximum position of the χ^2 distribution lies for a problem with n=8 degrees of freedom at six. Figure 6.20 shows the comparison of the χ^2 distributions between data and Monte Carlo for different data samples. The first picture reveals a reasonable agreement between data and Monte Carlo for 1992 Bhabhas (DANA92_C). The maximum position is centered at six. An even better agreement was found for Comptons of 1991 (DELANA_E) and Comptons of 1992 (DANA92_C). Since there was no Compton Monte Carlo available, the single electron Monte Carlos were used, whereby the momentum and the $\cos\theta$ spectra were corrected to the measured Compton spectra. The agreement for τ data and Monte Carlo with much less statistics is shown in the last picture to be very good.

It is essential for a good fit to have a χ^2 distribution independent of the energy. Figure 6.20 shows in a scatter plot the dependence of the χ^2 on the measured energy in the HPC for single electron Monte Carlos (DANA92_C). It is visible that the maximum of the χ^2 distribution remains at six down to energies as low as 1 GeV.

Since we have a complicated system in a multi-dimensional space and an even more difficult situation in crack regions, we do not expect to get a perfect agreement with a χ^2-distribution. Another weakness of the model is that we assume all layer energies to be Gaussian distributed. This assumption is good for highly energetic showers for layers with large energy deposition. Especially in the first and last layers, this assumption is often very crude, but since we have eleven contributions to the χ^2, the model is expected to work[14]. In order to study the deviation from a χ^2-distribution and to have a tool for the fine tuning of the parameters we convert the χ^2-distribution in a probability distribution.

$$Prob(\chi^2) = \int_{\chi^2}^{\infty} f(z,n)dz \tag{6.36}$$

Instead of having a χ^2 for the electron hypothesis, we are now left with a probability which is distributed between 0 and 1. In the case of a perfect χ^2-distribution, we expect the probability distribution to be flat. Figure 6.21 shows the probability distribution for the four described data samples. It can be seen that, except for the peak in the beginning, the distributions are very flat between 0 and 1. The peak in the beginning results from fits with increased χ^2. Parts of the peak can be explained by the θ crack region, which cannot be as good as non crack regions. In order to compensate for the peak in the beginning and to bring the mean value near to 0.5, the parameters were tuned in a such way to have a small rise to higher probabilities.

[14] Some addional information can be found in section 6.5.

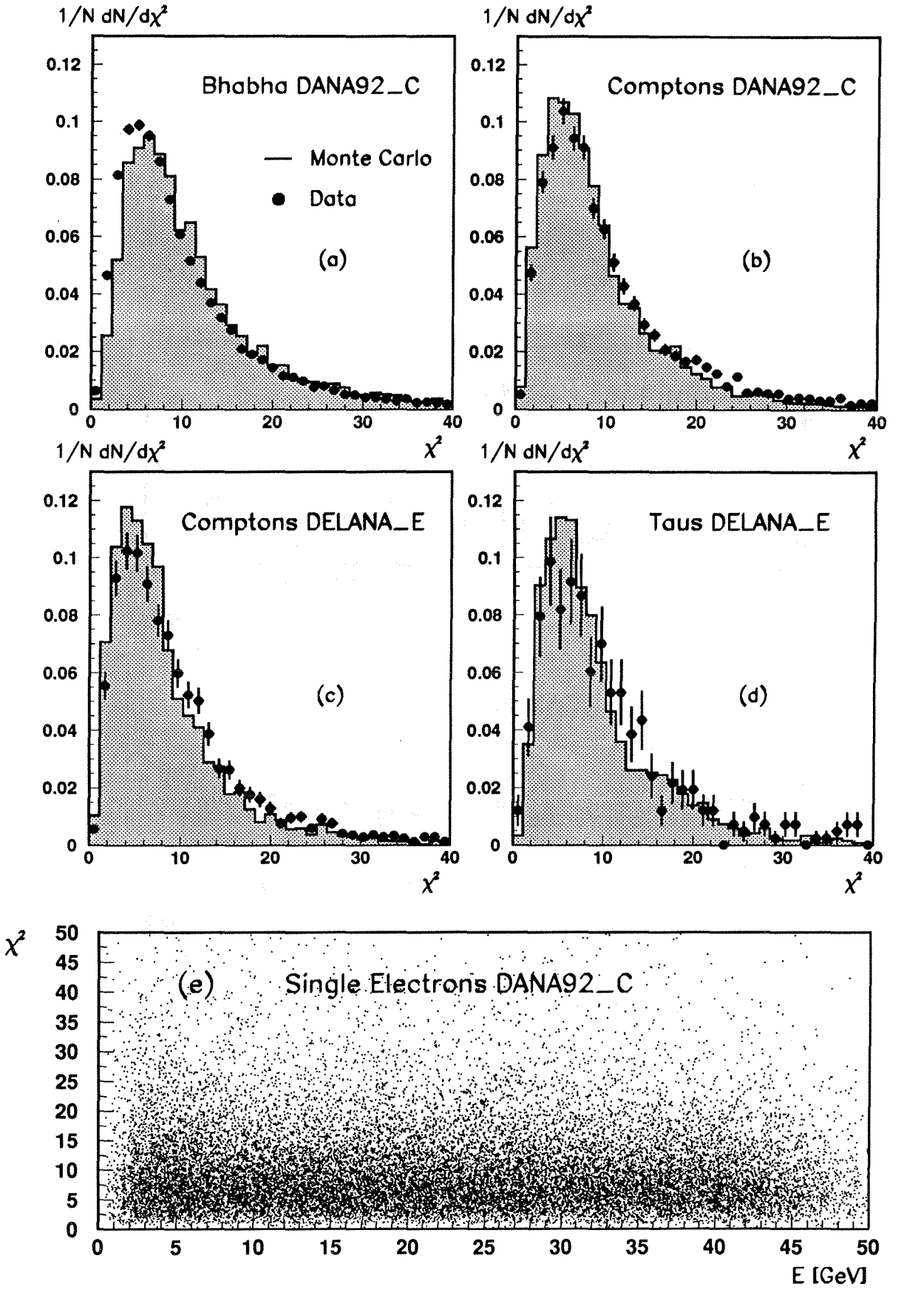

Figure 6.20: *Comparison of the χ^2 distributions between data and Monte Carlo for different data samples (Histograms (a)-(d)). The lower plot (e) shows the dependence of the χ^2 on the measured energy for single electron Monte Carlo.*

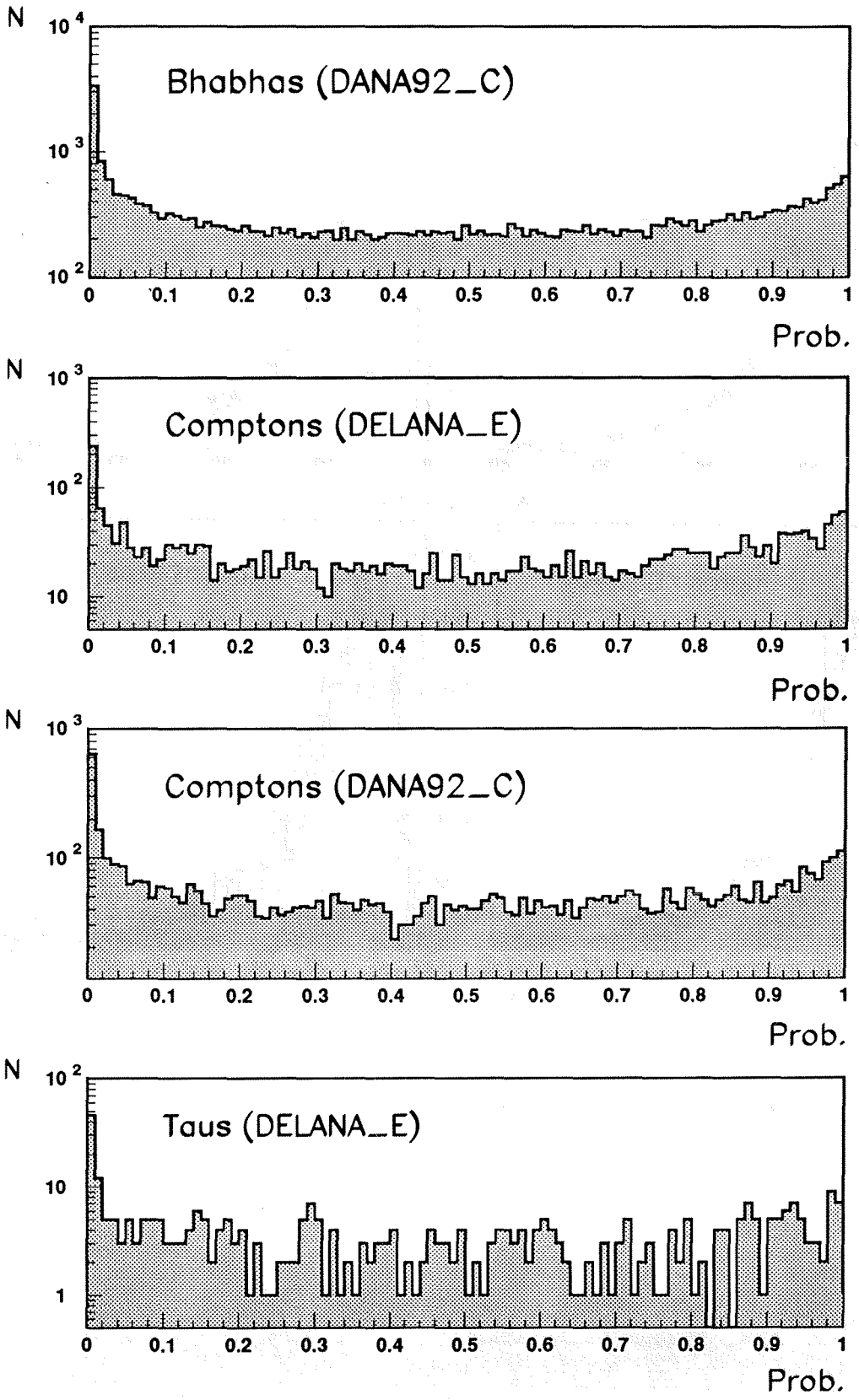

Figure 6.21: *Probability distributions for Bhabha (DANA92_C), Compton (DELANA_E and DANA92_C) and Tau (DELANA_E) events.*

6.3.5 Results from the Shower Fit in Crack Regions

In this section, some important results of the shower fit in crack regions will be discussed. Figure 6.22 shows some examples for the shower fit in crack regions. The abscissa denotes the 50 drift gaps while the ordinate corresponds to the deposited energy for the different drift gaps in GeV. These example showers were taken from Bhabha Monte Carlo and correspond to the cases shown in Figure 6.17. The first plot shows a shower with full containment in the

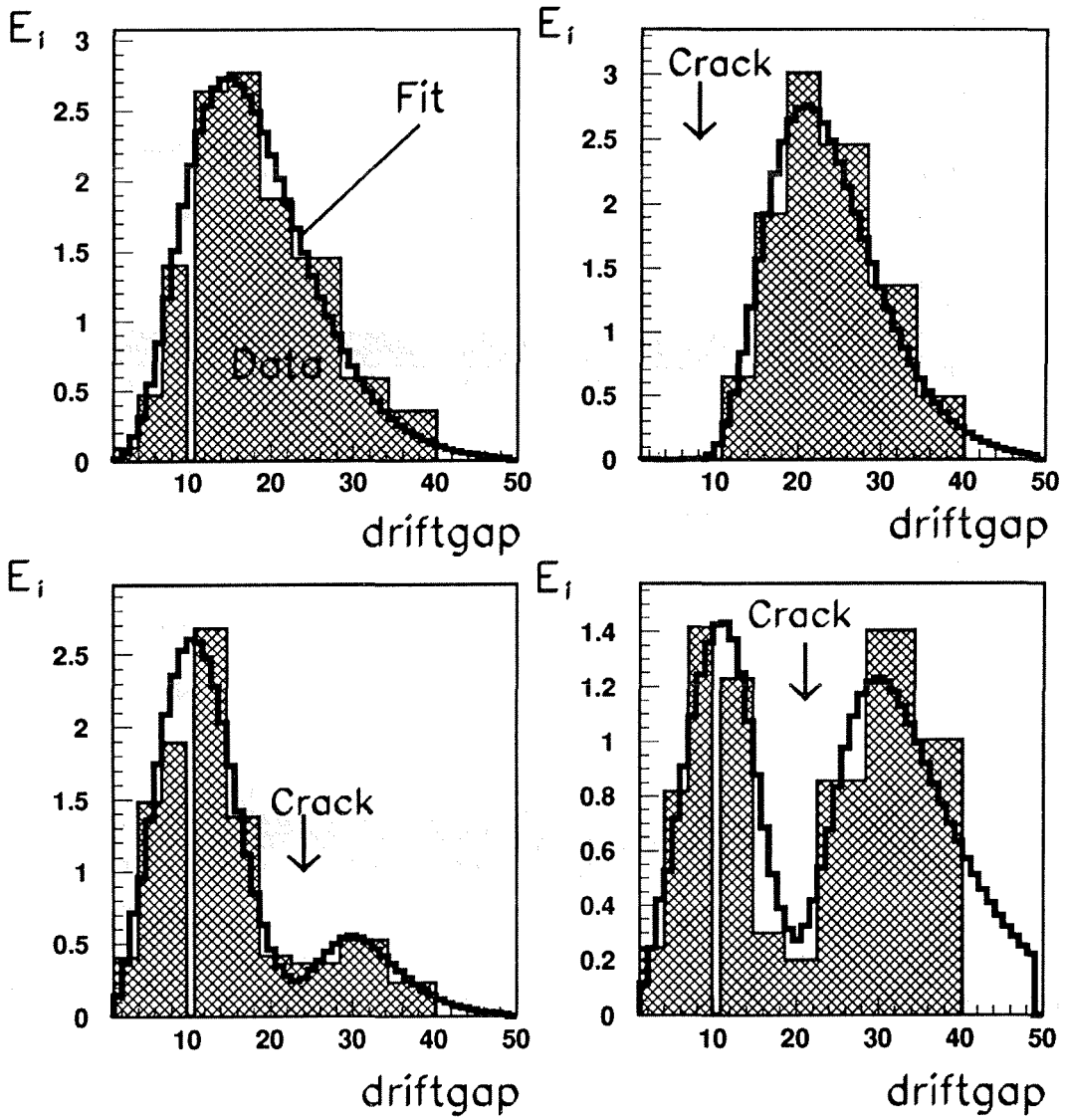

Figure 6.22: *Some examples of the shower fit in crack regions. The abscissa corresponds to the 50 drift gaps while the ordinate denotes the deposited energy for the different drift gaps in GeV. The examples correspond to the different cases shown in Figure 6.17.*

HPC. The next three histograms show some losses due to cracks and their recovery with the shower fit.

In order to study the recovery in crack regions it is enlightening to plot the χ^2 distribution versus $\cos\theta$. Without any special treatment in crack regions, a drastic rise in χ^2 is visible around the two crack positions at $\cos\theta = 0.39$ and 0.64. Using the described procedure in crack regions the χ^2 distribution is almost flat. Figure 6.23 shows the χ^2 distributions for Comptons DELANA_E and DANA92_C. The crack positions are marked with arrows and disappeared almost completely in the χ^2 distribution. A more quantitative picture of the

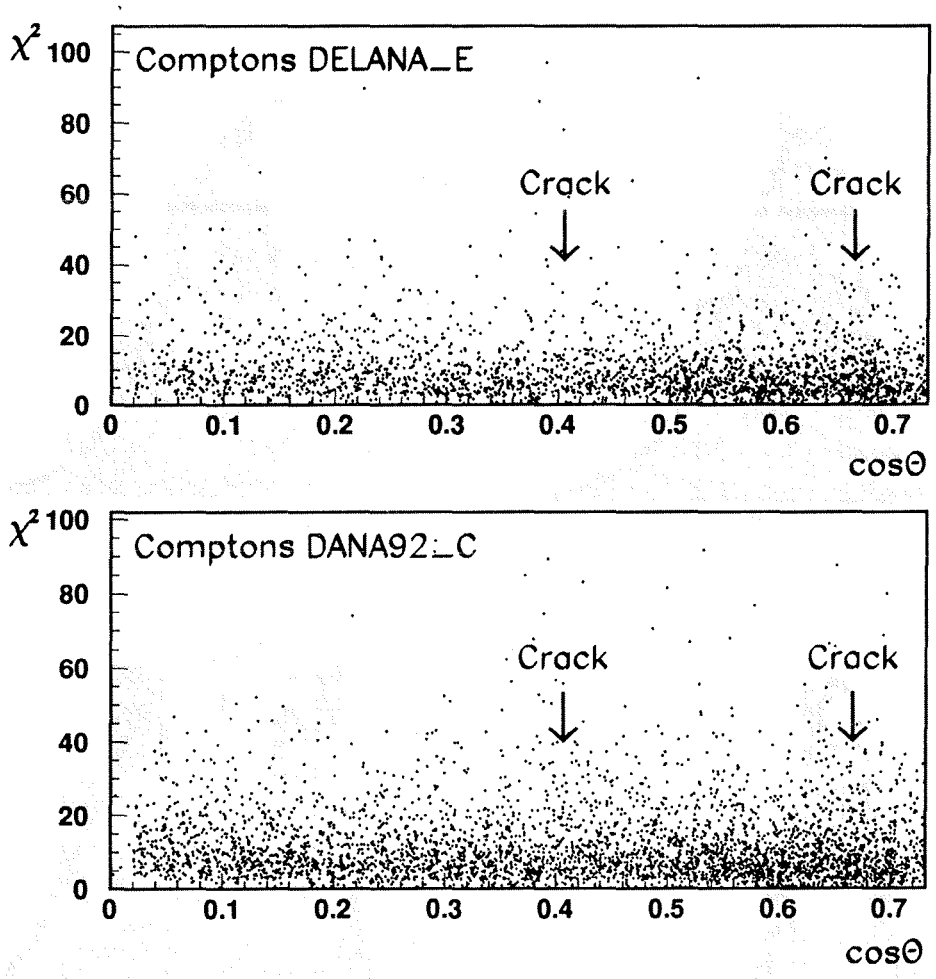

Figure 6.23: *χ^2 distribution versus $\cos\theta$ for Compton data (DELANA_E and DANA92_C). The two crack positions are marked with arrows.*

recovery in crack regions can be obtained by plotting the $\cos\theta$ distribution for probabilities lower than 1% and probabilities greater than 1%. Fits with high χ^2 should appear in the first plot. In case of any degradation due to cracks, we should see peaks at the two crack positions in this plot. In the plot with probabilities greater than 1% one should see a drop around the crack positions. Figure 6.24 shows these two distributions for 1992 Comptons (DANA92_C). The crack positions are marked with arrows again. A degradation due to cracks is hardly visible. Note that the crack at $\cos\theta = 0.64$ is recovered nearly perfectly.

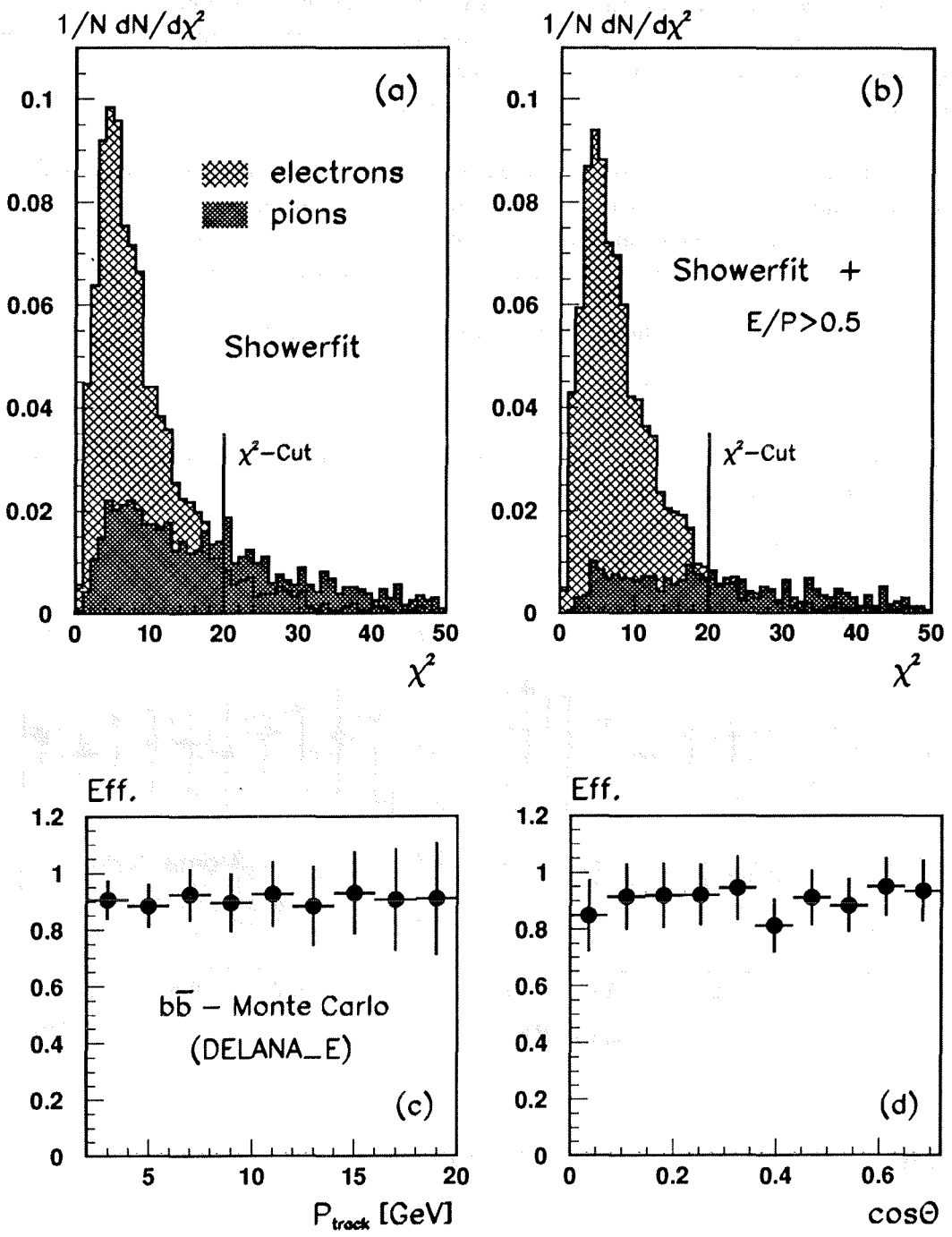

Figure 6.27: *Efficiencies for $b\bar{b}$–Monte Carlo (DELANA_E). The plots (a) and (b) show the χ^2 distributions for electrons and pions with and without the E/p-cut. Histograms (c) and (d) show the obtained efficiencies without E/p-cut for a χ^2-cut at 20 as a function of momentum and* $\cos\theta$.

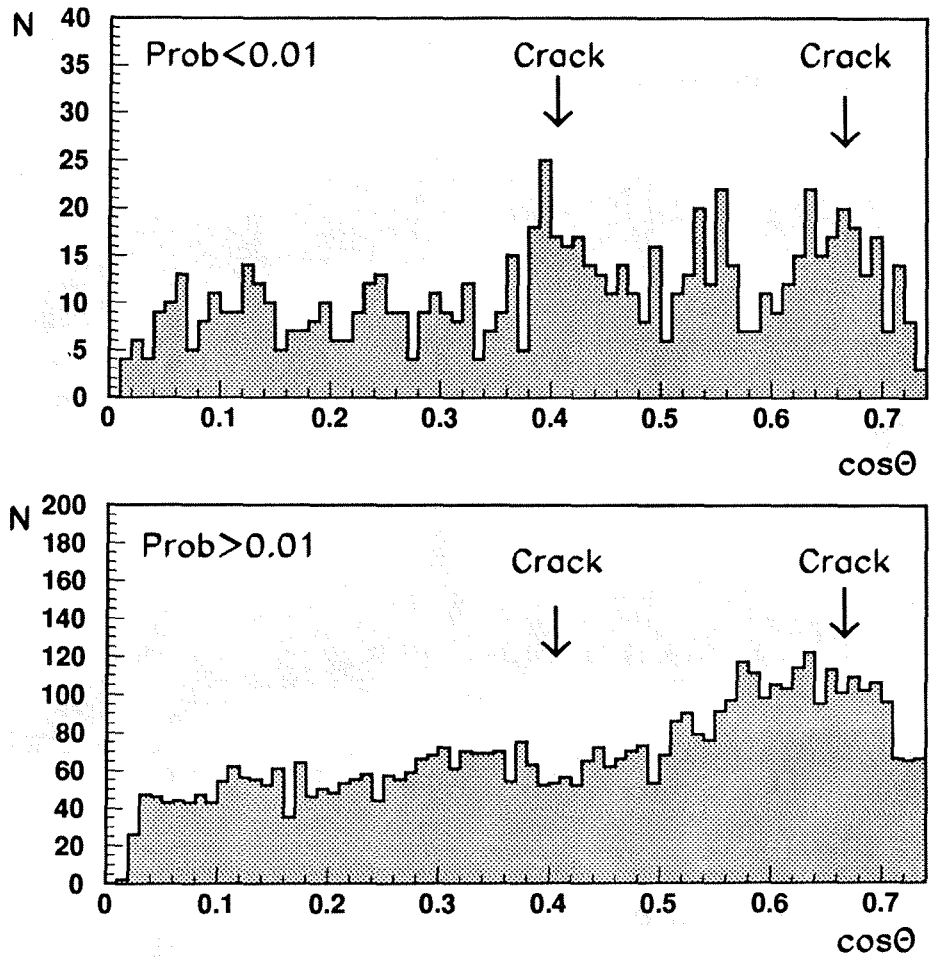

Figure 6.24: *$\cos\theta$-distribution for probability > 1% and < 1% for Compton data (DANA92_C). A degradation due to cracks is hardly visible.*

An energy correction in θ-cracks can only work if the model describes the energy distributions in the nine layers with a precise accuracy. In this case, the fit parameter E can go up and lead to a significant energy correction in cracks. The agreement of the nine layer energies from the measurement and the fit is very good. As an example, Figure 6.25 (histograms (a) and (b)) shows a comparison between the measured and fitted energy distributions in layer 8 versus $\cos\theta$. The plots were produced for real Bhabha data (DANA92_C). The complicated structure, which is just the result of a geometrical effect, is well reproduced by the fit. In case of such an agreement the χ^2 is small even in the near of θ-cracks.

Since one of the fit parameters is the total energy, the shower fit can be used to provide a corrected energy in crack regions. Figure 6.25 (plots (c) and (d)) also shows a comparison of the $\cos\theta$ distributions of measured and fitted energies for Bhabha Monte Carlo (DELANA_E). An improvement in crack regions is clearly visible. The measured energy in the crack at $\cos\theta = 0.39$ drops down to 30 GeV. After the fit the minimal energy lies around 40 GeV.

Another example which demonstrates the power of the shower fit in crack regions is given by Figure 6.26. The cracks are clearly visible in the two parameters V and W measured by the moments. After the fit the two crack positions disappeared.

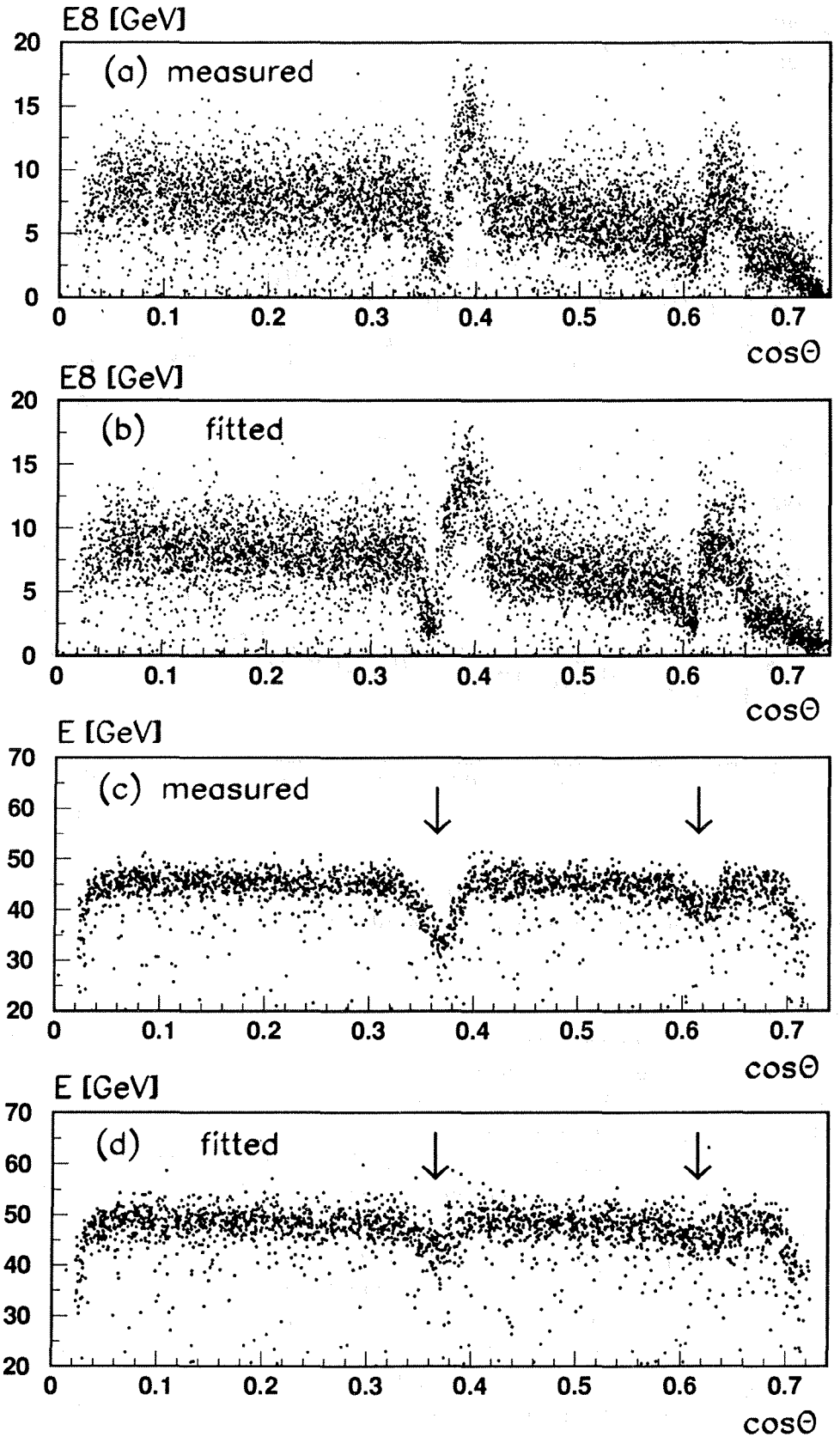

Figure 6.25: *The histograms (a) and (b) compare measured and fitted energies in layer 8 versus* $\cos\theta$ *for Bhabha data (DANA92_C). The fit parameter energy is displayed in the plots (c) and (d) as a function of* $\cos\theta$ *for Bhabha Monte Carlo (DELANA_E).*

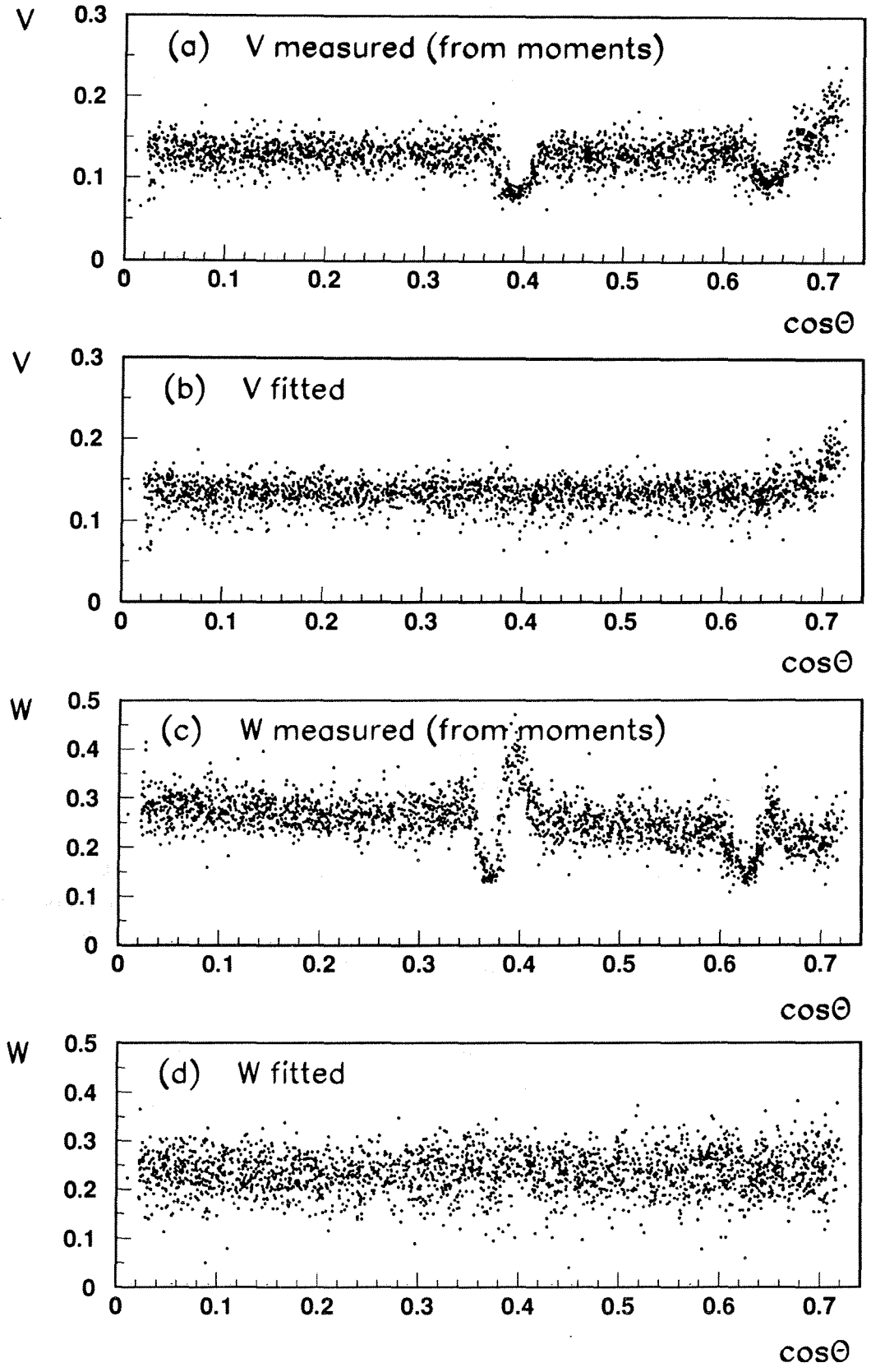

Figure 6.26: *Comparison between measured and fitted parameter V and W for Bhabha Monte Carlo (DELANA_E).*

6.3.6 Efficiencies of the Longitudinal Shower Fit for Electron Identification

In order to calculate efficiencies of the longitudinal shower fit for electron identification, we study the behaviour of $b\bar{b}$–Monte Carlo (DELANA_E). 2650 Events were generated, where one b-quark was forced to decay under weak interaction producing an electron.

$$\begin{aligned} Z^0 &\rightarrow b\bar{b} \\ b &\rightarrow Xe\nu \end{aligned}$$

Application of the cut

$$2.0\ GeV/c < p < 45\ GeV/c \text{ and } |\cos\theta| < 0.72$$

results in:

Pions:	Electrons:
10000	1800

From these particles we demand at least 0.5 GeV in the HPC to perform a fit. ϕ-cracks are excluded from all these calculations. After this cuts we are left with:

Pions:	Electrons:
2300	1500

Notice that before performing a shower fit the efficiency drops down to 83%, which can be explained by the fact that due to interaction with material and threshold effects, the electrons have no shower in the HPC. Of the pions, nearly 77% have been rejected just by demanding 0.5 GeV in the HPC. Since we want to determine the efficiency of the shower fit without any other tools, we take the 2300 pions and 1500 electrons as an input. One has to keep in mind that the obtained values are only valid after this energy cut at 0.5 GeV. The numbers would look much better for the shower fit without this energy cut, but the quoted numbers have more practical use. The momentum spectrum from the 1500 electrons peaks around 4 GeV.

Histogram (a) of Figure 6.27 shows the χ^2 distributions for the remaining electrons and the pions. The histograms are normalized to the total number of entries. For electrons, we have the expected maximum peak position at six. The pions produce a broad distribution between 0 and 50. For more than 50% of the pions the fit does not work, so that they were definitely identified as pions. If one applies now a cut, at for example 20 in the χ^2 distributions, we will get an additional rejection of pions, while most of the electrons will be retained. Plot (b) of Figure 6.27 shows the χ^2 distributions for the shower fit if one applies an additional E/p-cut at 0.5. In order to evaluate efficiencies for the shower fit we work with an χ^2-cut at 20. For the $b\bar{b}$–sample we get an overall efficiency (without E/p-cut) of:

$$\text{Efficiency}(b\bar{b} - \text{M.C.}) = (90 \pm 2)\ \%$$

From the 2300 pions (30 ± 1) % could pass the cut. Compared to the 10000 initial pions we are left now with roughly (7 ± 0.3) %.

The histograms (c) and (d) of Figure 6.27 show the evaluated efficiencies as a function of momentum and $\cos\theta$. One can see that the shower fit is very efficient down to energies around 2 GeV. The efficiency stays nearly constant independent of the energy. The dependence on $\cos\theta$ shows very good agreement with the expected behaviour. In the region of the 90° crack, and at the first crack, the efficiency drops down by roughly 7.5%.

In the following, some comparisons between data and Monte Carlo will be presented. For the electron channel of the Taus the following overall efficiencies were obtained for data and Monte Carlo. A track momentum of greater than 2 GeV was demanded as well as a minimal deposition of 0.5 GeV in the HPC. With the cuts described in section 6.1.4 we found:

$$\text{Efficiency}(\tau - \text{M.C.}) = (89 \pm 2)\ \%$$

$$\text{Efficiency}(\tau - \text{Data}) = (83 \pm 4)\ \%$$

A comparison between data and Monte Carlo for the dependence of the efficiency on momentum and $\cos\theta$ is shown in Figure 6.28.

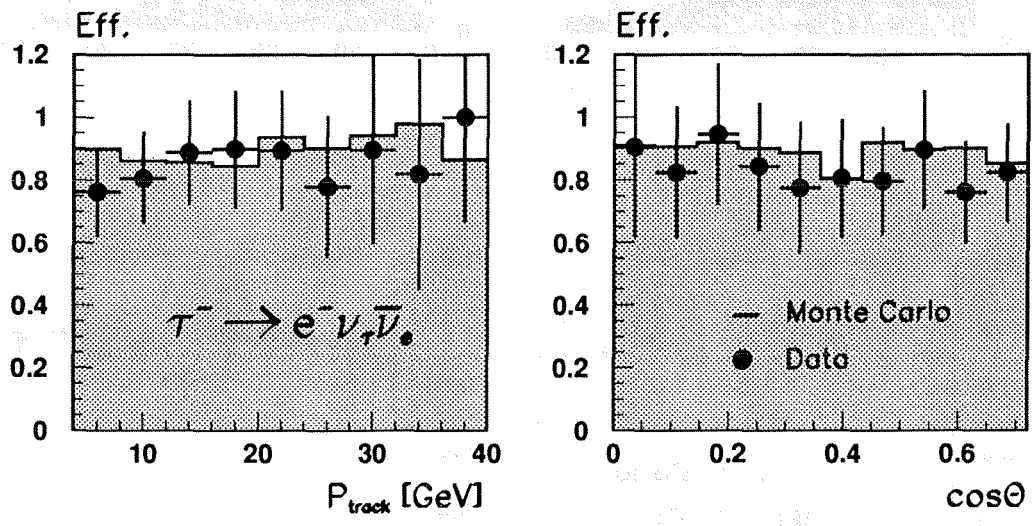

Figure 6.28: *Efficiencies for Taus (DELANA_E) as a function of momentum and cosθ*

For Comptons 1991 and Comptons 1992 a similar analysis was obtained. The results for the overall efficiencies are quoted here:

DELANA_E:

$$\text{Efficiency}(\text{Compton} - \text{M.C.}) = (91 \pm 0.5)\ \%$$

$$\text{Efficiency}(\text{Compton} - \text{Data}) = (88 \pm 2.0)\ \%$$

DANA92_C:

$$\text{Efficiency(Compton - M.C.)} = (90 \pm 0.5)\ \%$$

$$\text{Efficiency(Compton - Data)} = (86 \pm 1.3)\ \%$$

A comparison between data and Monte Carlo for the dependence of the efficiency on momentum and $\cos\theta$ is shown in Figure 6.29.

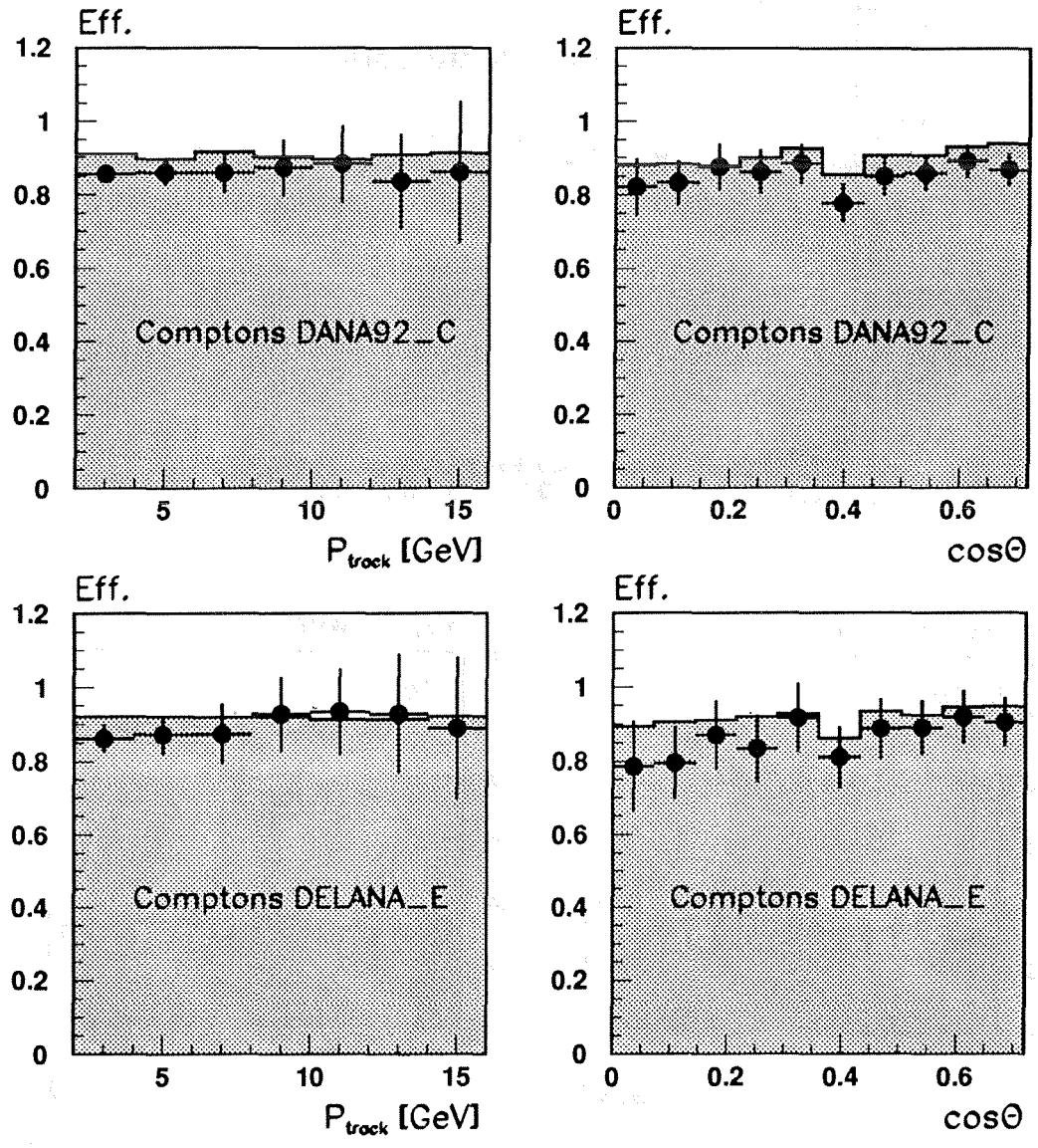

Figure 6.29: *Efficiencies for Comptons as a function of momentum and cosθ (DELANA_E and DANA92_C)*

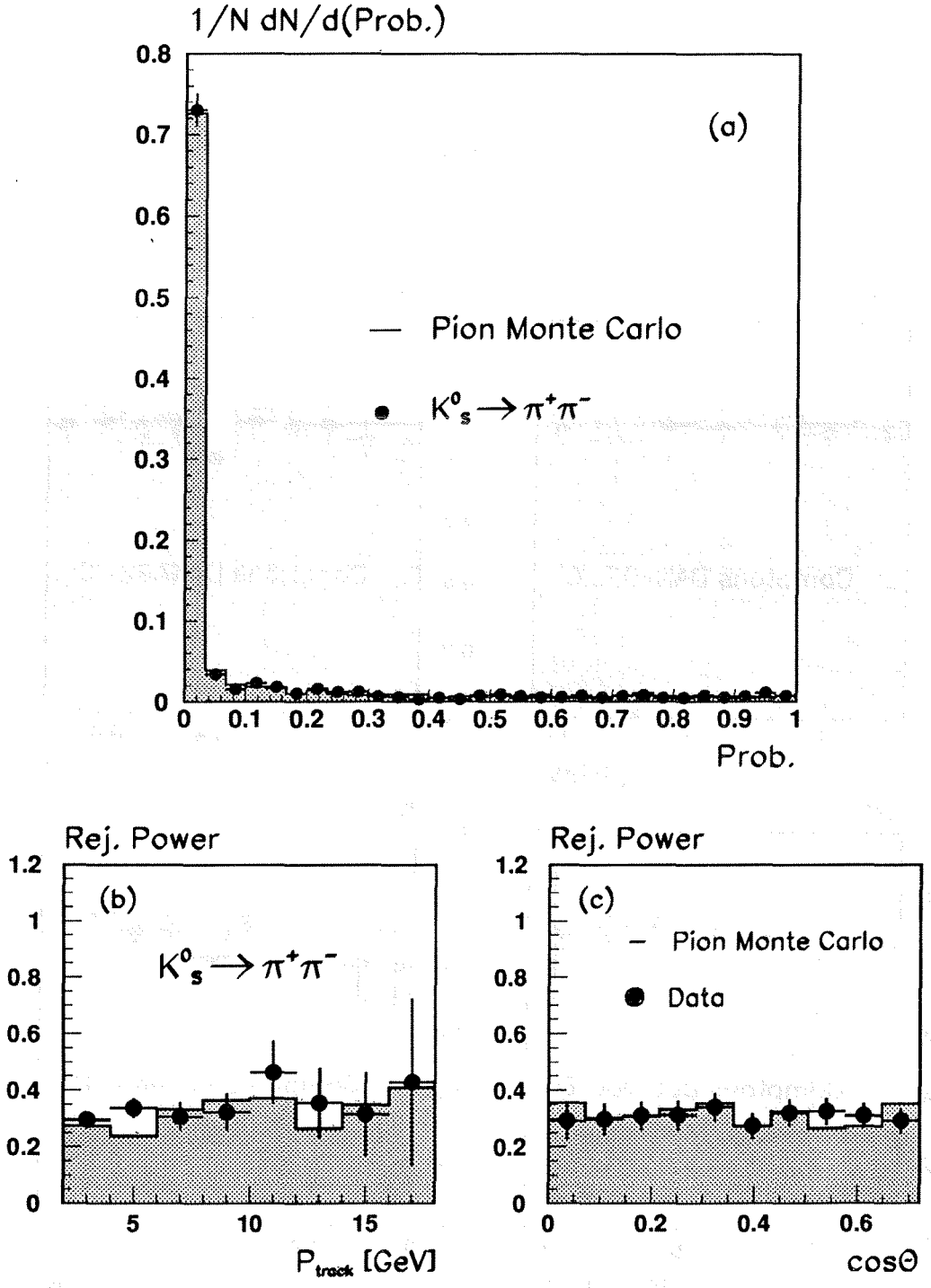

Figure 6.30: *Histogram (a) shows a comparison between the normalized probability distribution of pions from K^0_S (DANA92_C) events and single pion Monte Carlo (DELANA_E). The momentum and $\cos\theta$ spectra of the Monte Carlo were corrected to the spectra of the data. The plots (b) and (c) show the percentage of pions passing a χ^2-cut at 20 as a function of momentum and $\cos\theta$. One has to keep in mind that this numbers are only valid for the special pion sample with $E_{HPC} > 0.5GeV$ and $P_{track} > 2GeV$. Neglecting the energy cut $E_{HPC} > 0.5GeV$ would lead to the passage of roughly 7% of the pions.*

In histogram (a) of Figure 6.30 a comparison between the normalized probability distributions for pions from K^0_S events (DANA92_C) and single pion Monte Carlo (DELANA_E) is made. Since there was no Monte Carlo data for DANA92_C available, the comparison was made using DELANA_E Monte Carlo. Since the thresholds for 1991 Monte Carlos are very near to the 1992 values, this should be a good approximation. For most of the pions the fit does not work, so that they are definitively identified as pions. These pions are visible in the first bin of the plot. As it can be seen, the agreement between data and Monte Carlo is very good. The plots (b) and (c) in Figure 6.30 show the fraction of pions passing a cut in χ^2 at 20 as a function of energy and $cos\theta$. An average value of 31% was found for data and Monte Carlo. One has to keep in mind that these numbers are only valid for the special pion sample with $E_{HPC} > 0.5GeV$ and $P_{track} > 2GeV$. Neglecting the energy cut $E_{HPC} > 0.5GeV$ would lead to the passage of roughly 7% of the pions.

In order to show how to distinguish between pions and electrons in data, Figure 6.31 was included. The electrons are represented by 1992 Comptons. The pions are the decay products of the 1992 K^0_S. The histograms are normalized to the same number of entries including overflows. The agreement between data and Monte Carlo was already shown.

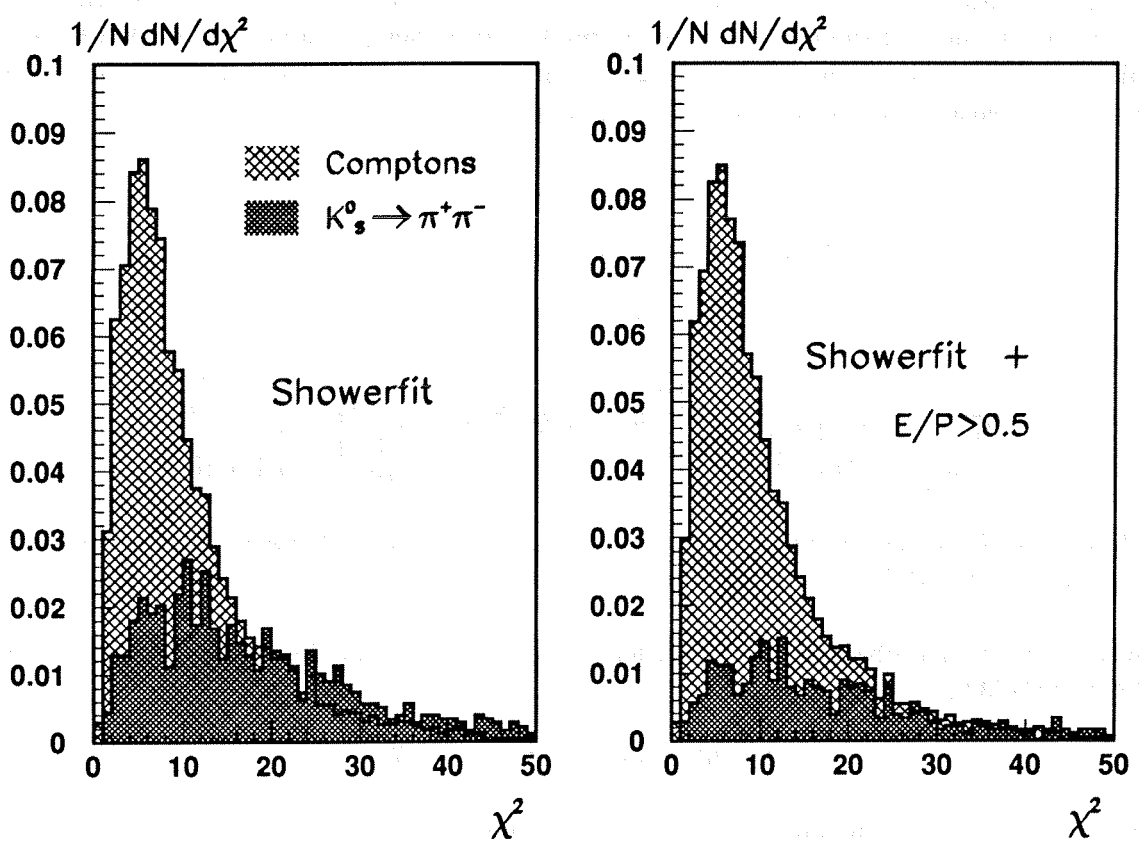

Figure 6.31: *Comparison between pion and electron χ^2 distributions. The electrons are represented by the Comptons (DANA92_C) and the pions by the decay products of the K^0_S (DANA92_C).*

6.4 Results from the Electron Identification

The first version of the electron identification routine[15] consists of five contributions, which were described in previous sections.

- HPC-shower fit
- dE/dx
- E_{HPC}/p_{track}
- Z(extrapolation)–Z(shower)
- ϕ(extrapolation)–ϕ(shower)

For each of the five tools, a probability was separately derived for the electron hypothesis. These probabilities had a nearly flat distribution between 0 and 1. In order to connect all these pieces together, an overall pseudo-probability was calculated.

$$\text{Prob}(e^-) = \text{Prob(sh.-fit)}\cdot\text{Prob}(dE/dx)\cdot\text{Prob}(E/p)\cdot\text{Prob}(\Delta Z)\cdot\text{Prob}(\Delta\phi)$$

Plotting this variable separately for pions and electrons reveals the pions to be concentrated near zero, while most of the electrons are distributed at higher probabilities. Applying a cut in this probability distribution leads to a good separation between electrons and pions. The following efficiencies have been obtained by applying a cut at:

$$\text{Prob}(e^-) < 2 \cdot 10^{-4}$$

The efficiencies have been obtained in the θ regions:

$$45 < \theta < 88 \text{ and } 92 < \theta < 135$$

	$p > 3$ GeV	$p > 4$ GeV	$p > 5$ GeV
$b\bar{b}$–M.C. (DELANA_E)	$(70 \pm 2)\%$	$(73 \pm 2)\%$	$(76 \pm 3)\%$
Compton (DANA92_C)	$(65 \pm 3)\%$	$(67 \pm 3)\%$	$(70 \pm 4)\%$

Table 6.3: *Efficiencies for the electron identification for $b\bar{b}$–MC (DELANA_E) and Compton data (DANA92_C) [32].*

A misidentification probability per track has been obtained from the K^0_S-sample from 1992 (DANA92_C) [32].

$$\text{Mis. Id. Prob.} = (0.2 \pm 0.1)\ \%$$

The rejection power of the different quantities used for the electron identification is shown in Table 6.4. Their rejection power was tested using the K^0_S-signal by excluding separately the tools shower fit, dE/dx, E/p, ΔZ and $\Delta\phi$ from the identification routine. It can be seen that the shower fit and the dE/dx measurement provide the most powerful tools for the electron identification.

[15] The routine ELPROB was provided by the electron identification task group [32].

	All	No shower fit	No dE/dx	No E/p	No ΔZ	No $\Delta\phi$
Mis. Prob.	0.2 %	1.7 %	1.7 %	0.8 %	0.5 %	0.4 %
Reject. Factor	–	8.5	8.5	4.0	2.5	2.0

Table 6.4: *Rejection power of the different quantities used for the electron identification obtained from the K^0_S-signal [32].*

Table 6.5 shows the identification power of the different five tools for the cases of $\pi-\gamma$ overlap, a normal electromagnetic shower initiated from electrons, a hadronic shower and no shower from pions. The symbols ++ and + mean positive identification as an electron, while −− and − denote the capability to reject these particles.

	$\pi-\gamma$ overlap El. mg. Shower	$e^{\pm}$ El. mg. Shower	$\pi^{\pm}$ Hadr. Shower	$\pi^{\pm}$ No Shower
Shower fit	+	++	−	−−
dE/dx	−−	++	−−	−−
E/p	+−	++	−	−−
ΔZ	−−	+	+	−−
$\Delta\phi$	−−	+	+	−−

Table 6.5: *Identification power of the different electron identification tools. The symbols ++ and + denote positive identification, while −− and − describe the capability to reject the particle.*

6.5 Longitudinal Shower Fluctuations

In this section a method is described for obtaining a better understanding of longitudinal shower fluctuations. We will describe a useful tool for obtaining the main shower fluctuations, which is needed for a successful parametrization of shower profiles. This tool can also be used to study differences in the shower development between real showers and Monte Carlo simulations.

Figure 6.32 shows the energy depositions for the 5 *GeV* Monte Carlo electron showers in the nine layers of the HPC. In order to make the sampling fluctuations clearly visible, this Monte Carlo was generated without material in front of the HPC and an injection angle of 90°. It is clear that the energies in the single layers are non Gaussian. This is especially true in the first layers, where the shower development starts, and in the last layers, where the energy deposition is small. In addition, the energy depositions in the layers are correlated which denotes the fact that one main shower fluctuation is the displacement of the whole shower along the shower axis. These effects are worse for low energetic showers. For 45 *GeV* Bhabhas,

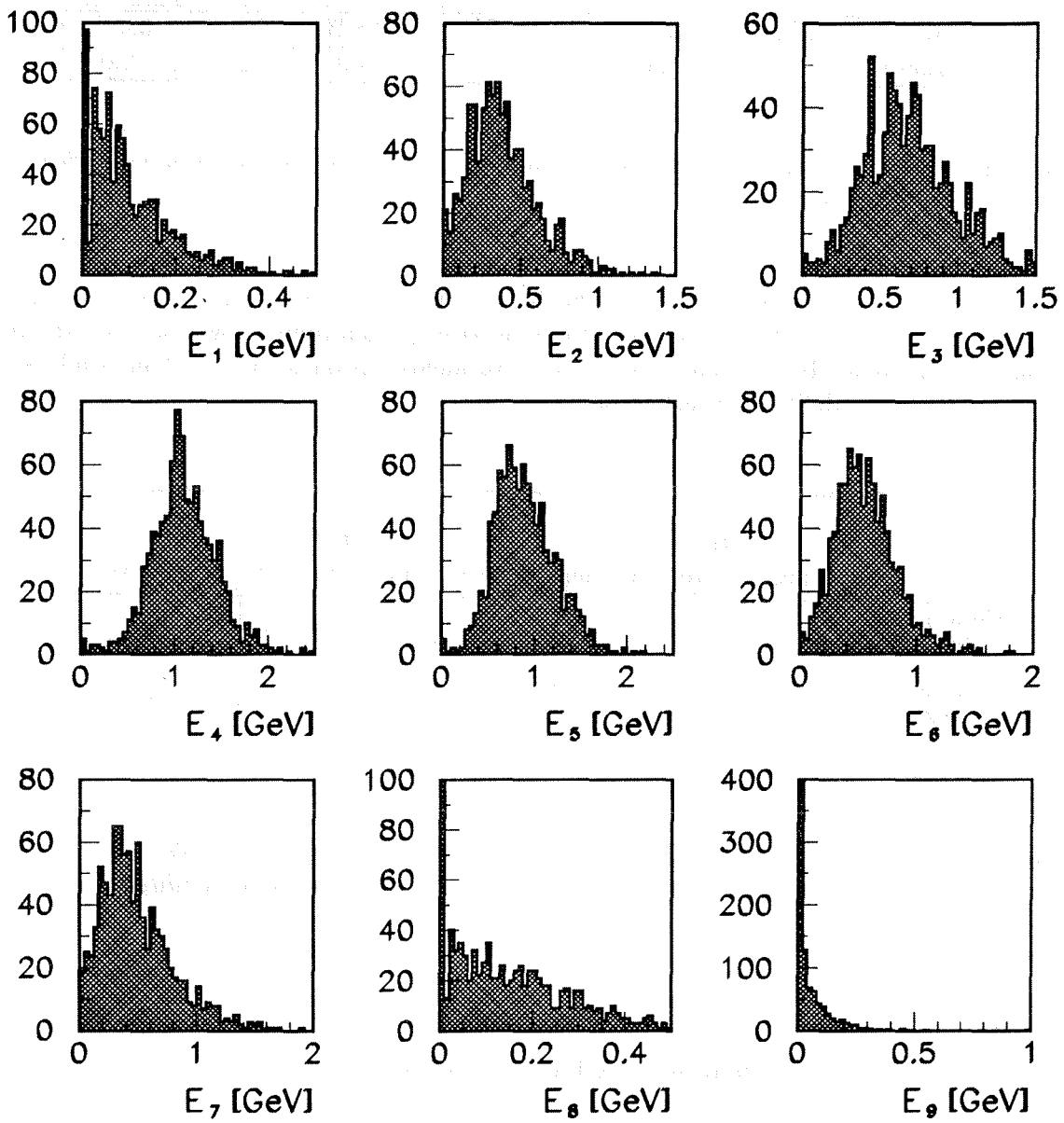

Figure 6.32: *Energy depositions in the nine layers of the HPC for* 5 *GeV electron Monte Carlo showers. The Monte Carlo is generated without material in front of the HPC and at an injection angle of* 90°. *The starting point of the generated electrons was shifted by* 40*cm in Z-direction.*

the approximation of Gaussian distributed quantities is rather good. Studies of the dependence on $\cos\theta$ where crack- and leakage-effects come into play, are even more complicated. In order to obtain the main fluctuations due to the sampling structure of the calorimeter, the following description will focus on regions where effects of cracks and leakage can be neglected.

From the energy E_{ik} of layer i ($i = 1,2,\cdots 9$)[16] and shower k we can compute the mean deposited energy per layer:

$$< E_i >= \frac{1}{N}\sum_{k=1}^{N} E_{ik} \tag{6.37}$$

where N is the number of showers. Using this definition we can calculate a matrix **M** which includes all information about correlations and shower fluctuations:

$$M_{ij} =< E_i \cdot E_j > \tag{6.38}$$

Subtracting the product of the mean values $< E_i >< E_j >$ leads to the covariance matrix σ:

$$\sigma_{ij}^2 = < E_i \cdot E_j > - < E_i >< E_j > \tag{6.39}$$

$$= < (E_i - < E_i >)(E_j - < E_j >) > \tag{6.40}$$

Thus, working with the covariance matrix implies a subtraction of the mean shower shape from the fluctuations which will be obtained later. Since we want to keep this information in our studies we work with the matrix **M**.

Now let us look at this system as a problem in a nine-dimensional space. The basis of this system is given by the nine orthonormal vectors $\vec{e}_i$, which are the 9 dimensional extensions of the cartesian coordinate system in 3-space. The total energy vector $\vec{E}_{tot}$ which denotes the energies per layer for one single shower can then formally be calculated by the sum of the products of E_i and the basis vectors $\vec{e}_i$. In this special coordinate system the coefficient vector $\vec{E} = (E_1, E_2, \cdots, E_9)$ is identical to the vector $\vec{E}_{tot}$.

$$\vec{E}_{tot} = \sum_{i=1}^{9} E_i \cdot \vec{e}_i \tag{6.41}$$

In order to diagonalize the matrix **M**, we now need to perform a transformation to a different coordinate system which can be obtained by evaluating the eigenvalues λ_i and eigenvectors $\vec{x}_{\lambda_i}$ of the matrix **M**. The following equations determining λ_i and $\vec{x}_{\lambda_i}$ can easily be solved by using some standard software routines:

$$det(\mathbf{M} - \lambda_i \mathbf{E}) = 0 \tag{6.42}$$

$$(\mathbf{M} - \lambda_i \mathbf{E})\vec{x}_{\lambda_i} = 0 \tag{6.43}$$

Figure 6.33 shows the nine eigenvalues λ_i for the 5 GeV electron Monte Carlo with an injection angle of $\theta = 90°$. The corresponding nine eigenvectors $\vec{x}_{\lambda_i}$ are shown in a graphical way in Figure 6.34, where each bin is the coefficient a_{ij} multiplying vector $\vec{e}_j$ in the original non-diagonal system.

$$\vec{x}_{\lambda_i} = \sum_{j=1}^{9} a_{ij} \cdot \vec{e}_j \tag{6.44}$$

The nine eigenvectors are orthogonal to each other and have unit length. They form a ortho-normal-system[17].

The eigenvalues in Figure 6.33 are portrayed by decreasing size. On the logarithmic scale

[16] In this description it is more reasonable to skip the trigger layer and work only with the nine energy layers.

[17] Due to a freedom in choosing the direction of the coordinate system, the sign of the eigenvectors is accidentally.

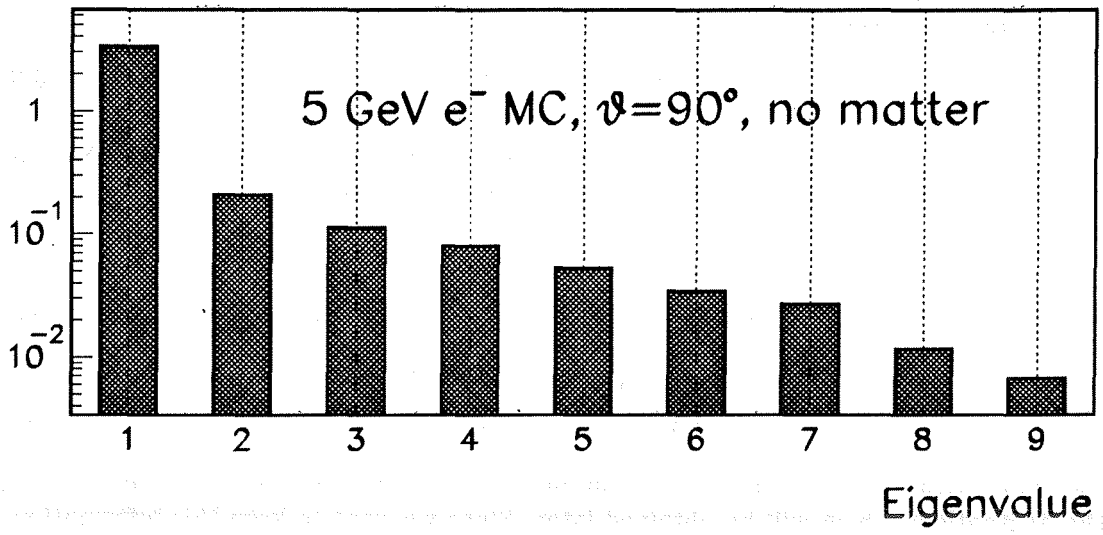

Figure 6.33: *Eigenvalues of the matrix* $M_{ij} =< E_i E_j >$ *for 5 GeV Monte Carlo showers.*

of the plot, it can be seen that the first eigenvalue λ_1 is dominating the situation completely. It is more than one order of magnitude larger than the other eigenvalues. Looking at the corresponding eigenvector $\vec{x}_{\lambda_1}$, it can be seen that it roughly describes the mean shape of a shower. Since it corresponds to the largest eigenvalue, it is clear that this structure will dominate in the shower development.

The eigenvector $\vec{x}_{\lambda_2}$ corresponding to the next eigenvalue λ_2 describes the first real shower fluctuation. The shape of it looks similar to a sine – function. In the first half of the layers the curve is higher than in the second half. This corresponds to a displacement of the whole shower along the shower axis.

The second shower fluctuation is described by the eigenvector $\vec{x}_{\lambda_3}$. The situation appears rather more complicated here. It implies the fact that the shower fluctuates in its width and becomes broader or smaller.

The influence of the following eigenvectors is smaller because of the drop of the corresponding eigenvalues. But the eigenvectors show some interesting structures. The eigenvectors $\vec{x}_{\lambda_8}$ and $\vec{x}_{\lambda_9}$ denote, for example, the fact of fluctuations in the first and ninth layer. This is understandable, if one thinks of the appearance of 'long life' photons and curling electrons, which can dominate these layers completely since the average energy deposition in these layers is small. Furthermore, the fact that the energies in these layers are not Gaussian distributed can contribute to the appearance of these structures.

We can now perform a transformation in the nine-dimensional space to the coordinate system of the nine eigenvectors. Since these eigenvectors are orthogonal to each other and have unit length, they form an adequate coordinate system for the 9-space. The basis $\vec{e}_i'$ of the new coordinate system can then be written as:

$$\vec{e}_i' = \vec{x}_{\lambda_i} \tag{6.45}$$

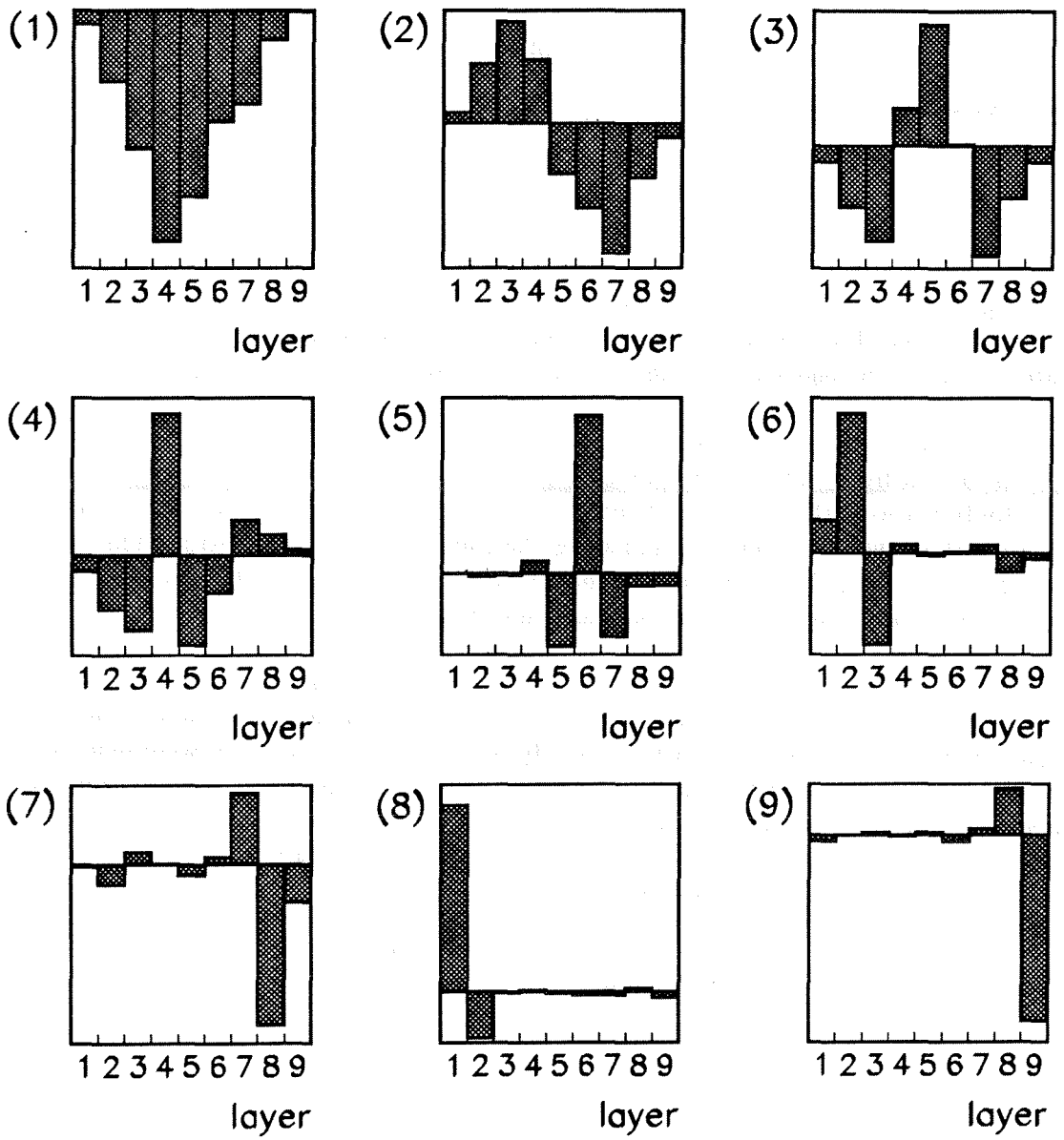

Figure 6.34: *Eigenvectors of the matrix* $M_{ij} =< E_i E_j >$ *for 5 GeV Monte Carlo showers. The material in front of the HPC was not simulated in this Monte Carlo.*

In this coordinate system the matrix **M** transforms to the diagonal matrix **M**$'$.

$$\mathbf{C} = |\vec{e}_1', \vec{e}_2', ...\vec{e}_9'| \tag{6.46}$$

$$\mathbf{M}' = \mathbf{C}^{-1}\mathbf{M}\mathbf{C} = \begin{pmatrix} \lambda_1^2 & 0 & \cdots & 0 \\ 0 & \lambda_2^2 & \cdots & 0 \\ \cdots & \cdots & \cdots & \cdots \\ 0 & 0 & \cdots & \lambda_9^2 \end{pmatrix} \tag{6.47}$$

The energy coefficient vector $\vec{E} = (E_1, E_2, \cdots, E_9)$ transforms in the following way

$$\vec{E}\,' = \mathbf{C}^{-1}\vec{E} \quad , \tag{6.48}$$

where the total energy per layer $\vec{E}_{tot}$ can now be calculated by

$$\vec{E}_{tot} = \sum_{i=1}^{9} E_i' \cdot \vec{e}_i\,' \quad . \tag{6.49}$$

Figure 6.35 shows the distributions of the energy coefficients E_i' for the 5 GeV Monte Carlo. In the first approximation these distributions are all Gaussian. They are all centered at zero, except for the E_1', which describes the mean shape of a shower. Since we transformed to the coordinate system of the eigenvectors, these coefficients are now uncorrelated.

The question now is: What differences do arise if we use a Monte Carlo, which also simulates the matter in front of the calorimeter? Figure 6.36 shows the different eigenvalues for a 5 GeV Monte Carlo with and without matter. It becomes clear, that the first eigenvalue for the case without matter is more dominating than for the case with matter. This means that the influence of the fluctuations is increased in the presence of matter in front of the calorimeter. The main eigenvectors are basically not changed.

It is interesting now to see how well the model of a Γ-distribution for the longitudinal shower shape describes the different fluctuations, which become visible with this method. Therefore, 5 GeV shower profiles using the Γ-distribution from the previous sections were generated. The material in front of the HPC was not simulated. As input parameters random numbers obeying a Gaussian distribution for E, V and W were used. The mean values M and standard deviations σ for these parameters were taken from the HPCSIM Monte Carlo and the energy parametrization explained in section 6.3.2.

$$M_E = 5.0\ GeV \qquad \sigma_E = 0.490\ GeV \tag{6.50}$$

$$M_V = 0.188 \qquad \sigma_V = 0.037 \tag{6.51}$$

$$M_W = 0.308 \qquad \sigma_W = 0.098 \tag{6.52}$$

$$\alpha = \left(\frac{W}{V}\right)^{1.5} + 1 \tag{6.53}$$

$$\beta = \sqrt{\frac{W}{V}} \tag{6.54}$$

$$\frac{dE}{dt} = E \cdot \beta \cdot \frac{(\beta t)^{\alpha-1} \cdot e^{-\beta t}}{\Gamma(\alpha)} \tag{6.55}$$

This method is widely used in fast simulation programs, because, in this way, the energy per layer can be calculated using an analytical formula, which is very fast compared to normal simulation methods.

From these calculations, layer energies have been obtained, which were analyzed in the same way as the data from HPCSIM. Figure 6.37 shows the eigenvalues from the fast simulation in comparison to the HPCSIM results for 5 GeV electrons. It is visible that the first three eigenvalues are in very good agreement to the results from HPCSIM. Then the differences become large.

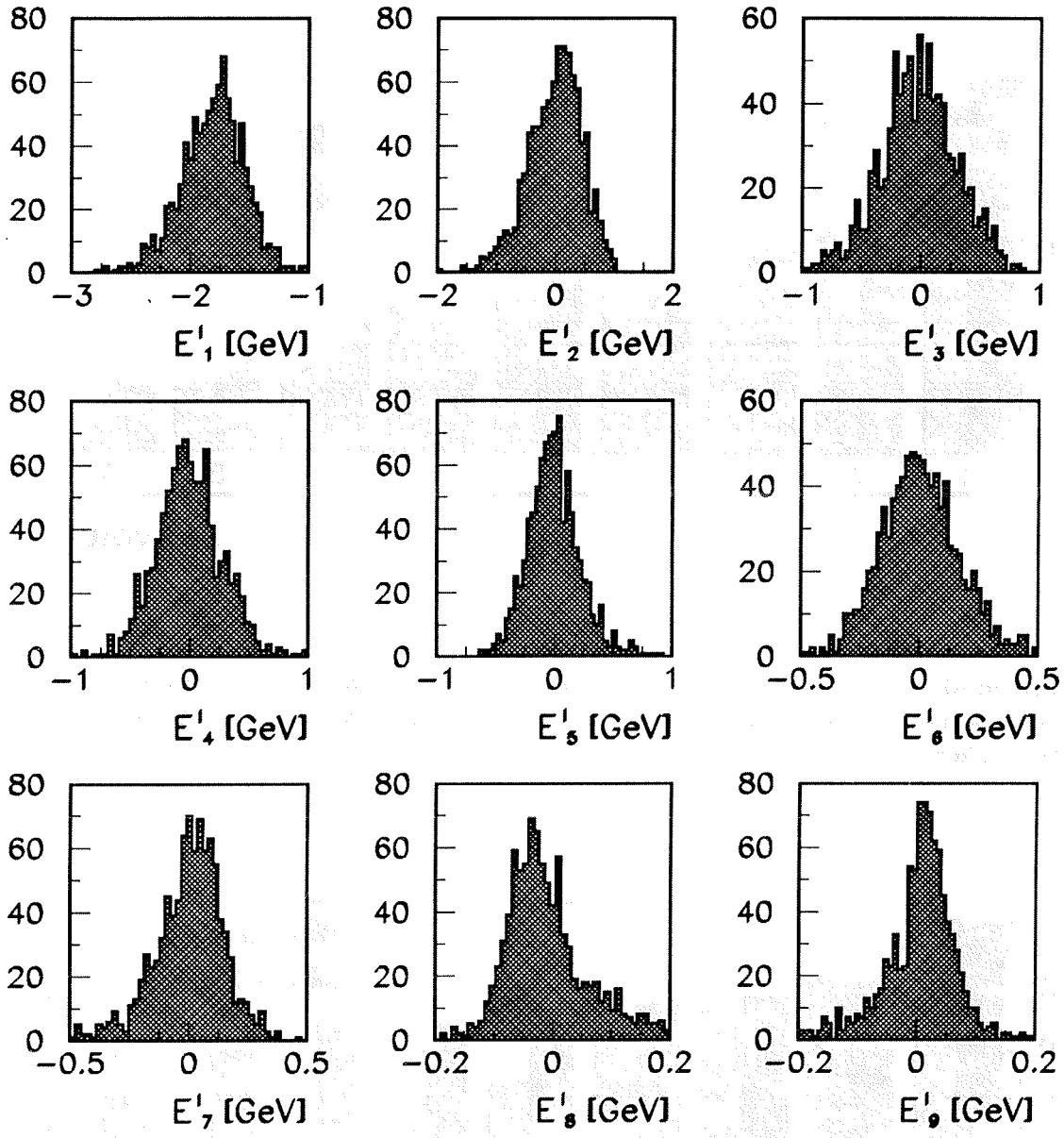

Figure 6.35: *Layer energies in the coordinate system of the eigenvectors for 5 GeV Monte Carlo showers. The injection angle was 90°. The material in front of the calorimeter was not simulated.*

The corresponding eigenvectors for the Γ-parametrized case are shown in Figure 6.38. It can be seen that the first three eigenvectors are very similar to the results from HPCSIM (see Figure 6.34). This means that the simple model using a Γ-distribution is able the reproduce the mean shower shape and the first and second shower fluctuations. The displacement of the shower along the shower axis is taken into account as well as the change of the longitudinal width of the shower. Very small fluctuations such as the fluctuations in the first and last layer

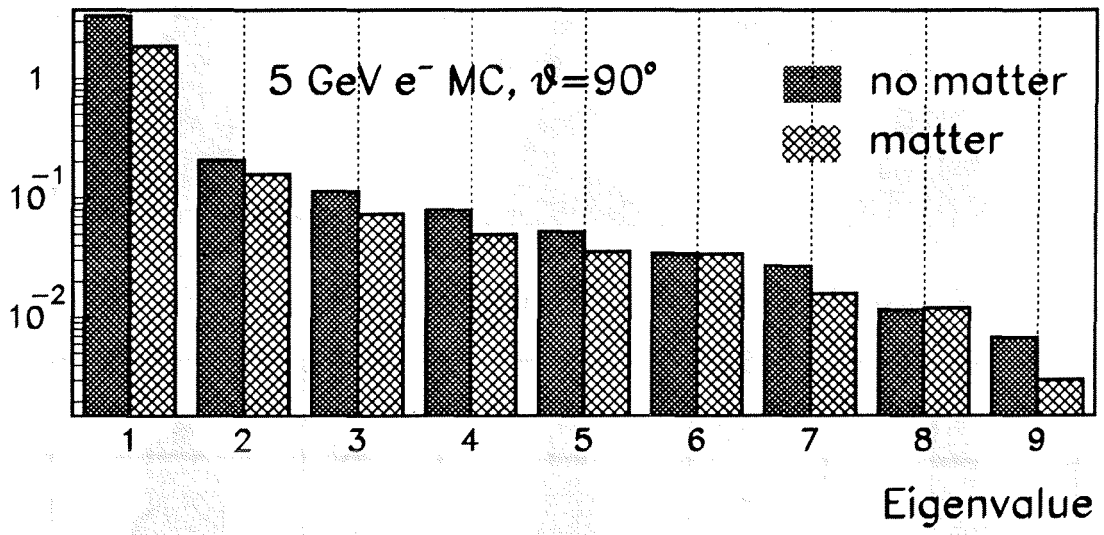

Figure 6.36: *Comparison of the eigenvalues for 5 GeV Monte Carlo electrons with and without matter. The first eigenvalue is more dominating in the case without matter because of the smaller fluctuations.*

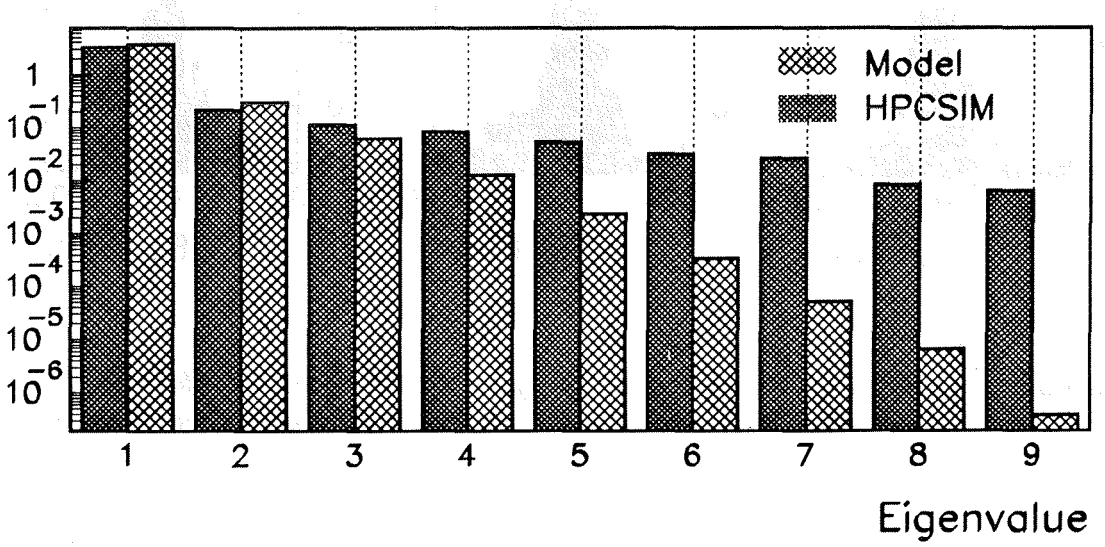

Figure 6.37: *Comparison of the eigenvalues of the Γ-distribution model and HPCSIM for 5 GeV electrons. The material in front of the HPC was not simulated.*

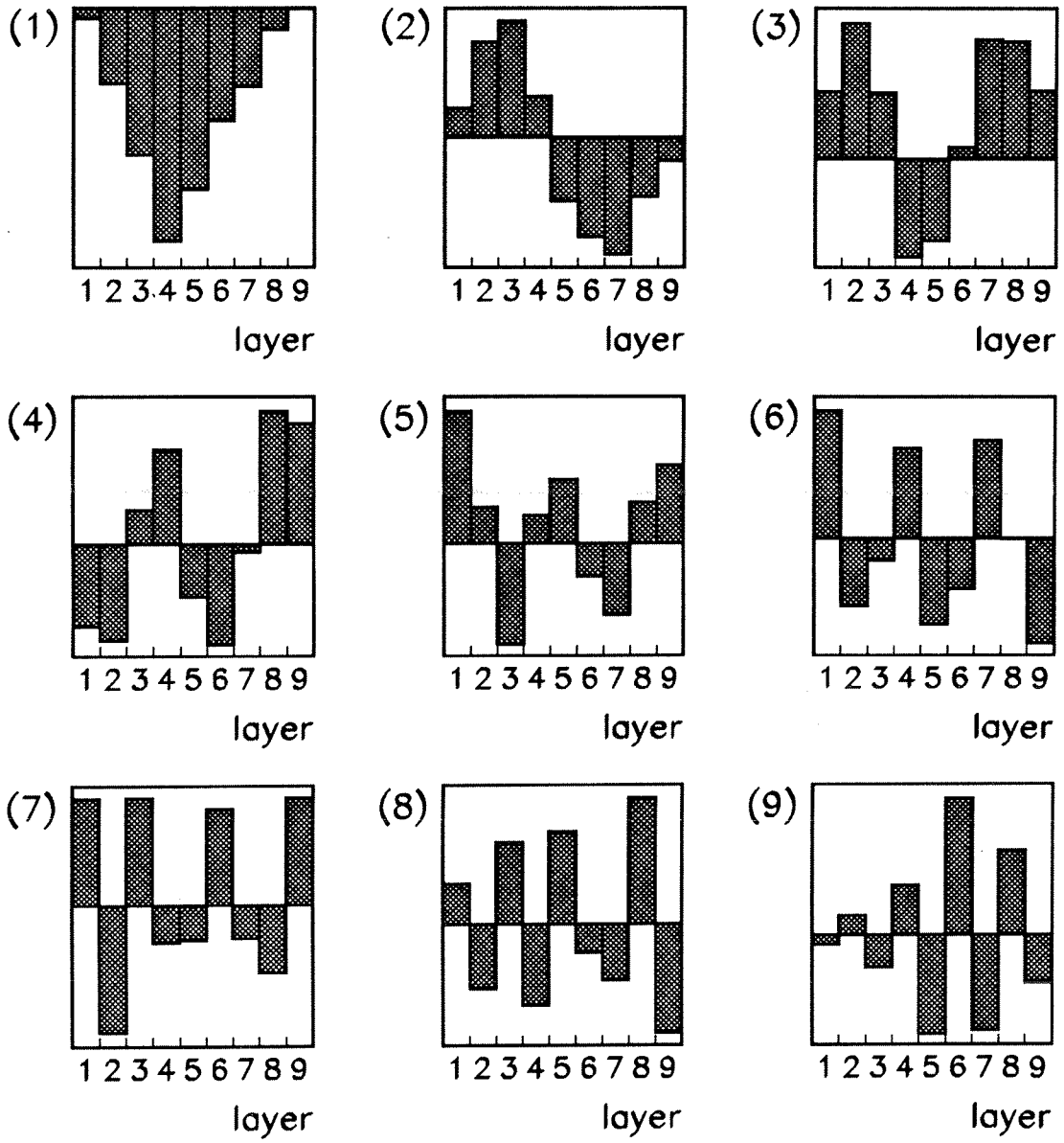

Figure 6.38: *Eigenvectors for the Γ-distribution model for 5 GeV electrons and no material in front of the HPC. The first three eigenvectors are very similar to the results from HPCSIM shown in Figure 6.34.*

are not reproduced. Since these fluctuations are only small corrections, the agreement in the first three eigenvectors is extremely astonishing.

Similar kinds of analyses have been performed for measured data. A good agreement between data and Monte Carlo has been observed. The goal here was, to show the agreement between the predictions from HPCSIM and the Γ-distribution model.

Chapter 7

Summary and Conclusions

In present and future experimental high energy physics, calorimeters are and will play a major role in complex detector systems. Therefore the construction and study of new technologies such as the High Density Projection Chamber (HPC) contribute to the development in detector physics. In this report several studies concerning the HPC are described.

In summary, one can say that the calibration of the HPC for 1992 data (DANA92_C) is well understood. Applying several corrections for hardware failures (e.g. short circuits, drift velocity instabilities, run instabilities, ...) the energy and spatial resolution of the HPC could be improved drastically. For the first time, the Z resolutions agreed with the values quoted in the original proposal [8]. The constant term could be reduced in comparison to previous processings. Further improvement with the increased Bhabha statistics of 1993 is not excluded.

Monte Carlo studies of brass and graphite chambers delivered a consistent picture about the Krypton calibration. The different resolutions for brass and graphite chambers could be understood as an effect of the transparency of the graphite grid. The dependence of the resolutions on the various parameters (transverse diffusion, drift field, chamber field, geometrical structure) has been studied and understood. The dramatic influence of the magnetic field has been discussed in a detailed way. Thus, one can say that a Krypton calibration of graphite chambers is possible in the same way as for brass chambers. Furthermore, Monte Carlo studies for minimum ionizing particles and electron showers lead to predictions for the different attenuation length in brass and graphite chambers. The predicted values are in good agreement with the measurements obtained in the West Area.

Chapter 6 described the main possibilities for electron identification in DELPHI. The tool of the longitudinal shower fit on the nine read-out layers of the HPC was explained in detail. By using the model of a Γ-distribution, parametrizing the longitudinal shape of an electromagnetic shower, a working algorithm was developed which provides a significant separation between electromagnetic and hadronic showers. After a simplified model of the material distribution in DELPHI was derived and an energy parametrization of the major parameters was developed, the χ^2 for the fit was defined in order to eliminate the main shower fluctuations. Detailed studies on the nature of shower fluctuations revealed the model using a Γ-distribution

to be able to reproduce the first and second real shower fluctuation. The goal was, in order to improve efficiencies, to extend the shower fit to work also in θ-cracks. The recovery of θ-crack showers was shown to be excellent.

The overall results from the electron identification are now comparable with the results from other detectors at LEP. It was shown that the shower fit and the dE/dx measurement provide the most powerful tools in the present electron identification routine. First results in J/ψ reconstruction using the decay $J/\psi \rightarrow e^+e^-$ are very encouraging. Further improvement is not excluded by performing a fit in the transverse shower directions although a strong correlation on the longitudinal shower fit is expected. Moreover, an improved spatial resolution in the processings DELANA_F and DANA92_D will necessarily lead to a better separation using the geometrical electron identification tools.

The longitudinal shower fit in the HPC can also be used for photon identification. First tests with D^* and η reconstruction have already been performed.

References

[1] S.L. Glashow, Nucl. Phys. 22, 579 (1967),
S. Weinberg, Phys. Rev. Lett. 19, 1264 (1967),
S. Salam in *Elementary Particle Theory*, 367 Stockholm (1968)

[2] G. Arnison *et al.* (UA1 collaboration), Phys. Lett. B 126, 398 (1983),
M. Banner *et al.* (UA2 collaboration), Phys. Lett. B 129, 130 (1983)

[3] V. Hatten *et al.* , LEP Performance Note 12 (1990),
R. Baily *et al.* , CERN-SL 90-95 (1990)

[4] L. Arnaudon *et al.* , CERN-PPE 92-125 (1992),
Notes of the 16th Meeting of the Working Group on LEP Energy
from 15 April 1992 at CERN, unpublished

[5] H. Sexel, R. Sexel, Weisse Zwerge – Schwarze Löcher, Vieweg Studium 2. Auflage (1979)

[6] H. Daniel, Beschleuniger, B. G. Teubner Stuttgart 1974

[7] DELPHI collaboration, P. Aarnio *et al.* , The DELPHI detector at LEP, Nuclear Instruments and Methods in Physics Research A303 (1991) 233-276, North Holland, Amsterdam

[8] DELPHI collaboration, DELPHI Technical Proposal, CERN/LEPC/83-3 LEPC/P 2,
17 May 1983

[9] A. Daum, Inbetriebnahme und Funktionsüberprüfung des schnellen neutralen Triggers am DELPHI-Detektor (LEP), Diplomarbeit an der Uni. Karlsruhe, IEKP-KA/91-3

[10] HPC Group, Pattern Recognition and Reconstruction of Photons and Charged Particles using the HPC Electromagnetic Calorimeter in the DELPHI Detector,
DELPHI 91-39 PROG 174 CAL 88, 9 March 1992

[11] J. Ellis, R. Peccei, Physics at LEP (Volume 1), Geneva 1986, CERN 86-02

[12] H. J. Hilke, Particle Detectors, CERN Academic Training Programme for Postgraduate Students, December 1992

[13] K. Kleinknecht, Detektoren für Teilchenstrahlung, B. G. Teubner Stuttgart 1987

[14] D. H. Perkins, Hochenergyphysik, Addison-Wesley Publishing Company (1991)

[15] W. R. Leo, Techniques for Nuclear and Particle Physics Experiments, Springer Verlag, Berlin 1987

[16] J. D. Jackson, Classical Electrodynamics 2nd Edition, John Wiley & Sons, New York 1975

[17] H. A. Bethe, J. Ashkin, Passage of Radiations through Matter, Experimental Nuclear Physics Vol. 1, John Wiley & Sons, New York 1953

[18] The American Physical Society, Physics Review D, Particles and Fields, Part II, Review of Particle Properties, Volume 45, Third series, Number 11, June 1992

[19] T. Mayer-Kuckuck, Kernphysik, B. G. Teubner Stuttgart 1984

[20] U. Amaldi, Fluctuations in Calorimetry Measurements, Phys. Scripta 23 (1981) 409-423

[21] B. Rossi, High-Energy Particles, Prentice Hall, New York 1952

[22] C. W. Fabjan, Calorimetry in High-Energy Physics, CERN-EP/85-54, Geneva 1985

[23] G. Grindhammer, M. Rudowicz, S. Peters, The Fast Simulation of Electromagnetic and Hadronic Showers, Nuclear Instruments and Methods in Physics Research A290 (1990) 469-488, North Holland, Amsterdam

[24] S. Peters, Parametrisierung hadronischer Schauer zur schnellen Kalorimeter-simulation im H1-Detektor, Diplomarbeit an der Universität Hamburg, MPI-PAE/Exp.El. 202, Juni 1989

[25] M. Rudowicz, Algorithmen zur Kalorimetersimulation mit parametrisierten Schauern am Beispiel des H1-Detektors, Diplomarbeit an der Universität Hamburg, MPI-PAE/Exp.El. 200, Januar 1989

[26] G. A. Akopdjanov *et al.* , Determination of Photon Coordinates in a Hodoscope Cherenkov Spectrometer, Nucl. Inst. and Meth. 140 (1977) 441-445

[27] F. Sauli, Principles of Operation of Multiwire Proportional and Drift Chambers Lectures given in the Academic Training Programme of CERN 1975-76 CERN 77-09, Geneva 1977

[28] S. F. Biagi, A Multiterm Boltzmann Analysis of Drift Velocity, Diffusion, Gain and Magnetic-Field Effects in Argone-Methane-Water-Vapour Mixtures, Nuclear Instruments and Methods in Physics Research A283 (1989) 716-722, North-Holland, Amsterdam

[29] A. Cattai, H. G. Fischer, A. Morelli, Drift Velocity in $AR + CH_4 +$ Water Vapours, DELPHI 89-63 TRACK 53 CAL 70, 28 July 1989

[30] M. Calvi, C. Matteuzzi, A Study of the HPC Detector using $45GeV$ Electrons, DELPHI 92-28 CAL 87, 9 March 1992

[31] Particle Data Group, Particle Properties Data Booklet, American Institute of Physics, June 1992

[32] Private communication with S. Schael

[33] J. A. Kadyk, Wire chamber ageing, Nuclear Instruments and Methods in Physics Research A300 (1991) 436-479, North Holland, Amsterdam

[34] S. Ragazzi, E. Rosenberg, Information available on Modules with Brass and Graphite Chambers, HPC internal memorandum, 29 May 1992

[35] A. Algeri, H. G. Fischer, M. Flammier, S-O. Holmgren, M. Szeptycka, Some results on HPC ageing with brass and graphite cathodes, DELPHI 92-103 CAL 100, 14 July 1992

[36] S. Squarcia, What we know about how to proceed for the HPC ageing repair? Memorandum to the DELPHI COP Members, 14 August 1992

[37] Private communication with S. Ragazzi

[38] Private communication with M. Feindt

[39] R. Jacobsson, H. Burmeister, Study of Muon Efficiency and Response in the HPC, DELPHI 93-16 CAL 101, 2 March, 1993

[40] Private communication with A. Cattai

[41] R. Veenhof, Garfield a drift-chamber simulation program, CERN Program Library W5050 (1989-91)

[42] Private communication with T. Tabarelli

[43] V. Gracco, L. Rossi, M. Sannino, L. Traspedini, Attenuation Length Measurements in Narrow Drift Channels, Nuclear Instruments and Methods in Physics Research A252 (1986) 573-578, North Holland, Amsterdam

[44] A. Firestone, Study of the HPC Energy Resolution, DELPHI 91-111 CAL 83, 16 December 1991

[45] Private communication with M. Wielers

[46] Private communication with D. Reid

[47] DELPHI collaboration, P. Abreu *et al.* , A Study of the decays of the tau lepton produced on the Z resonance at LEP, Z. Phys. C - Particles and Fields 55, 555-567 (1992)

[48] Private communication with G. Wormser

[49] M. Calvi, F. R. Cavallo, C. Matteuzzi, An Algorithm to Identify Electrons Using the HPC Electromagnetic Calorimeter of the DELPHI Detector, DELPHI 91-38 PROG 173, 17 July 1991

[50] P. Bambade, P. Zalewski, Study of Electron Identification in Hadronic Jets, DELPHI 92-32 PROG 183, 7 May 1992

[51] P. Ronchese, F. Simonetto, Electron Identification in DELPHI, DELPHI 93-6 PHYS 258, 18 January 1993

[52] K. Doroba, H. G. Fischer, J. Królikowski, M. Szeptycka, P. Szymański, The influence of material contained in the DELPHI detector on the performance of the barrel electromagnetic calorimeter HPC, DELPHI 92-61 PHYS 177 CAL 98, 29 May 1992

[53] Private communication with K. Mönig

[54] C. Stanescu, IGHPC An Interactive Graphics Program for HPC, DELPHI 89-10 PROG 129, 27 January 1989

Members of the DELPHI Collaboration

AUSTRIA - VIENNA

W.Adam, W.Bartl, R.Fruhwirth, J.Hrubec, G.Leder, D.Liko, F.Mandl, I.Mikulec, W.A.Mitaroff, M.Pernicka, M.Regler, J.Strauss

BELGIUM - ANTWERP, BRUSSEL, MONS

D.Bertrand, S.Braibant, C.Bricman, J.A.M.A.Buytaert, F.Cao, E.Daubie, H.De Boeck, C.De Clercq, F.Grard, P.Herquet, J.Kesteman, J.Lemonne, O.Pingot, F.Stichelbaut, S.Tavernier, C.Vander Velde, W.K.Van Doninck, F.Verbeure, J.H.Wickens

BRAZIL - LAFEX

I.Roditi

PUC

M.Begalli, R.C.Shellard

CIS - JINR - DUBNA

G.D.Alekseev, D.Y.Bardin, M.S.Bilenky, P.N.Bogolubov, G.A.Chelkov, V.M.Golovatyuk, B.A.Khomenko, N.N.Khovanski, A.V.Korytov, O.Kouznetsov, M.Lokajicek, G.V.Mitselmakher, A.G.Olshevski, J.Ridky, A.N.Sisakian, V.G.Timofeev, L.G.Tkatchev, E.N.Tsyganov, L.S.Vertogradov, A.S.Vodopyanov, N.I.Zimin

SERPUKHOV

Yu.Belokopytov, K.Belous, G.Borisov, M.Chapkin, P.Chliapnikov, R.Dzhelyadin, A.Fenyuk, S.Gumenyuk, A.Katargin, V.Kostioukhine, V.Lapin, V.Nikolaenko, V.Obraztsov, A.Ostankov, V.Perevozchikov, V.Ronjin, N.Smirnov, O.Tchikilev, A.Tomaradze, V.Uvarov, N.Vishnevsky, E.Vlasov, A.Zaitsev

DENMARK - NBI

E.Dahl-Jensen, G.Damgaard, J.E.Hooper, R.Moeller, B.S.Nielsen

FINLAND - HELSINKI

S.Czellar, I.Hietanen, R.Keranen, K.Kurvinen, R.Lauhakangas, J.Lindgren, R.Orava, K.Osterberg, J.Pennanen, C.Ronnqvist, H.Saarikko, O.Toker, T.Tuuva, L.Vitale, M.Voutilainen

FRANCE - CDF

P.Beilliere, J-M.Brunet, M.Crozon, C.Defoix, P.Delpierre, J.Dolbeau, Y.Dufour, P.Frenkiel, P.F.Honore, P.Lutz, J.Maillard, G.Tristram, R.Zukanovich Funchal

GRENOBLE

R.Barate, F.Ledroit, G.Sajot, T.S.Spassoff

LPNHE - PARIS

M.Baubillier, P.Billoir, H.Briand, J.Chauveau, V.Chorowicz, P.David, W.Da Silva, C.De La Vaissiere, B.Grossetete, F.Kapusta, F.Naraghi, R.Pain, I.A.Tyapkin

LYON

P.Antilogus, G.Smadja

MARSEILLE

A.Tilquin

ORSAY - LAL

J-E.Augustin, P.Bambade, M.Berggren, B.Bouquet, C.Bourdarios, L.Chaussard, G.Cosme, F.Couchot, S.Dagoret, B.Dalmagne, F.Fulda-Quenzer, G.Grosdidier, B.Jean-Marie, V.Lepeltier, A.Lopez-Fernandez, B.Muryn, F.Richard, P.Roudeau, A.Stocchi, P.Zalewski

SACLAY

T.Bolognese, P.Borgeaud, L.Chevalier, M.De Beer, G.Hamel De Monchenault, P.Jarry, J-P.Laugier, Y.Lemoigne, A.Ouraou, F.Pierre, V.Ruhlmann, Y.Sacquin, P.Siegrist, M-L.Turluer, D.Vilanova, M.Zito

STRASBOURG - CRN

D.Benedic, D.Bloch, F.Djama, J-P.Engel, J-P.Gerber, P.Juillot, J.M.Levy, R.Strub, T.Todorov, M.Winter

GERMANY - KARLSRUHE

W-D.Apel, A.Daum, W.De Boer, R.Ehret, D.C.Fries, H.Furstenau, U.Haedinger, M.Hahn, J.H.Koehne, M.Kopf, C.Kreuter, H.Mueller, P.Privitera, S.Schael, H.Schneider, R.Seufert

WUPPERTAL

K-H.Becks, J.Drees, F.Hahn, K.Hamacher, A.Koch-Mehrin, P.H.Kramer, U.Kruener-Marquis, G.Lenzen, E.Lieb, R.Lindner, T.Maron, M.A.E.Schyns, H.Staeck, S.Ueberschaer, M.Vollmer, H.Wahlen, A.Wehr, M.Weierstall, J.Werner, G.Zhang

UNITED KINGDOM - LANCASTER

P.N.Ratoff

LIVERPOOL

P.S.L.Booth, T.J.V.Bowcock, L.Carroll, K.A.J.Forbes, K.Furnival, T.L.Hessing, C.O.Higgins, M.Houlden, J.N.Jackson, D.Johnson, B.King, M.Mc Cubbin, R.Mc Nulty, B.Nijjhar, D.Reid, M.Richardson

OXFORD

M.J.Bates, C.J.Beeston, S.Blyth, S.Bosworth, P.Collins, P.D.Dauncey, F.J.Harris, S.D.Hodgson, J.Krstic, J.G.Loken, L.Lyons, G.Myatt, D.Radojicic, P.B.Renton, A.M.Segar, M.T.Trainor, G.R.Wilkinson, W.S.C.Williams, R.Zuberi

RUTHERFORD

T.Adye, R.J.Apsimon, D.Crennell, B.Franek, G.Gopal, J.Guy, G.Kalmus, W.J.Murray, R.Sekulin, G.R.Smith, M.Tyndel, W.Venus

GREECE - ATHENS

E.G.Anassontzis, P.Ioannou, G.Kalkanis, S.Katsanevas, C.Kourkoumelis, L.K.Resvanis, G.Voulgaris

ATHENS-NTU

M.Dris, D.Fassouliotis, T.A.Filippas, E.Fokitis, E.N.Gazis, E.C.Katsoufis, Th.D.Papadopoulou

DEMOKRITOS

P.Beltran, E.Karvelas, P.Kokkinias, C.Lambropoulos, D.Loukas, A.Maltezos, A.Markou, G.Stavropoulos, G.E.Theodosiou, E.Zevgolatakos

ITALY - BOLOGNA

F.R.Cavallo, F.L.Navarria, A.Perrotta, U.Rossi, T.Rovelli, G.Valenti, S.Volponi

GENOVA

M.Bozzo, C.Caso, R.Contri, G.Crosetti, G.Darbo, F.Fontanelli, V.Gracco, G.Meola, M.R.Monge, P.Morettini, A.Petrolini, I.Roncagliolo, M.Sannino, G.Sette, S.Simonetti, S.Squarcia, U.Trevisan

MILANO

A.Andreazza, M.Battaglia, M.Bonesini, W.Bonivento, M.Calvi, A.De Min, C.Matteuzzi, C.Meroni, P.Negri, M.Paganoni, A.Pullia, S.Ragazzi, N.G.Redaelli, T.Tabarelli, C.Troncon, G.Vegni

PADOVA

K.D.Brand, P.Checchia, A.Elliot Peisert, G.Galeazzi, U.Gasparini, I.Lippi, M.Margoni, M.Mazzucato, M.Michelotto, M.Pegoraro, T.E.Pettersen, P.Ronchese, F.Simonetto, L.Ventura, G.Zumerle

ROMA2

V.Bocci, V.Canale, L.Cerrito, L.Di Ciaccio, G.Matthiae

SANITA

A.Baroncelli, C.Bosio, P.Branchini, E.Graziani, A.Passeri, E.Spiriti, C.Stanescu, L.Tortora, V.Vrba

TORINO

F.Bianchi, R.Cirio, M.P.Clara, B.A.Della Riccia, N.Demaria, D.Gamba, G.Rinaudo, A.Romero, G.Sciolla, E.Torassa, E.Vallazza

TRIESTE/UDINE

G.Barbiellini, E.Castelli, A.De Angelis, B.De Lotto, L.Lanceri, P.Poropat, F.Scuri, M.Sessa, F.Waldner

NETHERLANDS - NIKHEF

E.Agasi, A.Augustinus, N.Brummer, N.De Groot, S.Haider, W.Hao, D.Holthuizen, P.Kluit, B.Koene, M.Los, H.Palka, W.Ruckstuhl, I.Siccama, J.Timmermans, D.Z.Toet, G.W.Van Apeldoorn, P.Van Dam

NORWAY - BERGEN

S.J.Alvsvaag, T.A.Fearnley, A.G.Frodesen, P-S.Iversen, A.Klovning, E.Lillethun, P.E.S.Nilsen

OSLO

L.Bugge, T.Buran, M.Dam, A.L.Read, T.B.Skaali, G.Skjevling, S.Stapnes, J.Wikne, D.Wormald

POLAND - KRAKOW

Z.Hajduk, P.Jalocha, K.Korcyl, W.Krupinski, G.Polok, K.Rybicki, M.Turala, A.Zalewska

WARSZAWA

K.Doroba, R.Gokieli, M.Gorski, T.Hofmokl, J.Krolikowski, A.Lipniacka, R.Sosnowski, M.Szczekowski, M.Szeptycka, P.Szymanski

PORTUGAL - LIP

P.Abreu, F.Barao, M.Pimenta, J.Varela

SPAIN - MADRID

J.A.Barrio, J.L.Contreras, J.Sanchez

SANTANDER

A.J.Camacho Rozas, J.Cuevas Maestro, M.Fernandez Alonso, J.Garcia, M.A.Lopez Aguera, J.Marco, F.Matorras, A.Ruiz

VALENCIA

P.Allen, M.V.Castillo Gimenez, J.T.Chrin, E.Cortina, M.D.M.De Fez Laso, A.Ferrer, C.Garcia, J.J.Hernandez, E.Higon, C.Lacasta, J.J.Lozano, S.Marti, J.Salt, J.A.Valls Ferrer, J.Zuniga

SWEDEN - LUND

S.Almehed, O.Barring, J.Bjarne, A.Hakansson, G.Jarlskog, L.Jonsson, I.Kronkvist, B.Loerstad, U.Mjoernmark

STOCKHOLM

B.Åsman, G.Ekspong, A.Goobar, S-O.Holmgren, P.O.Hulth, K.Hultqvist, E.K.Johansson, T.Moa, P.Niss, C.Walck, N.Yamdagni

UPPSALA

O.Botner, L-O.Eek, T.Ekelof, A.Hallgren, K.Kulka, K.Woschnagg

SWITZERLAND - CERN

U.Amaldi, P.Baillon, H.Borner, B.Bostjancic, R.A.Brenner, R.C.A.Brown, H.Burmeister, M.Caccia, T.Camporesi, F.Carena, A.Cattai, V.Chabaud, Ph.Charpentier, M.Davenport, D.Delikaris, S.Delorme, H.Dijkstra, M.Donszelmann, M.Dracos, P.A.-M.Eerola, M.Feindt, H.Foeth, J.Fuster, C.Gaspar, Ph.Gavillet, P.Giacomelli, J.J.Gomez Y Cadenas, A.Grant, E.Gross, P.Grosse-Wiesmann, T.Henkes, H.Herr, H.J.Hilke, D.Isenhower, M.Jonker, M.Karlsson, N.J.Kjaer, H.Klein, W.Klempt, R.Leitner, J-C.Marin, G.Maehlum, K.Moenig, L.Pape, M.E.Pol, S.Rossi, E.Rosso, J.Straver, D.Treille, W.Trischuk, A.Tsirou, S.Tzamarias, O.Ullaland, P.Vaz, P.Weilhammer, A.M.Wetherell, P.Yepes, D.Zavrtanik

USA - AMES

A.Chan, H.B.Crawley, D.Edsall, A.Firestone, J.W.Lamsa, L.Mathis, R.Mc Kay, W.T.Meyer, E.I.Rosenberg, M.Wayne

Acknowledgements

I would like to thank Prof. Dr. W. de Boer for his continuous support and providing me with the possibilty to work in the HPC group at CERN. I am grateful to Prof. Dr. D. C. Fries for having accepted to be my *Koreferent.*

The realization of this thesis was supported by several people of the HPC group: Dr. A. Cattai, D. Edsall, Dr. M. Feindt, Dr. H. Fürstenau, Dr. O. Podobrin and Dr. S. Schael.

In particular, I would like to thank Dr. M. Feindt for the interesting topics of analysis, many instructive discussions and ideas and a good working atmosphere. Furthermore, I am grateful to Dr. S. Schael for his support during the development of the longitudinal shower fit.

I am grateful to Dr. A. Cattai for providing me with the possibility to present parts of my results at the DELPHI week in Rome (1992) and at the spring conference 1993 of the German Physics Society (DPG) in Mainz.

Furthermore, I would like to thank D. Edsall for his comments on this thesis.

I would especially like to thank my whole family and my friends. Their support was essential for my studies and for the work on this thesis.